

OPTICAL PROPERTIES OF SMALL METAL CLUSTERS

THÈSE N° 6718 (2015)

PRÉSENTÉE LE 9 OCTOBRE 2015
À LA FACULTÉ DES SCIENCES DE BASE
LABORATOIRE DE NANOSTRUCTURES SUPERFICIELLES
PROGRAMME DOCTORAL EN PHYSIQUE

ÉCOLE POLYTECHNIQUE FÉDÉRALE DE LAUSANNE

POUR L'OBTENTION DU GRADE DE DOCTEUR ÈS SCIENCES

PAR

Chongqi YU

acceptée sur proposition du jury:

Prof. R. Houdré, président du jury
Dr W. Harbich, Prof. H. Brune, directeurs de thèse
Prof. V. Kresin, rapporteur
Dr M. Hillenkamp, rapporteur
Prof. O. Martin, rapporteur



ÉCOLE POLYTECHNIQUE
FÉDÉRALE DE LAUSANNE

Suisse
2015

Abstract

This thesis is devoted to the study of the optical properties of small metal clusters and metal cluster organic compounds. For this purpose a ultra-high vacuum (UHV) experimental apparatus has been built which allows for the deposition of mass selected neutral clusters in a size range up to 16,000 amu which corresponds to Ag_{150} or Au_{80} . Cluster cations are produced in a gas aggregation cluster source, steered in an ion optics device and co-deposited with electrons and excess rare gas on a cryogenic deposition head. Neutral mono dispersed clusters are analyzed by optical absorption, fluorescence and excitation spectroscopy in the UV-visible energy range. A novel custom-made conical octupole combined to an organic molecule injector has been built, serving as a generator of metal cluster-organic compounds. These are atomically precise model systems which permit to study surface-enhanced Raman scattering (SERS) in order to test the theoretical models and better understand the mechanism of SERS.

Optical absorption on size-selected silver clusters of Ag_n ($n = 20 - 120$) embedded in neon solid matrix was investigated. The spectra show plasmon-like absorption profiles around a photon energy of 4.0 eV which match in energy molecular like absorption spectra for the smallest Ag clusters but are sensitively higher than what would be expected for the dipolar absorption for bulk silver of about 3.3 eV. The central absorption peak, i.e. the plasmon energy as a function of cluster size is presented. The data fall in a transition between a blueshift of the plasmon resonance with decreasing size to a superimposed red shift for the very smallest sizes. Superimposed, we observe a distinct structure where clusters with atom number of 8, 18, 34, 58, 92 show a localized maximum value of the plasmon energy. These numbers correspond perfectly to the fully filled states of 1p, 1d, 1f, 1g and 1h according to the electronic shell model, manifesting a clear sub-shell effect.

Optical absorption, fluorescence and excitation spectroscopy on size-selected small gold clusters of Au_m ($m = 19, 20, 21$) embedded in solid neon were measured. These are the first optical data on ligand free neutral atomically precise Au clusters. Au_{20} , the famous tetraedic structure, shows a rich structured absorption spectrum, superimposed on a continuous background increasing to the UV part of the spectrum. Au_{21} and Au_{19} show the same tendency, however without any superimposed structure. Very interestingly, all three Au clusters show strong fluorescence centered at around 1.85 eV, here again Au_{20} being the prominent species. Comparison to ligand protected Au clusters clearly proves that the fluorescence comes from the Au cluster itself and is only weakly influenced by the ligands.

For the first time, size-selected small metal-organic compounds of silver-pyridine Ag_aPy_b

Abstract

($a=1,3$; $b=1,2$) which are prototypes for surface enhanced Raman scattering (SERS) have been produced and isolated in a solid Ne matrix. Optical absorption and fluorescence spectra have been measured. Raman scattering cross sections with an enhancement factor of 10^3 have been found in fair agreement with recent high level time-dependent density functional theory (TDDFT) calculations.

Keywords: Clusters, Solid rare-gas matrix, Silver, Gold, Pyridine, Optical absorption, Fluorescence, SERS, Vacuum, Cryogen.

Résumé

Cette thèse est consacrée à l'étude des propriétés optiques de petits agrégats métalliques ainsi que de composés contenant des molécules organiques et des agrégats métalliques. Dans ce but, un dispositif expérimental à ultra-vide a été fabriqué, permettant la déposition d'agrégats métalliques neutres sélectionnés en masse, d'une taille pouvant atteindre 16'000 uma, ce qui correspond à du Ag_{150} ou Au_{80} . Des agrégats chargés positivement sont produits dans une source de condensation, guidés à l'aide d'un dispositif électrostatique et déposés dans une matrice de gaz rare. Les agrégats neutres sont analysés par spectroscopie d'absorption optique, de fluorescence et d'excitation dans le domaine UV-visible. Un octopôle conique combiné à un injecteur de molécules organiques a été développé, servant ainsi de générateur pour les composés organo-métalliques. Ces derniers sont des systèmes modèles pour l'étude de la diffusion Raman amplifiée par effet de surface (SERS) permettant de tester les modèles théoriques et de mieux comprendre le mécanisme SERS.

L'absorption optique d'agrégats d'argent Ag_n ($n = 20 - 120$), sélectionnés en masse et isolés dans une matrice de néon solide, a été étudiée. Le spectre montre un profil d'absorption de type plasmonique autour d'une énergie de photons de 4.0 eV, ce qui concorde avec le spectre d'absorption de type moléculaire pour les plus petits agrégats d'Ag tout en étant sensiblement plus élevé que ce que l'on attendrait pour une absorption dipolaire dans l'argent solide, qui est d'environ 3.3 eV. La position du pic d'absorption, c.-à-d. l'énergie de plasmon est présentée en fonction de la taille des agrégats. Les données correspondent à une transition entre un décalage vers le bleu de la résonance plasmonique suivant une taille décroissante à une superposition de décalage vers le rouge. De plus, nous observons une structure distincte superposée, où les agrégats contenant 8, 18, 34, 58 ou 92 atomes montrent un maximum de la valeur d'énergie du plasmon. Ces nombres correspondent parfaitement à un remplissage complet des états 1p, 1d, 1f, 1g et 1h définis dans le modèle en couches électroniques, révélant clairement un effet de sous-couches.

Les spectroscopies d'absorption optique, de fluorescence et d'excitation sur des agrégats d'or Au_m ($m = 19, 20, 21$) sélectionnés en masse et isolés dans une matrice de néon solide ont été mesurées. Ce sont les premières données optiques d'agrégats d'Au neutres de nombre d'atomes bien défini et sans ligands. L'agrégat Au_{20} , célèbre pour sa structure tétraédrique, montre un spectre d'absorption riche en structures, superposé à un fond continu croissant dans la partie UV du spectre. Les agrégats de Au_{21} et Au_{19} montrent la même tendance, toute-

Résumé

fois sans aucune structure superposée. Il est intéressant de noter que les trois types d'agrégats d'or montrent une forte fluorescence centrée autour de 1.85 eV, où celle d'Au₂₀ est la plus marquée. La comparaison avec des agrégats d'Au en l'absence de tout ligands démontre clairement que cette fluorescence provient de l'agrégat d'or lui-même et qu'elle n'est que faiblement influencée par les ligands.

Pour la première fois, de petits agrégats de composés organo-métalliques d'argent-pyridine Ag_aPy_b (a= 1, 3 ; b= 1, 2), des prototypes pour l'étude de la diffusion Raman amplifiée par effet de surface, ont été produits et isolés dans une matrice de néon. Leurs spectres d'absorption optique et de fluorescence ont été mesurés. Des sections efficaces de diffusion Raman avec un facteur d'amplification de 10³ ont été observées, ce qui est en bonne adéquation avec de récents calculs time-dependent density functional theory (TDDFT).

Mots-clés : Agrégats, matrice de gaz rare, argent, or, pyridine, absorption optique, fluorescence, SERS, vide, cryogénie.

Contents

Abstract (English/Français)	iii
1 Introduction	1
2 Theory	7
2.1 Size dependent optical material function of clusters	7
2.2 Extrinsic cluster size effects	8
2.2.1 Bulk metals (Drude model)	8
2.2.2 Quasistatic response of a small metal sphere	11
2.2.3 Electrodynamic calculation of a small metal sphere (Mie theory)	13
2.2.4 Extrinsic size effect	17
2.3 Intrinsic cluster size effects	19
2.3.1 Size dependent optical material functions	20
2.3.2 Direct quantum mechanical calculations (Jellium approximation)	22
2.3.3 Shell model for simple metal clusters	23
2.3.4 Hydrodynamic model of a metal sphere	33
2.3.5 Time dependent density functional theory (TDDFT)	35
2.3.6 Intrinsic size effect	40
2.4 Surface enhanced Raman scattering (SERS)	42
2.4.1 The electromagnetic mechanism (EM)	42
2.4.2 The chemical mechanism (EM)	44
2.4.3 Unifying EM and CM	44
3 Experiment	47
3.1 Overview of apparatus	47
3.2 Vacuum system	47
3.3 Gas aggregation cluster source	49
3.3.1 Source setup	49
3.3.2 Sputtering process	50
3.3.3 Aggregation process	50
3.3.4 Characteristic of source	50
3.4 Ion guide device	51
3.4.1 Conical octupole	51
3.4.2 Quadrupole	52

Contents

3.4.3	Electrostatic lens	53
3.4.4	Ion deflector	53
3.5	Pyridine injector	54
3.6	Deposition head	55
3.6.1	Sample holder	55
3.6.2	Cryostat	55
3.6.3	Rare gas inlet	56
3.6.4	Filament	56
3.7	Optical setup	58
3.7.1	Light source and spectrometer	58
3.7.2	Fixed optical fiber	58
3.7.3	Optical absorption	58
3.7.4	Fluorescence collection	59
3.7.5	Excitation measurement	60
3.7.6	Raman measurement	60
3.8	Simulations of ion particles passing through the device	60
3.8.1	Transmission of cluster ions	60
3.8.2	Ions focusing and pre-mass selection	61
3.8.3	Mass selection and resolution	62
3.9	Mass spectra	63
3.9.1	Mass selection and ion detection	63
3.9.2	Resolution and purity of mass selection	63
3.9.3	Response to gas parameters	65
3.9.4	Size selection shift	65
3.9.5	Resolution effect	66
3.9.6	Isotope spectrum	67
3.9.7	Silver clusters spectra	68
3.9.8	Gold clusters spectra	69
3.9.9	Silver-pyridine clusters spectra	70
3.10	Optical spectra (Ag_3)	73
4	Result: Optical properties of silver clusters	75
4.1	Optical absorption spectra of Ag_n clusters ($n = 20, 35, 55, 58, 84, 92, 120$)	76
4.1.1	Ag_{20}	76
4.1.2	Ag_{35}	76
4.1.3	Ag_{55}	76
4.1.4	Ag_{58}	77
4.1.5	Ag_{84}	77
4.1.6	Ag_{92}	77
4.1.7	Ag_{120}	77
4.2	Comparison to TDDFT calculations	81
4.3	Plasmon energy of Ag_n clusters	85

4.3.1	Plasmon energy and width with cluster size	85
4.3.2	Bridge the gap between atom and bulk	86
4.3.3	Sub-shell effect	88
4.4	Polarizability of Ag clusters	90
4.4.1	Polarizability with cluster size	91
4.4.2	Comparison with theoretical model	91
5	Result: Optical properties of gold clusters	95
5.1	Optical response of Au ₂₀	96
5.1.1	Absorption spectrum of Au ₂₀	96
5.1.2	Fluorescence spectrum of Au ₂₀	97
5.1.3	Excitation spectrum of Au ₂₀	99
5.1.4	Conclusion of optical response of Au ₂₀	99
5.2	Optical response of Au ₁₉	103
5.2.1	Absorption spectrum of Au ₁₉	103
5.2.2	Fluorescence spectrum of Au ₁₉	103
5.3	Optical response of Au ₂₁	105
5.3.1	Absorption spectrum of Au ₂₁	105
5.3.2	Fluorescence spectrum of Au ₂₁	105
5.4	Comparison to TDDFT calculations	107
5.5	Transition of optical response of gold from atom to bulk	109
6	Result: Optical properties of silver-pyridine clusters	111
6.1	Optical response of Ag ₁ Py ₁	112
6.1.1	Absorption of Ag ₁ Py ₁	112
6.1.2	Fluorescence of Ag ₁ Py ₁	114
6.2	Optical response of Ag ₁ Py ₂	115
6.2.1	Absorption of Ag ₁ Py ₂	115
6.2.2	Fluorescence of Ag ₁ Py ₂	115
6.2.3	SERS of Ag ₁ Py ₂	116
6.3	Optical response of Ag ₃ Py ₁	118
6.3.1	Absorption of Ag ₃ Py ₁	118
6.3.2	Fluorescence of Ag ₃ Py ₁	119
6.4	Optical response of Ag ₃ Py ₂	120
6.4.1	Absorption of Ag ₃ Py ₂	120
6.4.2	Fluorescence of Ag ₃ Py ₂	120
6.4.3	SERS of Ag ₃ Py ₂	121
6.5	Conclusion of optical response of Ag _a Py _b ($a = 1, 3; b = 0, 1, 2$)	122
7	Conclusions	127
A	Supporting information to devices	129
B	Supporting information to simulations	131

Contents

Bibliography	135
Acknowledgements	147
Curriculum Vitae	149

1 Introduction

“If I have seen further, it is only by standing on the shoulders of giants.” – **Sir Isaac Newton** [1]

This is how human beings push science forward.

Physics, named from Ancient Greek: *φυσικ* (nature), and called as ‘natural philosophy’ until the late 19th century, is a branch of science and is currently defined as the study of matter, energy, and the relation between them.

The history of physics goes back to Ancient Greece times, at which time a Greek philosopher **Aristotle** (4th century BCE) proclaimed that all matter was made up of four elements: earth, water, air, and fire. During late 17th and early 18th centuries after two thousand years with several stages of scientific revolutions by many epochal physicists such as **Archimedes** and **Galilei** [2], an English physicist and mathematician **Sir Isaac Newton** established three laws of motion [3] and a law of universal gravitation [4], which laid the foundation of classical physics. At the beginning of the 20th century after more than two hundred years with the development of thermodynamics by **Thomson** and the promotion of electromagnetic theory by **Maxwell**, a major revolution shook the world of physics. The establishment of theory of relativity by a young German physicist **Albert Einstein** [5] and the foundation of quantum mechanics by a group of genius physicists leading by **Max Planck** [6] have knocked on the door of modern physics, which led to a new era.

Today, classical physics is still being used to describe the behavior of large-scaled bulk matter like the well-known tourism scenic flight by a hydrogen balloon who is light enough to overcome the gravity, and quantum physics is used to explain the phenomena in atomic-scaled particles such as the famous experiment of spectral series of hydrogen atom which led to the development of quantum electrodynamics. But there is still something in between that we don’t know clearly even today. A natural question then come out: What is between bulk and atom?

The answer is: cluster! In fact, cluster is not new. The glaziers in Middle Ages have already known how to produce beautiful and colorful stained glasses for church windows by special

treatments of metal-containing glasses. The first investigation of clusters was perhaps performed in 19th century by **Rayleigh** [7] who revealed the secret of color-changeable stained glasses behind due to the scattering of light by small metal particles embedded. This work was followed by **Mie** using electrodynamic at the beginning of 20th century, who then proposed a smart way of the study of cluster in 1908: “Gold atoms sure optically behave differently than small gold beads, so it would be very interesting to study their optical absorptions and track the process on how to build the gold particles from the atoms” [8]. But it was until more than half a century later that his idea about the study of optical properties of gold particles with sizes beyond the resolution limit of light microscopes has been realized thanks to the new field of cluster science.

What is cluster? Cluster is usually defined as a number of unspecified objects gathered together, composed of a certain number n of atoms with $2 \leq n \leq 10^7$. Cluster bridges the gap between bulk and atom. The study of cluster helps people to explore how a bulk is made up from one atom and how the micro property of atom transits to the macro property of bulk, thus to understand the transition from classical physics to quantum physics.

The development of cluster science begins at 1960s, during which time most of cluster work focused on the investigation of small metal particles in glasses for their electromagnetic properties [9]. At that time, new cluster sources were also improved to produce clusters of only a few atoms in gas phase which had shown properties that were different from those of bulk. Up to the early 1980s clusters were still thought as either small molecules treated with molecular physics and quantum-chemical methods, or bulk materials described by solid-state and statistical physics. The view of clusters changed in later 1983, when **Walter Knight**'s group produced and measured alkali metal clusters up to about 100 atoms, and found the electronic shell structure from the cluster abundance spectra where the clusters with valence electrons that matched the spherical shell-closing numbers were produced more abundantly [10]. Coincidentally at the same time, **Ekardt** independently predicted a shell model for metal clusters [11] using jellium approach adopted from nuclear shell theories, in which the cluster was considered to be a uniformly positive charged ionic sphere core filled with delocalized valence electrons in the mean field background created by the ionic core, resembling a giant atom. After the discovery of electronic shell structure, the simple metal clusters were treated as the quantized motion of collective delocalized electrons, and the detailed core structure did not affect so much the properties of clusters. The shell (jellium) model worked well even for clusters with several thousand atoms [12]. But the disadvantage of this model is also obvious: it neglects the ionic structure and works only for spherical metal clusters with electronically closed shell that satisfies the s-wave character of valence electrons, and for open-shell clusters the spherical shape is unstable towards distortion due to **Jahn-Teller** effect [13]. Hence, the shell model has its main applicability only in alkali metals such as sodium and potassium, and to some extent coinage metals like copper and silver. This problem had been noticed by **Clemenger** [14] who then adapted the deformed nuclear shell model of **Nilsson** [15] to metal clusters and explained the fine structure of cluster abundance spectra, giving birth to ellipsoidal shell model. From then on, the development of cluster science was rapid.

Cluster starts with the smallest size containing 2 atoms and ends with the largest size containing 10^7 atoms. The matter is like a long snake, with the head called bulk, the body called cluster, and the tail called atom. Generally, the physical property of a cluster is more sensitive to its size toward the tail than toward the head. For these very small clusters the surface is important, with the proportion of surface atoms of more than a quarter even for a cluster with 500 atoms. Therefore, the study of small cluster (usually defined as $2 \leq n \leq 500$) is more interesting than that of large cluster (usually defined as $500 \leq n \leq 10^7$) because the change of physical property is more pronounced and dramatic for small cluster when add or remove one atom.

The evolution of geometrical and electronic structure of cluster with size is still quite challenging and not very clear. How the famous tetrahedral structure of Au_{20} [16] evolves to the face-centered cubic (fcc) crystal structure of bulk gold? How the plasmon energy of 4.0 eV of Ag atom descends to the one of 3.3 eV of bulk silver [17]? Theoretically, geometrical structure and electronic structure are linked together: one of the two can be derived from the other. When we know the geometrical structure, the electronic structure can be calculated by time dependent density functional theory (TDDFT) [18, 19, 20]. Vice versa, when we know the electronic structure, the geometrical structure can be deduced as well. The electronic structure is accessible either via photoelectron spectroscopy (PES) or optical spectroscopy (OS). The geometrical structure can be determined by ion mobility measurements [21, 22, 23, 24] and electron diffraction [25, 26]. Technically for small clusters it is very difficult to observe their geometrical structure by experiments directly, thus an effective way is to detect its electronic structure first by measuring their optical properties. This is actually the idea of Mie.

The optical properties of metal clusters reveal their electronic and geometric structures, showing a fingerprint effect. Although our knowledge on the optical properties have been greatly improved over the last decades, the optical spectroscopy on small clusters was only limited to laser excitation techniques like resonant two photon ionization spectroscopy (R2PI) [27], laser induced fluorescence (LIF) [28] and photodepletion spectroscopy [29, 30] due to the low density of cluster specimens. Although big efforts have been made to enhance the cluster density by collecting them in a radiofrequency ion trap [31], limited success have been achieved. A promising way is to embed clusters in a solid rare gas matrix, which allows one to use optical absorption directly.

On one hand, small cluster has so high ratio of surface to volume that such large fraction of surface atoms make it very difficult to measure the pure property of cluster itself when embedded in a matrix due to the interaction between them on interface. On the other hand, free cluster without matrix in gas phase is also not possible to be measured because of very small target density. Hence, how to choose a perfect matrix that has the least interaction with cluster is a critical point for the study of cluster. A smart way is to use a rare gas solid as matrix at low temperature, the inert environment of which allows the study of even the most reactive particles. Among all the rare gas solid, neon provides the weakest interacting medium but technically requires the lowest sublimation temperature.

The first measurements on matrix isolated small metal clusters have been performed almost 40 years ago [32]. But the matrix with a rather wide size distribution of clusters made any spectral assignment impossible. This problem has been resolved by soft-landing mass-selected clusters into rare gas matrices [33]. This technique, developed in Lausanne and still state of the art, is commonly used in matrix isolated spectroscopy on small clusters [34, 35, 36, 37]. The advantage is that the neutral clusters with well-defined size can be investigated.

The complexity of optical properties of metal clusters starts from alkali metals, over the coinage metals to the open d-shell metals. For alkali metals, their optical properties are completely determined by s valence electrons. Among coinage metals, silver is the simplest case because of the large s-d separation, manifesting a pronounced surface plasmon. Copper is the intermediate case with small s-d separation and small relativistic effect, showing a damped surface plasmon. Gold is the most complex case since it has a small s-d separation with strong relativistic effect, implying a heavily damped surface plasmon. For open d-shell metals, the experiments are quite challenging and the results on such systems are sparse.

The optical properties of metal clusters are important in a new field called plasmonics [38, 39, 40, 41, 42]. Transition metal clusters, in particular silver and gold, have a great deal of important applications in biolabelling, nanophotonics, light energy harvesting, catalysis and so on [43, 44, 45, 46]. The plasmonic properties of these transition metals are key for the development of applications. These properties, defined by the dielectric function of the bulk materials, have been thoroughly characterized for nano-scaled particles in the framework of electromagnetic theory [47]. However, there is a particular interest in the so-called non-scalable cluster size regime where the dielectric function evolves from single molecular transitions into bulk regime and where each constituent atom counts and changes the physical property of the cluster [48, 49, 50]. For the optical properties, this is the range where molecular like electronic transitions evolve into surface plasmon whose shape depend on the symmetry of the cluster, changing smoothly for large clusters but dramatically for small ones as a function of size.

Small metal clusters are ideal objects for thorough tests of theoretical calculations since they are small enabling all electron, fully relativistic, as well as time-dependent density functional calculations. Recent progress in TDDFT allows to extend the size range for the investigation of optical properties up to more than 100 atoms for the simplest transition metal clusters [18, 19]. Therefore, there it is highly desirable and demanded to measure high quality optical spectra of small metal clusters under well-defined conditions, such as low temperature, defined cluster size, and most inert environment. For many metals, there is only limited experimental information on these studies, for some elements these are yet unknown. Measurements of optical absorption on size-selected silver clusters have been performed up to 9 atoms in Ne matrix [51] and up to 39 atoms in Ar matrix [52], and for gold and copper clusters only in Ne matrix up to 9 atoms as well [53, 54].

The realization of metal clusters stabilized in the inert gas matrix, and accessible to high-

resolution optical spectroscopy, also allows to perform surface enhanced Raman scattering (SERS) studies on very well defined structures of molecules attached to small metal clusters. Raman scattering is a powerful method to detect molecules and identify them by their vibrational fingerprint. The intrinsically weak Raman cross section (10^{-30} cm^2) can be greatly improved by SERS where the molecule is in the vicinity of a nanostructured metallic surface on a metallic nanoparticle [55]. Typical enhancement ratios of SERS are $10^3 - 10^6$ and can reach 10^{14} in particular cases.

SERS has been discovered almost 40 years ago [56, 57]. But a complete understanding has not yet been achieved. Two contributions are generally believed to enhance the Raman cross sections: chemical enhancement by resonance with a molecular transition or cluster molecule charge transfer transitions, and electromagnetic enhancement by plasmon excitation. Raman cross sections as large as 10^{-15} cm^2 have been found which makes single molecule detection possible when adsorbed on silver nanoparticles [58]. The amplification of the electrostatic field in the surface plasmon excitation of silver plays an important role in SERS. Theoretical calculations predicted large enhancement factors for molecules like pyridine (Py) attached to small silver clusters [59, 60, 61]. Giving the importance of SERS with small metal clusters for applications as well as a fundamental understanding of the underlying processes, it is highly desirable to obtain experimental data on size-selected neutral cluster molecule complexes. Freezing the Ag_aPy_b complexes in Ne matrices should provide an ideal system to measure Raman cross sections for a well-defined cluster size and environment. Based on this system, optical absorption, fluorescence and Raman spectroscopy should allow to test the theoretical predictions and thereby make a first step to the detailed understanding of the enhancement effect.

My thesis is devoted to the study of optical properties of small metal clusters. We will perform optical absorption measurements in the UV-visible range on size-selected Ag clusters in the size range $n = 20 - 120$ atoms. We expect to explore the evolution from molecular like single electron transitions into collective type transitions, the surface plasmon. This allows to trace the evolution of the dielectric function from molecules to the extended solid. Experiments will be compared to TDDFT calculations. In addition, we will perform optical absorption measurements on the famous Au_{20} in order to compare with the theoretical models. As a second step, we will perform SERS studies on size-selected Ag_aPy_b clusters in the size range $a=1,3$ and $b=1,2$. This allows us to test the theoretical models and better understand the mechanism of SERS.

For better organizing the thesis, we separated theoretical models (Chapter 2), experimental techniques (Chapter 3), and experimental results on silver clusters (Chapter 4), gold clusters (Chapter 5) and silver-pyridine compounds (Chapter 6). We hope this division increases the clarity of the presentation.

A brief overview of theoretical approaches in treating optical properties of metal clusters is given in Chapter 2. Two size effects of optical properties on metal clusters are shown here:

Chapter 1. Introduction

extrinsic size effect and intrinsic size effect. The first one is based on solid-state theory, and the optical response of the clusters follows classical electrodynamics. The second one is to calculate the optical response directly from the electronic structure of the clusters by applying quantum-mechanical methods.

A new setup for optical measurements (including absorption, fluorescence and Raman scattering) on size selected small clusters and cluster-organic compounds embedded in rare gas solid Ne matrixes is presented in Chapter 3. The object is to study the electronic structure of metal clusters and the surface-enhanced Raman scattering (SERS) of metal-organics combinations. Clusters of all elements with mass range of 1 – 16,000 amu can be fabricated and mass-selected. Simulations are shown to manifest the capability of mass-selection and transmission of cluster ions in the device. The design, construction and performance of the setup are discussed and demonstrated on the mass spectra of Ag_n ($n=1-140$), Au_m ($m=1-40$) and Ag_aPy_b ($a=1-11$, $b=1-3$).

Emphasis will be given to the experimental results of optical absorption on small silver clusters with size range of 20 – 120 atoms in Chapter 4. Results of clusters of Ag_n ($n=20, 35, 55, 58, 84, 92, 120$) are shown here and compared to TDDFT calculations. Plasmon absorption as a function of cluster size is presented. This fills the gap of silver clusters in intermediate size range of several tens of atoms [17, 62]. Clusters with atom number of 8, 18, 34, 58, 92 show a localized maximum value of plasmon energy, the numbers of which correspond to the fully filled states of 1p, 1d, 1f, 1g and 1h according to the electronic shell model, manifesting a sub-shell effect.

Experimental results of optical measurements on the gold cluster of Au_m ($m=19, 20, 21$) are shown in Chapter 5, including optical absorption, fluorescence and excitation spectra. The results have been compared to the TDDFT calculations. This helps to explore and verify the electronic as well as geometric structures (e.g. the beautiful tetrahedral structure of Au_{20} [16]).

Last but not least, results of optical measurements of absorption, fluorescence and Raman scattering on cluster-organic compounds of Ag_aPy_b ($a=1, 3$; $b=1, 2$) are shown in Chapter 6. The purpose is to test the theoretical models of SERS and better understand the mechanism of enhancement effect behind.

The Appendix lists the designs of the machine and the simulations of cluster ions that are not discussed in detail in this thesis.

2 Theory

In this Chapter, we will focus on the theoretical models of optical properties of metal clusters [47, 48, 63, 64, 65].

2.1 Size dependent optical material function of clusters

All the following theoretical calculations of optical properties of metal clusters rely on the optical material function ε .

For large clusters (with a diameter larger than about 10 nm), their dielectric functions $\varepsilon = \varepsilon(\omega)$ are size independent and have the values of bulk material. The optical response can then be calculated by classical electrodynamics. For metals the spectra are dominated by collective resonances. This kind of resonance is oftenly called as surface-plasmon or Mie resonance. The optical material functions are so important that determine not only the position but also the shape of these resonances. Due to the comparable scale of cluster size to light wavelength, a retardation effect of the electromagnetic field across the particle can cause huge shifts and broadening the resonances, if the particle size is increased. This size dependence of the optical spectra of large clusters manifests an **extrinsic cluster size effect** governed only by the dimension of the particle with respect to the light wavelength.

For small clusters (with a diameter smaller than about 10 nm), their dielectric functions $\varepsilon = \varepsilon(\omega, R)$ are size dependent and vary as a function of particle radius. The change of dielectric functions can also cause huge shifts of plasmon resonance of optical response, although the retardation effect does not play a role here due to the unmatched cluster size with light wavelength. This size dependence of the optical spectra of small clusters manifests an **intrinsic cluster size effect** governed only by the dielectric function.

Therefore, extrinsic size effect dominates for large clusters and intrinsic size effect dominates for small clusters, as shown in table 2.1.

Cluster radius R	R ≤ 10 nm	R ≥ 10 nm
Electrodynamics of Mie theory	$f = f$	$f = f(R)$
Optical material functions	$\varepsilon = \varepsilon(\omega, R)$	$\varepsilon = \varepsilon(\omega)$
Size effects	intrinsic	extrinsic

Table 2.1 – Extrinsic and intrinsic size effects of the optical response of metal clusters.

2.2 Extrinsic cluster size effects

2.2.1 Bulk metals (Drude model)

Most of bulk metals are free-electron metals, and their electronic as well as optical properties are determined completely by the conduction electrons, including alkali metals, magnesium, aluminum, and also noble metals to some extent. For free-electron metals, their valence band is fully filled by electrons, but the conduction band is only partially filled. The linear response of these metals to electromagnetic field is determined by the dielectric function $\varepsilon(\omega)$. For alkali metals, their dielectric function are governed only by the transitions within the conduction band. For other metals, interband transitions from low-lying bands to conduction band or from conduction band to higher unoccupied levels also contribute to the dielectric function. Noted that for noble metals both types of transitions exist.

(1) Free electron optical response

For free electron metals, a simple approach to the optical response is the **Drude-Lorentz-Sommerfeld model**. In this model, it assumes that all the conduction electrons are independent and fully coupled in phase. That is, the response of a metal particle can be considered first microscopically by the influence of one free conduction electron alone by external forces, and then macroscopically multiplying the effect of the single electron by the number of electrons.

The response of a free electron of mass m_e and charge e to an external electric field $\vec{E} = \vec{E}_0 e^{-i\omega t}$ can be described as:

$$m_e \frac{\partial^2 \vec{r}}{\partial t^2} + m_e \Gamma \frac{\partial \vec{r}}{\partial t} = e \vec{E}_0 e^{-i\omega t}, \quad (2.1)$$

where Γ is the damping constant. Equation 2.1 gives the dipole moment $\vec{p} = e \vec{r}$ and the polarization $\vec{P} = n \vec{p}$, where n is the number of electrons per unit volume. Introducing the polarizability α by $\vec{P} = n \alpha \vec{E}$, we have $\vec{P} = n \alpha \vec{E} = n e \vec{r}$. Using the definition of dielectric

function ε by $\varepsilon = 1 + \vec{P}/(\varepsilon_0 \vec{E})$, we get:

$$\varepsilon - 1 = \frac{1}{\varepsilon_0} n\alpha = \frac{1}{\varepsilon_0} ne \frac{\vec{r}}{E}. \quad (2.2)$$

Solving equation 2.1 and substituting \vec{r} into 2.2, we obtain:

$$\varepsilon(\omega) = 1 - \frac{\omega_p^2}{\omega^2 + i\Gamma\omega} = 1 - \frac{\omega_p^2}{\omega^2 + \Gamma^2} + i \frac{\omega_p^2 \Gamma}{\omega(\omega^2 + \Gamma^2)} = \varepsilon_1(\omega) + i\varepsilon_2(\omega), \quad (2.3)$$

where

$$\omega_p = (ne^2/\varepsilon_0 m_e)^{1/2} \quad (2.4)$$

is the Drude plasma frequency. The damping constant (or say relaxation constant) Γ can be related to the electron mean free path ℓ by $\Gamma = v_F/\ell$, where v_F is the Fermi velocity. For $\omega \gg \Gamma$, we have:

$$\varepsilon_1(\omega) \approx 1 - \frac{\omega_p^2}{\omega^2}, \quad \varepsilon_2(\omega) \approx 1 - \frac{\omega_p^2}{\omega^3} \Gamma. \quad (2.5)$$

We can see from equation 2.5 that $\omega = \omega_p$ when $\varepsilon_1(\omega) = 0$. Namely, the resonance ($\omega = \omega_1$) occurs when:

$$\varepsilon_1(\omega_1 = \omega_p) = 0. \quad (2.6)$$

This plasma frequency of ω_p is also called the **volume plasmon** frequency. The real part of the dielectric function describes the polarization, and the imaginary part of the dielectric function describes the dissipation of matter, respectively.

It is common to express the dielectric function $\varepsilon(\omega)$ in terms of the electric susceptibility χ , as:

$$\varepsilon(\omega) = 1 + \chi^{DS}(\omega), \quad (2.7)$$

where $\chi^{DS}(\omega)$ denotes the free-electron Drude-Sommerfeld susceptibility.

(2) Interband transitions

Until now, only conduction electrons have been treated. However, all other electrons in deeper levels also contribute to the dielectric function. The influence of interband transition gives an additional contribution $\chi^{IB}(\omega)$ to the susceptibility. The resulting dielectric function is determined by the band structure $E(\vec{k})$ and transition matrix elements M_{if} , describing the interband transition between initial (i) and final (f) state. Using the electric-dipole approximation for the electron-photon interaction, the expression of $\chi^{IB}(\omega)$ can be written as [47]:

$$\chi^{IB} = \frac{8\hbar^3 \pi e^2}{m_{eff}^2} \sum_{i,f} \int_{BZ} \frac{2d\vec{k}}{(2\pi)^3} |\vec{e} M_{if}(\vec{k})|^2 \left\{ \frac{1}{[E_f(\vec{k}) - E_i(\vec{k})][(E_f(\vec{k}) - E_i(\vec{k}))^2 - \hbar^2 \omega^2]} + i \frac{\pi}{2\hbar^3 \omega^2} \delta[E_f(\vec{k}) - E_i(\vec{k}) - \hbar\omega] \right\}. \quad (2.8)$$

In this equation, the integral is over the Brillouin zone and \vec{e} is the unit vector along the direction of the electric field. Therefore, the total complex dielectric function including the interband transitions (as shown in figure2.1) is given by:

$$\varepsilon(\omega) = 1 + \chi^{DS}(\omega) + \chi^{IB}(\omega). \quad (2.9)$$

Thus the real part of dielectric function can be expressed as:

$$\varepsilon_1(\omega) = \varepsilon_1^{DS}(\omega) + \chi^{IB}(\omega). \quad (2.10)$$

Assuming that the matrix elements are independent of wavevector, i.e. constant throughout the Brillouin zone, the imaginary part of $\chi_2^{IB}(\omega)$ can be expressed as:

$$\chi_2^{IB}(\omega) \propto \frac{1}{\omega^2} \sum_{i,f} |M_{if}|^2 J_{if}(\omega), \quad (2.11)$$

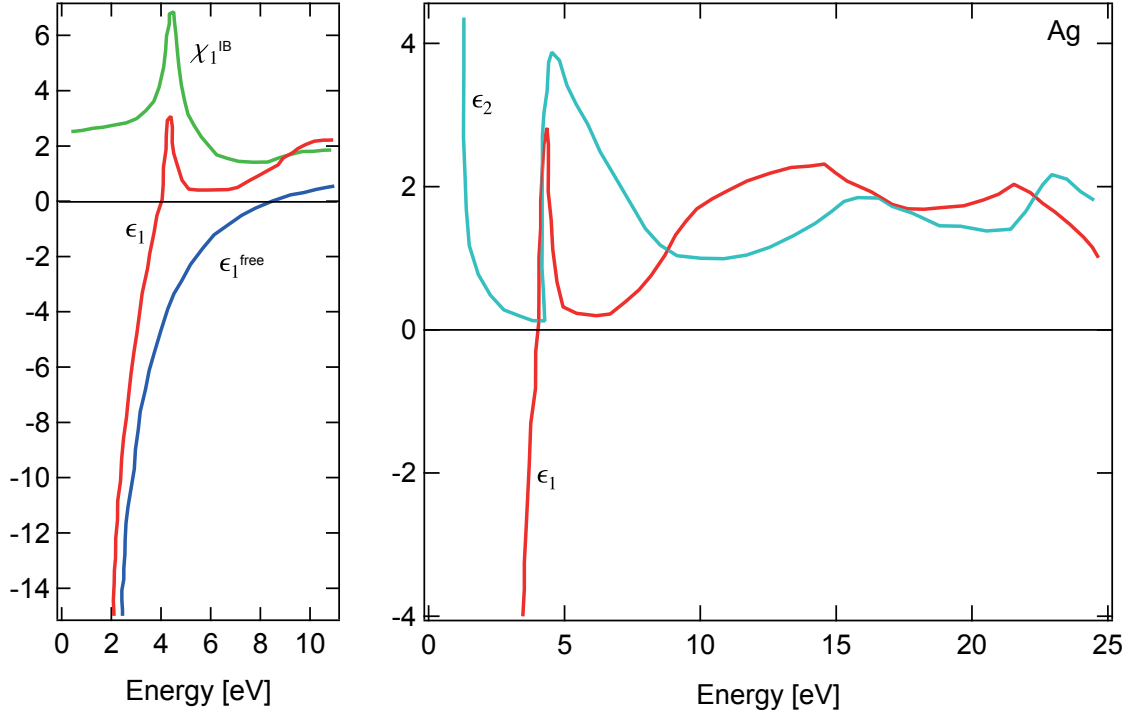


Figure 2.1 – Left: Decomposition of measured $\epsilon_1(\hbar\omega)$ into the free electron contribution ϵ_1^{free} (Drude) and the interband transition contribution χ_1^{IB} . Due to χ_1^{IB} , the plasmon energy for $\epsilon_1(\hbar\omega) = 0$ is red-shifted by about 5 eV from the free electron value. Right: Dielectric functions $\epsilon_1(\hbar\omega)$ and $\epsilon_2(\hbar\omega)$ for bulk solid silver. Below about 4 eV $\epsilon(\hbar\omega)$ is dominated by free electron behavior, above 4 eV by interband transition [47].

where $J_{if}(\omega)$ is the joint density of states given by the integral over the Brillouin zone:

$$J_{if}(\omega) = \frac{2}{(2\pi)^3} \int_{BZ} d^3\vec{k} \delta[E_f(\vec{k}) - E_i(\vec{k}) - \hbar\omega]. \quad (2.12)$$

The real part of $\chi_1^{IB}(\omega)$ can be calculated using Kramers-Kronig relation between $\epsilon_1(\omega)$ and $\epsilon_2(\omega)$.

2.2.2 Quasistatic response of a small metal sphere

For a small metal sphere ($R \ll \lambda$), the understanding of the optical response can be facilitated by the application of electrostatics. The positive charges in the clusters (i.e. core) are assumed to be immobile and the negative charges (i.e. conduction band) are allowed to move under the external field. Thus a displacement between the positive charges and the negative ones occurs if a metal cluster is placed in an external field. Using the boundary conditions at the

Chapter 2. Theory

sphere surface, the static polarizability of a small sphere can be calculated as:

$$\alpha = 4\pi\epsilon_0 R^3 \frac{\epsilon - \epsilon_m}{\epsilon + 2\epsilon_m}. \quad (2.13)$$

In the special case of metals we have $\epsilon(0) = -\infty$ and this leads to the classical static electric polarizability:

$$\alpha_{cl} = 4\pi\epsilon_0 R^3. \quad (2.14)$$

The polarizability shows resonance behavior when:

$$\begin{aligned} |\epsilon + 2\epsilon_m| &= Minimum, \\ i.e. \quad [\epsilon_1(\omega) + 2\epsilon_m]^2 + [\epsilon_2(\omega)]^2 &= Minimum. \end{aligned} \quad (2.15)$$

Therefore, the resonance ($\omega = \omega_1$) occurs when:

$$\epsilon_1(\omega_1) = -2\epsilon_m. \quad (2.16)$$

Here ϵ_m shows a medium effect. In vacuum ($\epsilon_m = 1$), we find the resonance position at:

$$\omega_1 = \frac{\omega_p}{\sqrt{3}}, \quad (2.17)$$

or inserting equation 2.14 at the frequency:

$$\omega_1 = \sqrt{\frac{Ne^2}{m_e \alpha_{cl}}}, \quad (2.18)$$

where N denotes the total number of conduction electrons in the sphere.

Sometimes the ω_1 of equation of 2.17 is interpreted as the classical **surface plasmon** frequency. Plasmon conditions for various sample geometries are compiled in table 2.2.

Geometry	Resonance condition	Resonance frequency
Bulk metal	$\varepsilon_1(\omega) = 0$	$\omega_1 = \omega_p$
Planar surface	$\varepsilon_1(\omega) = -1$	$\omega_1 = \frac{\omega_p}{\sqrt{2}}$
Thin film	$\frac{\varepsilon_1+1}{\varepsilon_1-1} = \pm \exp[-(\vec{k})_x d]$	$\omega_1 = \frac{\omega_p}{\sqrt{2}} \sqrt{1 \pm \exp[-(\vec{k})_x d]}$
Sphere (dipole mode)	$\varepsilon_1(\omega) = -2$	$\omega_1 = \frac{\omega_p}{\sqrt{3}}$
Ellipsoid (dipole mode)	$\varepsilon_1(\omega) = -\frac{1-\tilde{L}_m}{\tilde{L}_m}$	$\omega_1 = \omega_p \tilde{L}_m$

Table 2.2 – Plasma resonance positions for various sample geometries in vacuum ($\varepsilon_m = 1$). \tilde{L}_m denotes the depolarization factor, d is the film thickness and x gives the direction parallel to the film.

2.2.3 Electrodynamic calculation of a small metal sphere (Mie theory)

The above discussion of the quasi-static regime serves as a first rough estimate which only holds for sufficiently small particles and needs to be extended considerably in order to account for larger particle sizes. The general solution of the diffraction problem of a single sphere of arbitrary material within the frame of electrodynamics was first put forward by **Mie** in 1908 [8]. He applied Maxwell's equations with appropriate boundary conditions in spherical coordinates using multipole expansions of the incoming electric and magnetic field, as shown in figure 2.2. The input parameters were the particle size and the optical functions of the particle material and of the surrounding medium. Note that, all Mie theory calculations are restricted to electrically neutral clusters.

It is common to express the optical properties in terms of absorption and scattering cross sections σ_{abs} and σ_{sca} . Following the Lambert-Beer law, we have:

$$\begin{aligned} \Delta I_{abs}(z) &= I_0(1 - e^{-\# \sigma_{abs} z}) \\ \Delta I_{sca}(z) &= I_0(1 - e^{-\# \sigma_{sca} z}), \end{aligned} \quad (2.19)$$

where $\#$ is the number density of clusters. Hence, the extinction cross section, contributed by both absorption and scattering, is given by:

$$\sigma_{ext} = \sigma_{abs} + \sigma_{sca}. \quad (2.20)$$

The extinction, scattering, and absorption cross sections can be calculated from Mie theory by

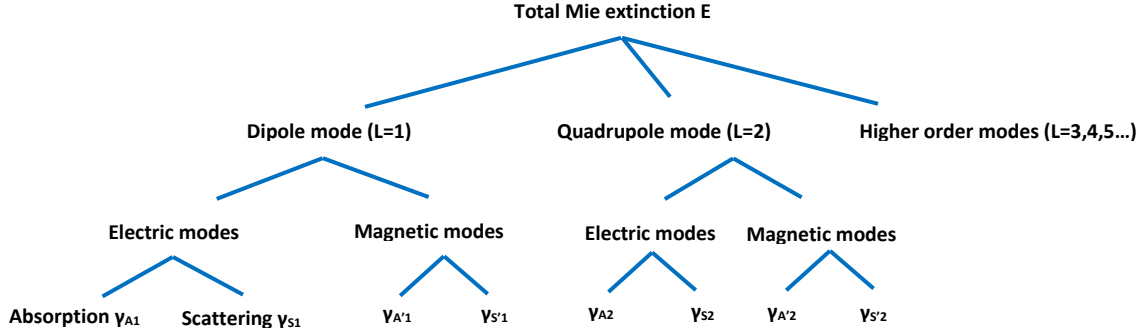


Figure 2.2 – Scheme for decomposing the total Mie extinction spectra in dipolar, quadrupolar and higher modes of electronic excitations. Each multipole contributes by electric and magnetic modes, i.e. plasmons and eddy currents which each consist of absorption and scattering losses [47].

series expansion of the involved fields into partial waves of different spherical symmetries:

$$\begin{aligned}\sigma_{ext} &= \frac{2\pi}{|\vec{k}|^2} \sum_{L=1}^{\infty} (2L+1) \text{Re}(a_L + b_L) \\ \sigma_{sca} &= \frac{2\pi}{|\vec{k}|^2} \sum_{L=1}^{\infty} (2L+1) (|a_L|^2 + |b_L|^2) \\ \sigma_{abs} &= \sigma_{ext} - \sigma_{sca},\end{aligned}\tag{2.21}$$

with

$$\begin{aligned}a_L &= \frac{m\psi_L(mx)\psi'_L(x) - \psi'_L(mx)\psi_L(x)}{m\psi_L(mx)\eta'_L(x) - \psi'_L(mx)\eta_L(x)} \\ b_L &= \frac{\psi_L(mx)\psi'_L(x) - m\psi'_L(mx)\psi_L(x)}{\psi_L(mx)\eta'_L(x) - m\psi'_L(mx)\eta_L(x)}.\end{aligned}\tag{2.22}$$

Here $m = n/n_m$, where n denotes the complex index of refraction of the particle and n_m the real index of refraction of the surrounding medium. \vec{k} is the wavevector and $x = |\vec{k}|R$ the size parameter. $\psi_L(z)$ and $\eta_L(z)$ are Riccati-Bessel cylindrical functions. The prime indicates differentiation with respect to the argument in parentheses.

The summation index L gives the order of the partial wave, thus is the order of spherical multipole excitations in the clusters. $L = 1$ corresponds to dipole fields, $L = 2$ to quadrupole, $L = 3$ to octupole fields and so on, as shown in fig2.3.

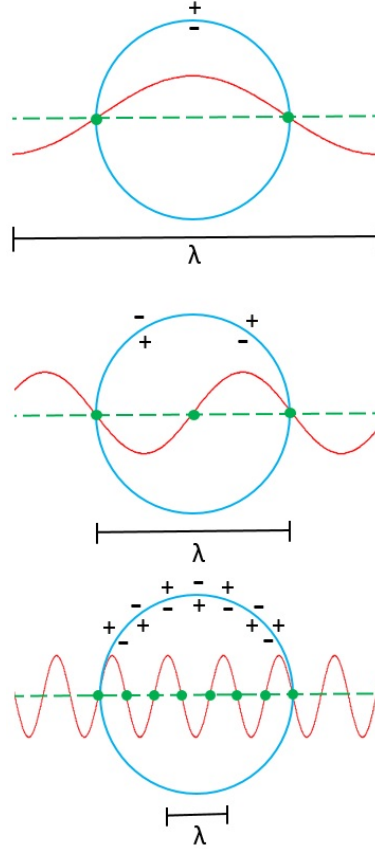


Figure 2.3 – Top: Dipole mode ($L = 1$); Mid: Quadrupole mode ($L = 2$); Down: Multipole mode ($L > 2$) of Mie theory.

Before presenting numerical results of the complete electrodynamic calculation, it is worth analyzing the resonance frequencies of plasmon of metal clusters in the quasi-static regime. In this case ($R \ll \lambda$), phase retardation and effects of higher multipoles are neglected and the Mie formula is simplified considerably. Thus equation 2.21 yields as the lowest order term:

$$\sigma_{ext} = 9 \frac{\omega}{c} \epsilon_m^{3/2} V_0 \frac{\epsilon_2(\omega)}{[\epsilon_1(\omega) + 2\epsilon_m]^2 + \epsilon_2(\omega)^2}. \quad (2.23)$$

Here $V_0 = (4\pi/3)R^3$ denotes the particle volume, ϵ_m is the dielectric function of the embedding medium, and ϵ is the dielectric function of the particle material. This extinction cross section is due to dipolar absorption only. Again, the condition of resonance is simplified to $\epsilon_1(\omega) = -2\epsilon_m$. Figure 2.4 shows dielectric function of $\epsilon_1(\omega)$ and $\epsilon_2(\omega)$ of bulk metals and the effective absorption section of metal spheres of copper, silver and gold.

For free electron metals with $\omega \gg \Gamma$ the resonance position and shape can be approximated

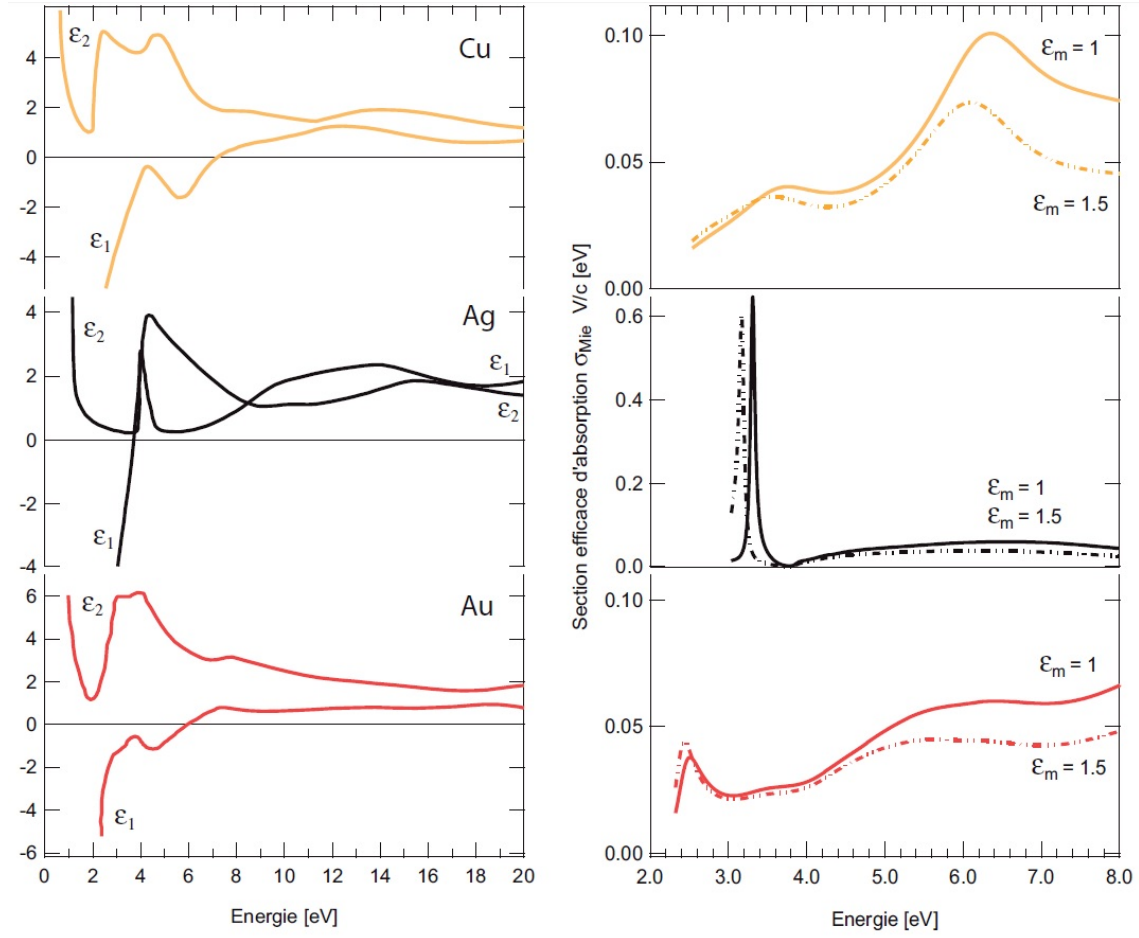


Figure 2.4 – Left: Dielectric function of $\epsilon_1(\omega)$ and $\epsilon_2(\omega)$ of a bulk metal. Right: The effective absorption section of a metal sphere using Mie theory. [66]

by inserting equation 2.5 into 2.23. In the vicinity of the resonance, the lineshape is then described by a Lorentzian:

$$\sigma_{ext} = \sigma_0 \frac{1}{(\omega - \omega_1)^2 + (\Gamma/2)^2}. \quad (2.24)$$

The resonance position follows from equation 2.23 as $\omega_1 = \omega_p / \sqrt{1 + 2\epsilon_m}$. For the positions of higher multipole orders in the quasi-static limit of Mie theory, we have:

$$\omega_L = \omega_p \frac{1}{\sqrt{1 + \frac{L+1}{L}\epsilon_m}}. \quad (2.25)$$

Up to now we have assumed the presence of one single Mie resonance for each L which is by no means the general case.

2.2.4 Extrinsic size effect

For large clusters in the cluster size range from 10 to 100 nm, the quasi-static approximation does not hold anymore, and extrinsic size effects due to retardation of the fields across the cluster come into play.

It is difficult to prepare samples of monodisperse clusters of a given size. Clusters in matrices or on surfaces commonly have size distributions of considerable width.

Symmetric distributions are usually described by the Gaussian distribution, also called normal distribution:

$$f_{Normal}(R) = \frac{1}{\sqrt{2\pi}\sigma} \exp\left(-\frac{(R - R_0)^2}{2\sigma^2}\right), \quad (2.26)$$

where σ is the standard deviation. This equation frequently describes colloidal systems.

Asymmetries the distributions can be described by two half-Gaussian functions of different widths, centered around the maximum value R_0 :

$$f_{Gauss,\pm}(R) = C \exp\left(-\frac{(R - R_0)^2}{2\sigma_{\pm}^2}\right), \quad (2.27)$$

where σ_+ holds for $R \geq R_0$ and σ_- holds for $R \leq R_0$. The full width at half maximum (FWHM) is related to the standard deviation σ by $\text{FWHM} = (2 \ln 2)^{1/2}(\sigma_+ + \sigma_-)$. C is determined by the normalization $\int f(R) dR = 1$.

Alternatively cluster samples produced by gas aggregation can be quantitatively modeled using the *log* normal distribution as below:

$$f_{\log}(R) = \frac{1}{\sqrt{2\pi} \ln(\beta)} \exp\left(-\frac{[\ln(R) - \ln(R_0)]^2}{2 [\ln(\beta)]^2}\right), \quad (2.28)$$

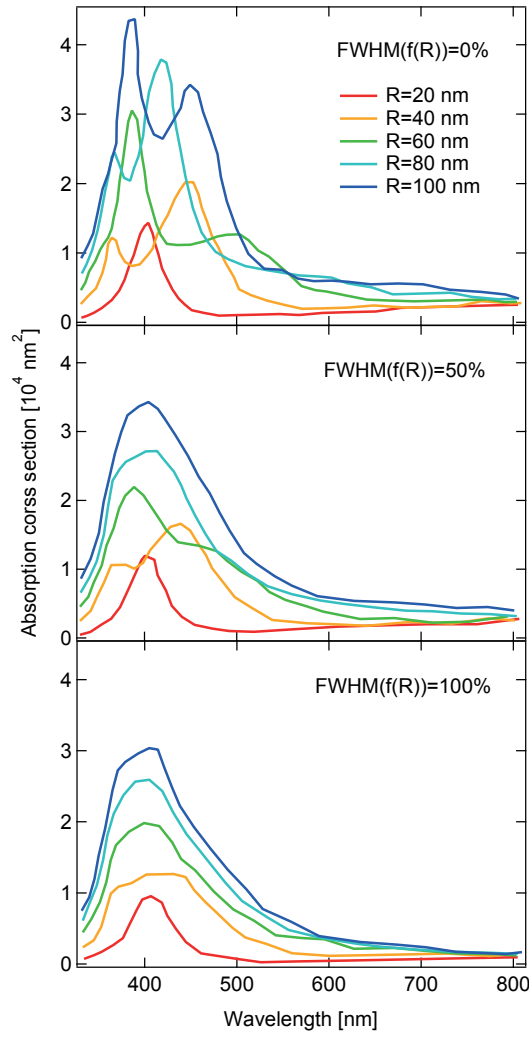


Figure 2.5 – Absorption cross section as function of wavelength for size distributed free sodium clusters in vacuum with fixed mean cluster sizes $R = 20$ nm, 40 nm, 60 nm, 80 nm and 100 nm, and full width at half maximum (FWHM) of the cluster size distribution of 0%, 50% and 100%, respectively. [47]

where β is a measure of the width of the distribution. If the cluster size distributions are narrow it is difficult to distinguish between the *lognormal* and the *normal* distribution. As optical material functions the data for bulk sodium were chosen for the wavelength region from 330 nm to 800 nm. Several important features can be illustrated with figure 2.5.

(1) For monodisperse particles (FWHM=0) of 20 nm mean radius, the absorption cross section is dominated by the dipole resonance, centered around $\lambda_1 = 400$ nm. The electrostatic approximation without phase-retardation effects would lead to a size-independent resonance at $\lambda_1 = 384$ nm for the dipolar mode. Although the particle size is only 10% of the wavelength of the light, the shift introduced by phase retardation amounts to about 16 nm, still showing a

small extrinsic effect.

(2) With increasing cluster radius, higher order resonances come into play in the absorption cross section. For $R = 40$ nm, the quadrupole oscillation becomes clearly visible and even overcomes the dipole contribution for $R = 60$ nm. Further increase in particle size leads to octupole resonances and for $R = 100$ nm the dipole resonance is even negligible.

(3) The change of the absorption cross section due to nonzero width of the cluster size distribution is pronounced. Clearly seen from figure 2.5 (from top to down), the structures due to the various multipoles are smeared out when the FWHM increases, leading to larger apparent widths of the resonances. However, the position of the peaks is not affected seriously.

Cathedral colorful stained glass is a good example to show the extrinsic effect of metal clusters. The wavelength of absorption light changes with the size of metal clusters embedded in the window.

The width of the cluster size distribution has also another interesting consequence. For $R \ll \lambda$, absorption is proportional to $(|\vec{k}|R)^3/|\vec{k}|^2$ and for scattering to $(|\vec{k}|R)^6/|\vec{k}|^2$. As a consequence, for broad size distributions the resulting extinction spectra are dominated by the largest heavily scattering particles.

Mie theory is not specific to any type of material and can be applied to the interaction of light with any sphere of given dielectric function, for instance, also for the rainbow produced by water droplets. However, this is a tedious calculation because the cluster sizes are of the order or even larger than the wavelength and hence a very large number of multipoles have to be considered.

2.3 Intrinsic cluster size effects

The dielectric function of $\varepsilon(\omega)$ represents a system rather than a material quantity since it includes surface effect which, in turn, are closely related to the cluster size. As shown in table 2.1, if sizes are large, size dependencies of the Mie absorption are caused by electrodynamic effects. We have called these effects extrinsic, being due to size dependent interference of the retarded electromagnetic scattering fields outside the clusters.

We defined as **extrinsic** size effect those properties of the Mie spectra depending on R and bulk dielectric functions $\varepsilon(\omega)$ that occurs for sizes above $2R = 10$ nm, and **intrinsic** size effect which results from the cluster material in the form of size dependent dielectric functions $\varepsilon(\omega, R)$ that occurs in quasi-static regime ($R \ll \lambda$) where the electrodynamic effects vanish. Hence, the two kinds of effects are automatically separated from each other: at small sizes, there are only intrinsic size effects and at large sizes, the extrinsic ones dominate.

Intrinsic size effects can be due to many different reasons. they reflect changes of the atomic structure of the cluster, and the influence of the cluster surface. The dielectric function,

defined as an average over microscopic polarizabilities, changes in clusters due to the limited volume for averaging, the existence of the surface, inhomogeneities of the charge densities, local polarizabilities etc., that means generally changes of the electric and the atomic structure across the cluster.

2.3.1 Size dependent optical material functions

Some general features of $\varepsilon(\omega, R)$ are obvious:

$$\begin{aligned} \varepsilon(\omega, R \rightarrow \infty) &= \varepsilon(\omega, \text{bulk}) \\ |\varepsilon(\omega, R \rightarrow R_{\text{atom}})| &\text{ is finite} \end{aligned} \quad (2.29)$$

A common feature of small particles is that the additional contribution to Γ_∞ which called $\Delta\Gamma(R)$ is proportional to $(1/R)$. Therefore Γ in the Drude dielectric function of 2.3 is replaced by:

$$\Gamma(R) = \Gamma_\infty + \Delta\Gamma(R) = \Gamma_\infty + A \frac{\nu_F}{R}, \quad (2.30)$$

where the parameter of A is a theory-dependent quantity of the order of 1. For small particles, surface scattering obviously becomes the dominant contribution to the relaxation. The $(1/R)$ law simply reflects the ratio of surface scattering probability (being proportional to the surface area $4\pi R^2$) and the number of electrons (which is proportional to the volume $\frac{4\pi}{3} R^3$), that is the surface to volume ratio.

Early quantum mechanical concepts for clusters started from the solid state physics point of view. Soon afterwards people realized that the continuous electronic conduction band of a solid should break up into discrete states (levels) if the dimensions of the metal become small enough. Towards large cluster sizes the number of levels increases while the gap width decreases, finally leading to the band structure of the bulk.

A starting point for the calculation of the optical response of metal clusters is the polarizability or the dielectric function of the cluster material, including the influence of the confining surface. If the metal clusters are so small that the conduction band breaks up into the discrete levels separated by energies δ large compared to thermal energies ($\delta > kT$) as shown in figure 2.6, and if, furthermore, the level widths due to lifetime limitations δ_i are so small compared to the level distance ($\delta_i \ll \delta$), then the Drude expression of 2.3 is no longer valid.

Ruppin and Yatom [68] have proved the similarity of various theoretical approaches regarding the prediction of the $(1/R)$ -law. Formally, $\varepsilon_2(\omega, R)$ can be decomposed into bulk contribution

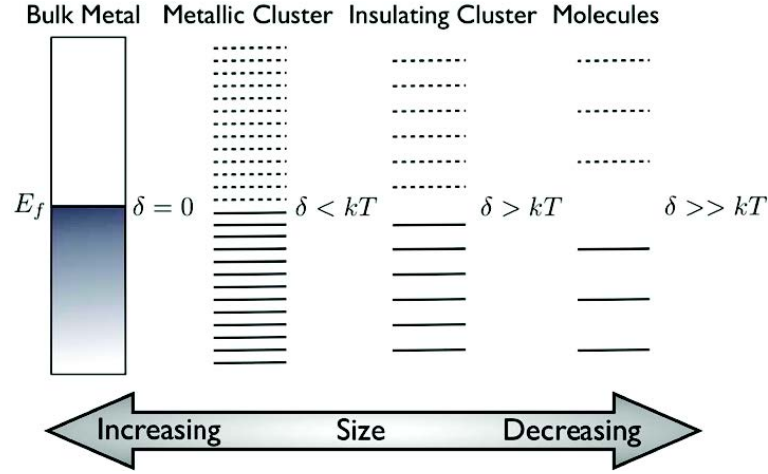


Figure 2.6 – Evolution of the band gap and the density of states as the number of atoms in a system increases (from right to left). $\delta = \frac{4E_f}{3N}$ is the so called Kubo gap, where N is the number of valence electrons and E_f is the fermi level. [67]

$\varepsilon_{2,bulk}(\omega)$ and the size-dependent free electron contribution $\chi_2(\omega, R)$:

$$\varepsilon_2(\omega, R) = \varepsilon_{2,bulk}(\omega) + \chi_2(\omega, R). \quad (2.31)$$

The term $\varepsilon_{2,bulk}(\omega)$ is determined by the limit $R \rightarrow \infty$ provided that χ_2 goes to zero. Ruppin and Yatom compiled various ways to determine $\chi_2(\omega, R)$ and yielded the $(1/R)$ -law:

$$\chi_2(\omega, R) = Z_j \frac{e^2}{\hbar\omega} \frac{1}{v^2} g_j(v) \frac{1}{R}, \quad (2.32)$$

with $Z_j = 32/\pi^3$, $4/\pi$, and $12/\pi^2$ for the sphere, the film and the cylinder geometry, respectively. R denotes the radius of sphere and cylinder and half the thickness of the thin film. The functions $g_j(v)$ of the variable $v = \hbar\omega/E_F$ are monotonic functions close to unity with E_F being the Fermi energy.

The $(1/R)$ -law appears to be universal for $\varepsilon_2(\omega, R)$ and $\Gamma_2(R)$. One fundamental problem still open: the limiting case $\chi_2(R \rightarrow 0) \rightarrow \infty$ has no physical meaning, hence, a lower limit at some finite R must occur where the $(1/R)$ -law begins to fail.

2.3.2 Direct quantum mechanical calculations (Jellium approximation)

The theory discussed in Section 2.3.1 introduced a complex, cluster volume averaged, $\varepsilon(\omega)$ of the cluster material, yielding the optical response of the clusters if $\varepsilon(\omega)$ is inserted into the Mie equations.

The interaction of metal clusters with visible light usually gives rise to excitations of electrons. Energies of vibrational or rotational excitations lie in the infrared spectral region and thus beyond the scope of this Chapter.

In small clusters, the single-electron transitions directly reflect allowed transitions between different individual electronic levels. For larger sizes, the additional collective excitations of the metal electrons constructed from the single-electron transitions are the plasma or Mie resonances. Since this Section is restricted to clusters with $2R \ll \lambda$, collective excitations refer here to the dipole resonance alone. Currently, the question of how collective excitations emerge from molecular excitations is one of the most intensely discussed topics in cluster physics.

Quatum-mechanical studies of small metal clusters can be done either with quantum-chemical methods or with approaches borrowed from solid-state quantum theory. Although being successful in studying ground-state electronic properties, especially for very small clusters, quantum-chemical all-electron calculations of larger clusters are limited by available time and capacity of computers. In contrast, some simpler methods, like jellium approximation, give reasonable results for large and small clusters but have apparent limitations for very small clusters.

The **jellium approximation** commonly used for simple-metal crystals neglects the structure of the ion lattice and replaces it by a uniform, positively charged background. In the jellium theories, the electrons move in fact in one central potential of the whole cluster which then resembles a giant atom. Consequently, like atoms, the electron eigenfunctions are labelled by the quadrupole of quantum number ν , l , m , and s . The states are filled with electrons according to the Pauli exclusion principle. Whenever $2(2l + 1)$ states are occupied for a given l , it is called a completely filled l -shell. Then the total angular momentum is zero. Such clusters are proved to be very stable, assigned as clusters with electronic magic number. For spherical symmetry they are 2, 8, 18, 20, 34, 40, 58, 68, 70, 92, etc, as shown in table 2.3. The geometric magic numbers of hard sphere packing structures have also been listed, which have been used to describe abundances of rare gas clusters.

According to Lushnikov [69] and Ekardt [70], the position of the collective dipole resonance can be estimated if we assume that all the optical oscillator strength is stored in just one collective

Geometrical magic numbers	Number of atomic shells	Electronic magic numbers	Last filled electronic shell
1	0	2	1s
13	1	8	1p
55	2	18	1d
147	3	20	2s
309	4	34	1f
561	5	40	2p
923	6	58	1g
1415	7	68	2d
2057	8	70	3s
2869	9	92	1h
⋮	⋮	⋮	⋮

Table 2.3 – Geometric and electronic magic numbers of the metal clusters.

mode, namely the surface-plasmon mode. The peak position is as given by equation 2.18:

$$\omega_1 = \sqrt{\frac{Ne^2}{m_e \alpha}}. \quad (2.33)$$

With α_{cl} being the classical static polarizability, equation 2.33 can be written as:

$$\omega_1 = \frac{\omega_p}{\sqrt{3}} \sqrt{\frac{\alpha_{cl}}{\alpha}}. \quad (2.34)$$

This means that, as long as the static polarizability $\alpha(0)$ of a cluster is enhanced with respect to the bulk value, the surface-plasmon resonance is red-shifted.

2.3.3 Shell model for simple metal clusters

Up to the early 1980s clusters were primarily thought of as small molecules. However, this changed in late 1983 when Walter Knight's group, with Keith Clemenger, Walt de Heer, and Winston Saunders, produced and detected clusters of alkali metals with up to about 100 atoms. They found a striking order from the cluster abundance spectra : clusters in which the number of valence electrons matched the spherical shell closing numbers were produced more abundantly, as seen in figure 2.7, reflecting a shell structure. By a coincidence, Ekardt independently and simultaneously predicted this shell structure in his model for alkali clusters

using the jellium approach.

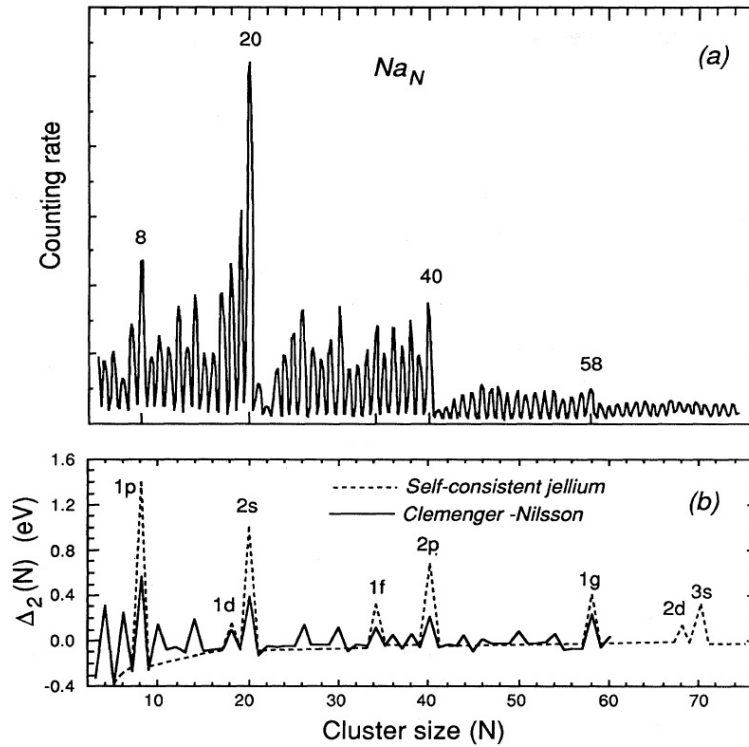


Figure 2.7 – Sodium cluster abundance spectrum: (a) experimental; (b) dashed line, using Wood-Saxon potential; solid line, using the ellipsoidal shell model. [63]

For monovalent simple metals, the conduction band is approximately free-electron-like and the Fermi surface is nearly spherical. For sodium especially, deviations from a perfect sphere are almost negligible. Correspondingly, the jellium model ignores the ionic core structure altogether and replaces it by a uniform positive background, and this approach has led to valuable insights into the electronic structure of bulk metals.

In contrast with the jellium calculations, a related semiempirical model - shell model - based essentially on the Sommerfeld model takes for granted that a very simple effective single-particle potential is a good starting point.

(1) Shell model for spherical metal clusters

In metal cluster physics the quantum numbers follow the nuclear (i.e., not the atomic) convention, so that each shell is characterized by the radial quantum number n and the angular momentum l . For a given quantum number l , the lowest state has $n = 1$, etc. Figure 2.8 shows the energy-level structure for three spherically symmetric wells, and it can be seen that changing the well shape not only changes the relative level spacings, but may even alter their ordering.

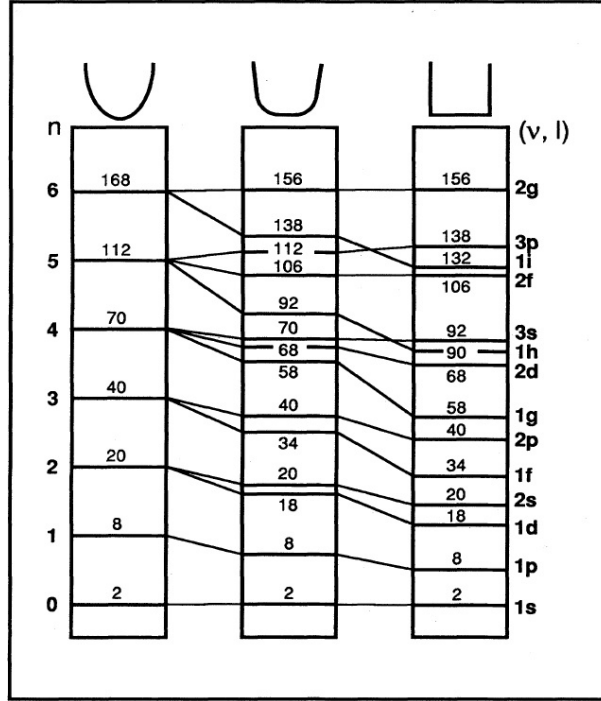


Figure 2.8 – Energy-level occupations for spherical three-dimensional, harmonic, intermediate, and square-well potentials. [63]

For comparison, figure 2.9 shows the calculated self-consistent effective single-particle potential for Na_{40} . The energy levels are also shown and the shell structure is clearly discernable. This particular self-consistent potential well has the shape of a wine bottle, and the energy-level spacings approximately correspond to those of the intermediate case in figure 2.8.

Now we examine the properties of a three-dimensional harmonic oscillator. The effective single-particle Hamiltonian for electrons with mass m is:

$$H = \frac{\vec{p}^2}{2m} + \frac{m\omega_0^2 \vec{q}^2}{2} - U\hbar\omega_0[l^2 - n(n+3)/6], \quad (2.35)$$

where \vec{p} and \vec{q} are single-electron momentum and coordinate operators, l is the angular momentum, n is the shell number, and U is the anharmonic distortion parameter. $U = 0$ corresponds to the harmonic oscillator.

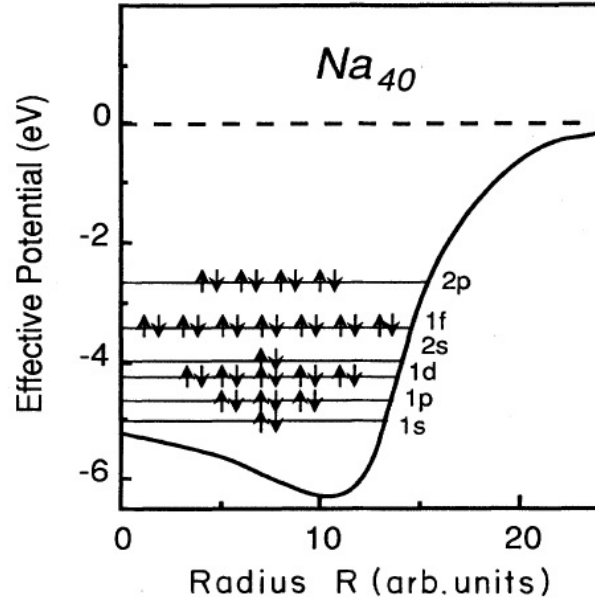


Figure 2.9 – Self-consistent effective potential of jellium sphere corresponding to Na_{40} with the electron occupation of the energy levels. [63]

The spherical shell model predicts an energy eigenvalue spectrum:

$$E_n = \hbar\omega_0 \left\{ \left(n + \frac{3}{2} \right) - U[l^2 - n(n+3)/6] \right\}. \quad (2.36)$$

These levels as a function of U are shown in figure 2.10.

(2) Spheroidal Clemenger-Nilsson shell model

Approximating small clusters with spheres can be only be justified for closed-shell clusters. From the Jahn-Teller theorem it follows that open-shell clusters must distort. As demonstrated by Clemenger, the fine structure in figure 2.7(a) is a manifestation of these distortions. Clemenger introduced a deformable potential well that is particularly well suited to account for this effect.

The Clemenger-Nilsson model assumes that the effective single-particle potential is essentially that of a three-dimensional harmonic oscillator. This turns out to be a good approximation for smaller clusters (i.e. $N < 20$). For larger ones, a small anharmonic distortion term is required.

An important feature of the model is that its shape adjusts to the electronic structure while keeping the volume of the cluster fixed. In this way spheroidal cluster (i.e. with two equal axes

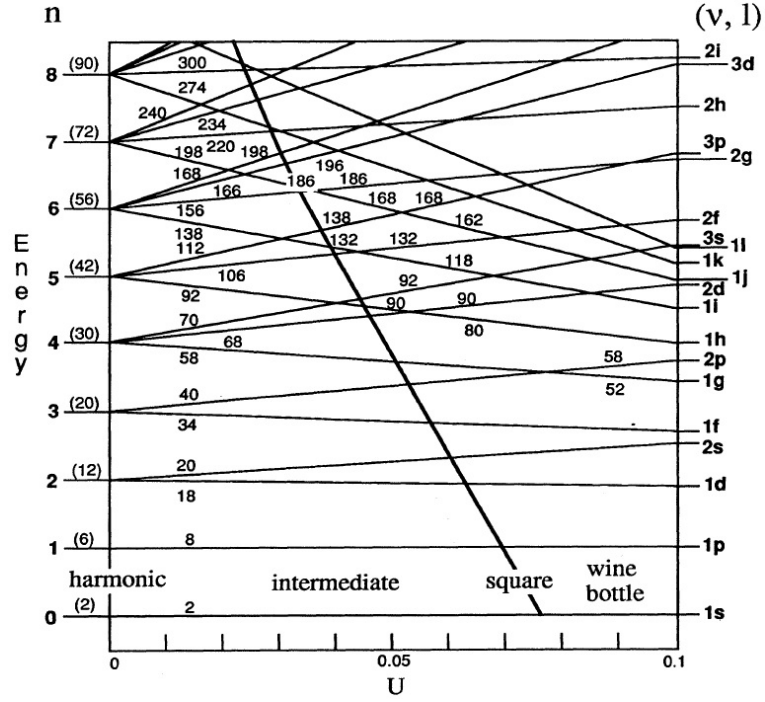


Figure 2.10 – Single-particle energy levels as a function of the anharmonic distortion parameter U . [63]

$R_x = R_y$ and one unequal axis R_z) can be treated.

As in the spherical shell model, the spheroidal shell model predicts enhanced stabilities for closed-shell clusters. However, in addition, the spheroidal distortions cause sub-shell closings which are also seen in the spectra. Hence this model reproduces not only the main features but also most of the fine structure in the abundance spectrum, as shown in figure 2.7(b).

The basic assumption of the Clemenger-Nilsson model is that for fixed volume the cluster shape adjusts to minimize the total electronic energy. Ignoring the anharmonic term of U gives the eigenvalues as a function of the shape:

$$E(n_x, n_y, n_z) = h\omega_0 \left[\left(n_x + \frac{1}{2}\right) \frac{R_0}{R_x} + \left(n_y + \frac{1}{2}\right) \frac{R_0}{R_y} + \left(n_z + \frac{1}{2}\right) \frac{R_0}{R_z} \right], \quad (2.37)$$

where R_x , R_y and R_z are the semiaxes of the ellipsoid, and n_x , n_y and n_z are the harmonic-oscillator quantum numbers ($n_x + n_y + n_z = n$). For example: for the 1s state, $(n_x, n_y, n_z) = (0, 0, 0)$; for the 1p, they are $(1, 0, 0)$, $(0, 1, 0)$ and $(0, 0, 1)$; for the 1p, they are $(1, 0, 0)$, $(0, 1, 0)$ and $(0, 0, 1)$ etc. All the details are shown in table 2.4. The volume are constrained by $R_x R_y R_z = R_0^3$.

Chapter 2. Theory

Hence the energy of cluster with the index of N (e.g. Ag_N) is:

$$E_N = \sum_{i=1}^N E(n_x, n_y, n_z)^i = \sum_{i=1}^N \left\{ h\omega_0 \left[(n_x^i + \frac{1}{2}) \frac{R_0}{R_x} + (n_y^i + \frac{1}{2}) \frac{R_0}{R_y} + (n_z^i + \frac{1}{2}) \frac{R_0}{R_z} \right] \right\}. \quad (2.38)$$

Using the conditions of $R_x = R_y$ and $R_x R_y R_z = R_0^3$ and minimizing the energy of equation 2.38, we obtained the shape of cluster as a function of (n_x, n_y, n_z) :

$$\begin{aligned} R_x &= R_0 \left[\frac{\sum_{i=1}^N (n_x^i + n_y^i + 1)}{\sum_{i=1}^N (2n_z^i + 1)} \right]^{\frac{1}{3}}, \\ R_y &= R_0 \left[\frac{\sum_{i=1}^N (n_x^i + n_y^i + 1)}{\sum_{i=1}^N (2n_z^i + 1)} \right]^{\frac{1}{3}}, \\ R_z &= R_0 \left[\frac{\sum_{i=1}^N (2n_z^i + 1)}{\sum_{i=1}^N (n_x^i + n_y^i + 1)} \right]^{\frac{2}{3}}. \end{aligned} \quad (2.39)$$

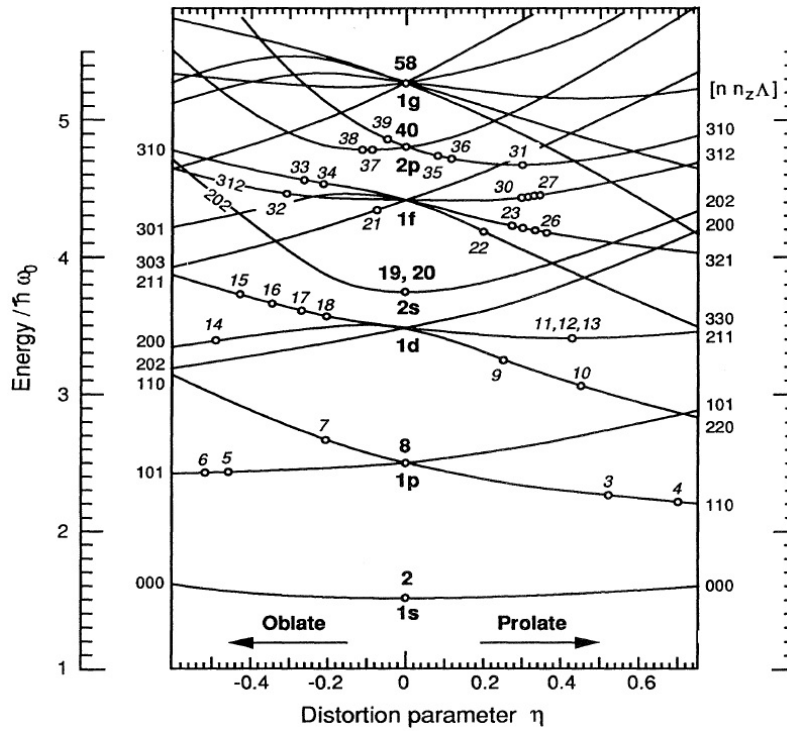


Figure 2.11 – Clemenger-Nilsson diagram. Cluster number are positioned at the highest occupied levels and at the equilibrium configuration η . [63]

2.3. Intrinsic cluster size effects

N	n	(n_x, n_y, n_z)			(v, l)
1 – 2	0	$(0, 0, 0)^{1,2}$			1s
3 – 8	1	$(1, 0, 0)^{7,8}$	$(0, 1, 0)^{5,6}$	$(0, 0, 1)^{3,4}$	1p
9 – 20	2	$(2, 0, 0)$ $(1, 1, 0)$	$(0, 2, 0)$ $(0, 1, 1)$	$(0, 0, 2)$ $(1, 0, 1)$	1d , 2s
21 – 40	3	$(3, 0, 0)$ $(1, 2, 0)$ $(2, 1, 0)$	$(0, 3, 0)$ $(0, 1, 2)$ $(0, 2, 1)$ $(1, 1, 1)$	$(0, 0, 3)$ $(1, 0, 2)$ $(2, 0, 1)$	1f , 2p
41 – 70	4	$(4, 0, 0)$ $(1, 3, 0)$ $(3, 1, 0)$ $(1, 1, 2)$ $(2, 2, 0)$	$(0, 4, 0)$ $(0, 1, 3)$ $(0, 3, 1)$ $(1, 2, 1)$ $(2, 0, 2)$	$(0, 0, 4)$ $(1, 0, 3)$ $(3, 0, 1)$ $(2, 1, 1)$ $(0, 2, 2)$	1g , 2d , 3s
71 – 112	5	$(5, 0, 0)$ $(1, 4, 0)$ $(4, 1, 0)$ $(2, 3, 0)$ $(3, 2, 0)$ $(1, 1, 3)$ $(1, 2, 2)$	$(0, 5, 0)$ $(0, 1, 4)$ $(0, 4, 1)$ $(0, 2, 3)$ $(0, 3, 2)$ $(1, 3, 1)$ $(2, 1, 2)$	$(0, 0, 5)$ $(1, 0, 4)$ $(4, 0, 1)$ $(2, 0, 3)$ $(3, 0, 2)$ $(3, 1, 1)$ $(2, 2, 1)$	1h , 2f , 3p

Table 2.4 – Shell model, where N is the number of free electrons in the conduction band of a cluster, namely the number of cluster atoms with one valence electron (e.g. cluster of Ag_N).

Inserting equation 2.39 into equation 2.38, we obtain the energy of cluster as a function of (n_x, n_y, n_z) :

$$\begin{aligned}
 E_N &= h\omega_0 \sum_{i=1}^N \left\{ (n_x^i + n_y^i + 1) \frac{R_0}{R_x} + (n_z^i + \frac{1}{2}) \frac{R_x^2}{R_0^2} \right\} \\
 &= h\omega_0 \sum_{i=1}^N \left\{ (n_x^i + n_y^i + 1) \left[\frac{\sum_{i=1}^N (n_x^i + n_y^i + 1)}{\sum_{i=1}^N (2n_z^i + 1)} \right]^{-\frac{1}{3}} + (n_z^i + \frac{1}{2}) \left[\frac{\sum_{i=1}^N (n_x^i + n_y^i + 1)}{\sum_{i=1}^N (2n_z^i + 1)} \right]^{\frac{2}{3}} \right\}. \quad (2.40)
 \end{aligned}$$

For spheroids, the shape can be expressed in terms of the distortion parameter:

$$\eta \equiv 2 \frac{R_z - R_x}{R_z + R_x} = 2 \frac{2(\sum_{i=1}^N n_z^i) - (\sum_{i=1}^N n_x^i) - (\sum_{i=1}^N n_y^i)}{2(\sum_{i=1}^N n_z^i) + (\sum_{i=1}^N n_x^i) + (\sum_{i=1}^N n_y^i) + 2N} \quad (2.41)$$

All the discussion from equation 2.37 to equation 2.41 are in harmonic case with $U = 0$. Figure 2.11 shows the Clemenger-Nilsson diagram, giving the single-particle energies as a function of η , with $U = 0.04$ of anharmonic distortion. The total electronic energy is the sum of the single-particle energies. We find that the closed-shell clusters, i.e., 2, 8, 20, ..., are spherical ($\eta = 0$) and that open-shell clusters are either oblate or prolate spheroids.

(3) Ellipsoidal Clemenger-Nilsson shell model

Now we extend the Clemenger-Nilsson model by allowing distortion along three axes, allowing the shapes to be either spheres, spheroids, or ellipsoids. Figure 2.12(a) shows the cluster shapes. For example, the atom and dimer are spherical, since only s states are occupied. The tetramer is prolate, since then p_x state is doubly occupied, and the p_x energy is reduced by elongating the cluster in the x direction. The 5- and 6-mer are disk shaped, since now both the p_x and p_y are filled. The 7-mer is the first three-dimensional cluster, since the p_z orbital is singly occupied, followed by the spherical 8-mer with a completely filled $1p$ shell.

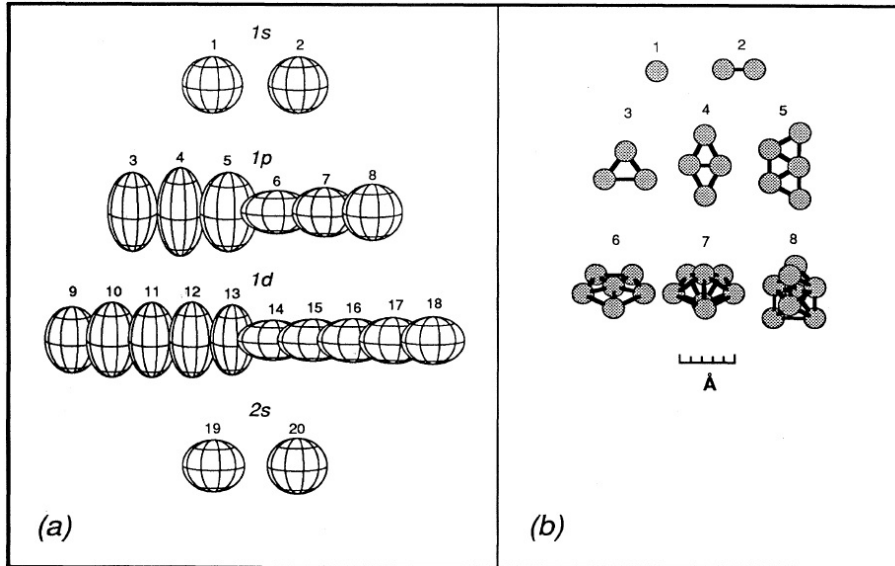


Figure 2.12 – Cluster shapes (a) according to the ellipsoidal shell model, normalized to the constant volume; (b) from ab initio quantum-chemical calculations by Bonacic-Koutecky.

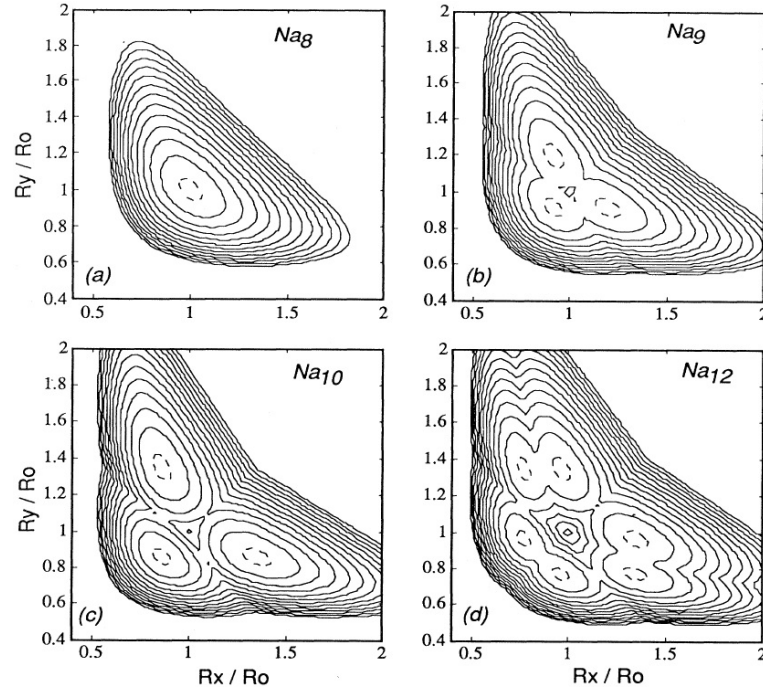


Figure 2.13 – Total-energy surfaces of several sodium clusters as a function of R_x and R_y , calculated in ellipsoidal shell model. Contours are spaced every 0.2eV .

The cluster shapes in the previous subsection were constrained to be spheroidal, i.e., $R_x = R_y$. Removing this constraint allows the clusters to assume ellipsoidal shapes. Therefore the ground-state total-energy surfaces may also be represented simply as functions of R_x and R_y ($R_z = R_0^3/R_x R_y$). But it is trivial to find the equilibrium cluster shapes analytically. Figure 2.13 shows examples (assuming $U = 0$). Here it is evident that Na_8 is spherical (since the lowest energy occurs for $R_x = R_y = R_z = R_0$), Na_9 and Na_{10} are spheroidal, and Na_{12} ellipsoidal.

(4) Polarizability by cluster shape

The normalized polarizability of a spherical cluster can be calculated from equation 2.13 as [71]:

$$\alpha_n = \frac{\alpha}{\epsilon_0 V} = 3 \frac{\epsilon_r - 1}{\epsilon_r + 2}, \quad (2.42)$$

where $\epsilon_r = \epsilon/\epsilon_0$ is the relative permittivity of the sphere.

Chapter 2. Theory

Now for a ellipsoidal cluster, the polarizability can be calculated as:

$$\alpha_{n,ave} = \frac{1}{3}(\alpha_x + \alpha_y + \alpha_z), \quad (2.43)$$

where:

$$\begin{aligned} \alpha_x &= \frac{\epsilon_r - 1}{1 + N_x(\epsilon_r - 1)}, \\ \alpha_y &= \frac{\epsilon_r - 1}{1 + N_y(\epsilon_r - 1)}, \\ \alpha_z &= \frac{\epsilon_r - 1}{1 + N_z(\epsilon_r - 1)}, \end{aligned} \quad (2.44)$$

with:

$$\begin{aligned} N_x &= \frac{R_x R_y R_z}{2} \int_0^\infty \frac{ds}{(s + R_x^2) \sqrt{(s + R_x^2)(s + R_y^2)(s + R_z^2)}}, \\ N_y &= \frac{R_x R_y R_z}{2} \int_0^\infty \frac{ds}{(s + R_y^2) \sqrt{(s + R_x^2)(s + R_y^2)(s + R_z^2)}}, \\ N_z &= \frac{R_x R_y R_z}{2} \int_0^\infty \frac{ds}{(s + R_z^2) \sqrt{(s + R_x^2)(s + R_y^2)(s + R_z^2)}}, \end{aligned} \quad (2.45)$$

where $N_x + N_y + N_z = 1$.

For a spheroidal cluster ($R_x = R_y$ and $R_x R_y R_z = R_0^3$), we have the shape of cluster defined by the distortion parameter of η according to equation 2.41:

$$\begin{aligned} R_x &= \left(\frac{2 - \eta}{2 + \eta} \right)^{\frac{1}{3}} R_0, \\ R_y &= \left(\frac{2 - \eta}{2 + \eta} \right)^{\frac{1}{3}} R_0, \\ R_z &= \left(\frac{2 + \eta}{2 - \eta} \right)^{\frac{2}{3}} R_0. \end{aligned} \quad (2.46)$$

So equation 2.45 can be written as:

$$\begin{aligned}
 N_x &= \frac{1}{2} \int_0^\infty \frac{ds'}{\left[s' + \left(\frac{2-\eta}{2+\eta} \right)^{\frac{2}{3}} \right]^2 \left[s' + \left(\frac{2+\eta}{2-\eta} \right)^{\frac{4}{3}} \right]^{\frac{1}{2}}}, \\
 N_y &= \frac{1}{2} \int_0^\infty \frac{ds'}{\left[s' + \left(\frac{2-\eta}{2+\eta} \right)^{\frac{2}{3}} \right]^2 \left[s' + \left(\frac{2+\eta}{2-\eta} \right)^{\frac{4}{3}} \right]^{\frac{1}{2}}}, \\
 N_z &= \frac{1}{2} \int_0^\infty \frac{ds'}{\left[s' + \left(\frac{2-\eta}{2+\eta} \right)^{\frac{2}{3}} \right] \left[s' + \left(\frac{2+\eta}{2-\eta} \right)^{\frac{4}{3}} \right]^{\frac{3}{2}}}.
 \end{aligned} \tag{2.47}$$

With equation 2.43, 2.44 and 2.47, we have the polarizability $\alpha_{n,ave}$ of cluster as a function of shape η .

2.3.4 Hydrodynamic model of a metal sphere

(1) Classical local Drude model

The simplest approach is the classical local-response Drude model with a homogeneous electron density profile in the metal, assuming a constant free-electron density n_0 in the metal particle, which drops abruptly to zero outside the particle.

Neglecting the extrinsic retardation effect and combining equations 2.3 with 2.9, we can rewrite the classical quasistatic Drude permittivity as:

$$\varepsilon_D(\omega) = \varepsilon_\infty(\omega) - \frac{\omega_p^2}{\omega^2 + i\Gamma\omega}, \tag{2.48}$$

by taking interband transitions into account through $\varepsilon_\infty(\omega) = 1 + \chi^{IB}(\omega)$.

If the metal sphere is embedded in a homogeneous background dielectric media with permittivity ε_m , the classical local-response polarizability α_L can be written as (see equation 2.13 and equation 2.42):

$$\alpha_L(\omega) = 4\pi R^3 \frac{\varepsilon_D(\omega) - \varepsilon_m}{\varepsilon_D(\omega) + 2\varepsilon_m}, \tag{2.49}$$

where R is the radius of the particle. As we have already discussed before in Section 2.2.2, the resonance condition is $\varepsilon_D(\omega) = -2\varepsilon_m$ which makes $\alpha_L(\omega)$ maximum.

(2) Semiclassical local Drude model

A more complicated approach is the semiclassical local-response Drude model, where the electron density is determined from the quantum mechanical problem of electrons moving in an infinite spherical potential well [72]. In this approach, the standard approximation in local-response theory of a homogenous electron density profile is corrected by using insight from the quantum wave nature of electrons to model the electron density profile and take into account the quantum confinement of the electrons, thus taking into account an inhomogeneous electron density.

Therefore, equation 2.49 can be extended as:

$$\alpha_{LQC}(\omega) = 12\pi \int_0^R r^2 dr \frac{\varepsilon(r, \omega) - \varepsilon_m}{\varepsilon(r, \omega) + 2\varepsilon_m}, \quad (2.50)$$

with a spatially varying Drude permittivity:

$$\varepsilon(r, \omega) = \varepsilon_\infty(\omega) - \frac{\omega_p^2}{\omega^2 + i\Gamma\omega} \frac{n(r)}{n_0}. \quad (2.51)$$

Here $n(r)$ is the electron density in the metal nanoparticle. Clearly, if $n(r) = n_0$ we arrive at the classical model of equation 2.49 as expected.

(3) Semiclassical nonlocal hydrodynamic model

The final approach is the semiclassical nonlocal hydrodynamic description of the electron density which takes into account nonlocal response through the internal quantum kinetics of the electron gas in the Thomas-Fermi (TF) approximation [72]. In this approach, the electron density is allowed to deviate slightly from the constant electron density used in classical local-response theories. The dynamics of the electron gas is governed by the semiclassical hydrodynamic equation of motion, which also results in an inhomogeneous electron density profile.

The nonlocal hydrodynamic polarizability is given as:

$$\alpha_{NL}(\omega) = 4\pi R^3 \frac{\varepsilon_D(\omega) - \varepsilon_m(1 + \delta_{NL})}{\varepsilon_D(\omega) + 2\varepsilon_m(1 + \delta_{NL})}, \quad (2.52)$$

with

$$\delta_{NL} = \frac{\varepsilon_D(\omega) - \varepsilon_\infty(\omega)}{\varepsilon_\infty(\omega)} \frac{j_1(k_L R)}{k_L R j_1'(k_L R)}. \quad (2.53)$$

Here $k_L = \sqrt{\omega^2 + i\Gamma\omega - \omega_p^2/\varepsilon_\infty}/\beta$ is the wave vector of the additional longitudinal wave allowed to be excited in the hydrodynamic nonlocal theory, and j_1 is the spherical Bessel function of first order. Finally, within TF theory $\beta = 3/5 v_F^2$, where v_F is the Fermi velocity. Note that for $\beta \rightarrow 0$, the local-response Drude result is retrieved, since $\delta_{NL} \rightarrow 0$ and equation 2.52 simplifies to the classical model of equation 2.49 as expected as well.

Therefore, the resonance frequency can be approximated by using equation 2.16 as:

$$\omega = \frac{\omega_p}{\sqrt{\text{Re}[\varepsilon_\infty(\omega)] + 2\varepsilon_m}} + \sqrt{\frac{2\varepsilon_m}{\text{Re}[\varepsilon_\infty(\omega)]}} \frac{\beta}{2R} + O\left(\frac{1}{R^2}\right), \quad (2.54)$$

where the first term is the common size-dependent local-response Drude result for the SP resonance (see equation 2.17) that also follows equation 2.49, and the second term gives the size-dependent blueshift due to nonlocal corrections.

2.3.5 Time dependent density functional theory (TDDFT)

Recent progress in theory, in particular TDDFT, allows to extend the size range for the investigation of optical properties up to more than 100 atoms for the simplest transition metals [73].

TDDFT can be viewed as an exact reformulation of time-dependent quantum mechanics, where the fundamental variable is no longer the many-body wave function but the density [74]. This time-dependent density is determined by solving an auxiliary set of noninteracting Schrödinger equations, the Kohn-Sham equations. The nontrivial part of the many-body interaction is contained in the so-called exchange-correlation potential, for which reasonably good approximations exist. Within TDDFT two regimes can be distinguished: (a) If the external time-dependent potential is “small,” the complete numerical solution of the time-dependent Kohn-Sham equations can be avoided by the use of linear response theory. This is the case, e.g., for the calculation of photoabsorption spectra. (b) For a “strong” external potential, a full solution of the time-dependent Kohn-Sham equations is in order. This situation is encountered, for instance, when matter interacts with intense laser fields.

It was in 1964 that Hohenberg and Kohn [75] discovered that to fully describe a stationary electronic system it is sufficient to know its ground-state density. From this quantity all ob-

servables (and even the many-body wave function) can, in principle, be obtained. The density is a very convenient variable: it is a physical observable, it has an intuitive interpretation, and it depends only on three spatial coordinates, in contrast to the many-body wave function, which is a complex function of $3N$ spatial coordinates. Hohenberg and Kohn also established a variational principle in terms of the density by showing that the total energy can be written as a density functional whose minimum, the exact ground-state energy of the system, is attained at the exact density. In this way, they put on a sound mathematical basis earlier work by Thomas [76], Fermi [77], and others, who had tried to write the total energy of an interacting electron system as an explicit functional of the density.

Another breakthrough occurred when Kohn and Sham [78] proposed the use of an auxiliary noninteracting system, the Kohn-Sham system, to evaluate the density of the interacting system. Within the Kohn-Sham system, the electrons obey a simple, one-particle, Schrödinger equation with an effective external potential, v_{KS} . As v_{KS} is a functional of the electronic density, the solution of this equation has to be performed self-consistently. The effective potential, v_{KS} , is usually decomposed in the form:

$$v_{KS}(\vec{r}) = v_{ext}(\vec{r}) + v_{Hartree}(\vec{r}) + v_{XC}(\vec{r}). \quad (2.55)$$

The first term is the external potential (normally the Coulomb interaction between the electrons and the nuclei), whereas the second includes the classical (Hartree) part of the electron-electron interaction. All the complex many-body effects are contained in the (unknown) exchange-correlation (xc) potential v_{XC} . Kohn and Sham [78] also proposed a simple approximation to v_{XC} , the local density approximation (LDA). This functional, that uses the knowledge of the XC energy of the homogeneous electron gas [79], turned out to be quite accurate for a number of applications, and is still widely used, especially in solid-state physics.

The use of the density as the fundamental variable, and the construction of the Kohn-Sham system form the basis of what became known as density functional theory (DFT). The original formulation assumed an electronic system at zero temperature with a nondegenerate ground state, but has been extended over the years to encompass systems at finite temperature, superconductors, relativity, etc. An extension of somewhat different nature is time dependent DFT (TDDFT) [80]. The foundation of modern TDDFT was laid in 1984 by Runge and Gross [81], who derived a Hohenberg-Kohn-like theorem for the time-dependent Schrödinger equation. The scope of this generalization of DFT included the calculation of photoabsorption spectra or, more generally, the interaction of electromagnetic fields with matter, as well as the time-dependent description of scattering experiments (which was actually the original motivation of Runge and Gross). Again, the rigorous theorems of Runge and Gross put on a firm basis previous work by Ando and by Zangwill and Soven [82], who had performed the first time-dependent Kohn-Sham calculations.

The (nonrelativistic) many-body Schrödinger equation can be described as:

$$i\frac{\partial}{\partial t}\Psi(\{\vec{r}\}, t) = \hat{H}(\{\vec{r}\}, t)\Psi(\{\vec{r}\}, t), \quad (2.56)$$

where \hat{H} is the Hamilton operator of the system and $\{\vec{r}\} = \{\vec{r}_1, \dots, \vec{r}_N\}$ are the spatial coordinates of the N electrons. This equation describes an initial value problem, i.e., if we know the state of the system at an initial time t_0 , equation 2.56 allows us to calculate Ψ at any other time t . This is quite different from the solution of the time-independent Schrödinger equation, where our aim is to find the eigenstates of the Hamiltonian subject to some appropriate boundary conditions.

The Hamiltonian is naturally decomposed into three parts:

$$\hat{H}(\{\vec{r}\}, t) = \hat{T}(\{\vec{r}\}) + \hat{W}(\{\vec{r}\}) + \hat{V}_{ext}(\{\vec{r}\}, t). \quad (2.57)$$

The first two are the kinetic energy and the electron-electron interaction:

$$\hat{T}(\{\vec{r}\}) = -\frac{1}{2} \sum_{i=1}^N \nabla_i^2, \quad \hat{W}(\{\vec{r}\}) = \frac{1}{2} \sum_{i,j=1(i \neq j)}^N \frac{1}{|\vec{r}_i - \vec{r}_j|}. \quad (2.58)$$

The third term can be written as a sum of one-body potentials:

$$\hat{V}_{ext}(\{\vec{r}\}, t) = \sum_{i=1}^N v_{ext}(\vec{r}_i, t), \quad (2.59)$$

and can be used, for example, to describe the Coulomb interaction of the electrons with a set of nuclei:

$$v_{ext}(\vec{r}, t) = - \sum_{v=1}^{N_n} \frac{Z_v}{|\vec{r} - \vec{R}_v(t)|}, \quad (2.60)$$

where Z_v and \vec{R}_v denote the charge and position of the nucleus v , and N_n stands for the total number of nuclei in the system. Note that by allowing the \vec{R}_v to depend on time we can treat

situations where the nuclei move along a classical path. This may be useful to study, e.g., scattering experiments and chemical reactions. Another very interesting class of problems is the interaction of electrons with external time dependent fields. For example, for a system illuminated by a laser beam we can write, in the dipole approximation,

$$v_{ext}(\vec{r}, t) = Ef(t) \sin(\omega t) \vec{r} \cdot \alpha, \quad (2.61)$$

where α , ω , and E are the polarization, the frequency, and the amplitude of the laser, respectively. The function $f(t)$ is an envelope that describes the temporal shape of the laser pulse.

The absolute square of the wave function $\Psi(\{\vec{r}\}, t)$ is interpreted as the probability of finding at time t one electron at \vec{r}_1 , another at \vec{r}_2 , etc. It then follows that:

$$n(\vec{r}, t) = N \int d^3\vec{r}_2 \dots d^3\vec{r}_N |\Psi(\vec{r}, \vec{r}_2 \dots \vec{r}_N, t)|^2, \quad (2.62)$$

gives N times the probability of finding an electron at time t and position \vec{r} . With this definition, the density $n(\vec{r}, t)$ is normalized at all times to the total number of electrons, N . This quantity, the electronic density $n(\vec{r}, t)$, is the basic variable in terms of which TDDFT is formulated.

The central theorem of TDDFT (now called the Runge-Gross theorem) proves that there is a one-to-one correspondence between the external (time-dependent) potential, $v_{ext}(\vec{r}, t)$, and the electronic density, $n(\vec{r}, t)$, for many-body systems evolving from a fixed initial state. This is a nontrivial statement with profound consequences. It implies that, if the only information we have about the system is its density, we can obtain the external potential that produced this density. With the external potential the time-dependent Schrödinger equation can be solved, and all properties of the system obtained. From this we conclude that the electronic density determines all other properties of the quantum system. Note that this statement is true for a fixed initial state, i.e, besides the knowledge of $n(\vec{r}, t)$ we also need to know the initial many-body state. The situation is somewhat different if the system departs from its ground state: By virtue of the ordinary Hohenberg-Kohn theorem, the many-body ground state is uniquely determined by the initial density, $n(\vec{r}, t = t_0)$. If, however, the system at $t = t_0$ is in an arbitrary state, the knowledge of the initial state is essential.

In possession of the Runge-Gross theorem, it is fairly straightforward to construct a time-dependent Kohn-Sham scheme. We introduce an auxiliary system of noninteracting electrons subject to an external local potential v_{KS} . This potential is unique, by virtue of the Runge-Gross theorem applied to the noninteracting system, and is chosen such that the density of

the Kohn-Sham electrons is the same as the density of the original interacting system. These Kohn-Sham electrons obey the time-dependent Schrödinger equation:

$$i\frac{\partial}{\partial t}\varphi_i(\vec{r}, t) = \hat{H}_{KS}(\vec{r}, t)\varphi_i(\vec{r}, t), \quad (2.63)$$

where the Kohn-Sham Hamiltonian is defined as:

$$\hat{H}_{KS}(\vec{r}, t) = -\frac{\nabla^2}{2} + v_{KS}[n](\vec{r}, t), \quad (2.64)$$

By construction, the density of the interacting system can then be calculated from the Kohn-Sham orbitals:

$$n(\vec{r}, t) = \sum_i^N |\varphi_i(\vec{r}, t)|^2. \quad (2.65)$$

As in the Kohn-Sham scheme for the ground state, the time-dependent Kohn-Sham potential is normally written as the sum of three terms:

$$v_{KS}[n](\vec{r}, t) = v_{ext}(\vec{r}, t) + v_{Hartree}[n](\vec{r}, t) + v_{XC}[n](\vec{r}, t). \quad (2.66)$$

The first term is the external potential, whereas the second accounts for the classical electrostatic interaction between the electrons:

$$v_{Hartree}(\vec{r}, t) = \int d^3\vec{r}' \frac{n(\vec{r}', t)}{|\vec{r} - \vec{r}'|}. \quad (2.67)$$

The third term, the xc potential, includes all nontrivial many-body effects, and has an extremely complex (and essentially unknown) functional dependence on the density. This dependence is clearly nonlocal, both in space and in time, i.e., the potential at time t and position \vec{r} can depend on the density at all other positions and all previous times (due to causality). Note that the way of writing is largely a matter of convention. We separate out of v_{KS} two large terms that are well known, the external and Hartree potentials, and write the rest as the “mysterious” xc term that we expect to approximate using clever physical and mathematical arguments.

The quality of the results obviously depends on the quality of the approximation to the xc potential used. It is important to stress that, like in ground-state density functional theory, this is the only fundamental approximation in TDDFT.

Formally, not only is v_{KS} a functional of the density, but it also depends on the initial Kohn-Sham determinant and on the initial many-body wave function. For practical reasons the latter dependence is always neglected. Explicit density functionals, like the adiabatic LDA, only retain the density dependence. Orbital functionals, on the other hand, are functionals of both the time-dependent density and the initial Kohn-Sham determinant.

At the heart of the Kohn-Sham construction lies the assumption that there exists a noninteracting system that possesses the same density as the interacting system that we are interested in. If this is the case, the interacting density is said to be noninteracting v -representable. For ground-state DFT it is well known that there are some smooth densities that are not noninteracting v -representable by a single determinant. Curiously, the situation is much more satisfactory in TDDFT: it was shown that, under very mild assumptions, a time-dependent one-body potential $v_{KS}(\vec{r}, t)$ exists that reproduces a given smooth density $n(\vec{r}, t)$ at all times.

2.3.6 Intrinsic size effect

As discussed before, the change of optical response with cluster size can be described either by extrinsic effect or by intrinsic effect. The former is caused by the retarding effect due to the comparable size of cluster to light wavelength. The colorful stained glass of cathedral window is a good example. But although the absorption wavelength of stained glass changes with the size of clusters embedded inside, the intrinsic dielectric function of the clusters stay the same value as that of the bulk material. By contrast, the latter is caused by the change of dielectric function with cluster size due to the limited volume and high surface to volume ratio. Figure 2.14 gives the examples of some experimental results of intrinsic effect compared with theoretical TDDFT calculations in very small silver clusters (Ag_1 - Ag_9).

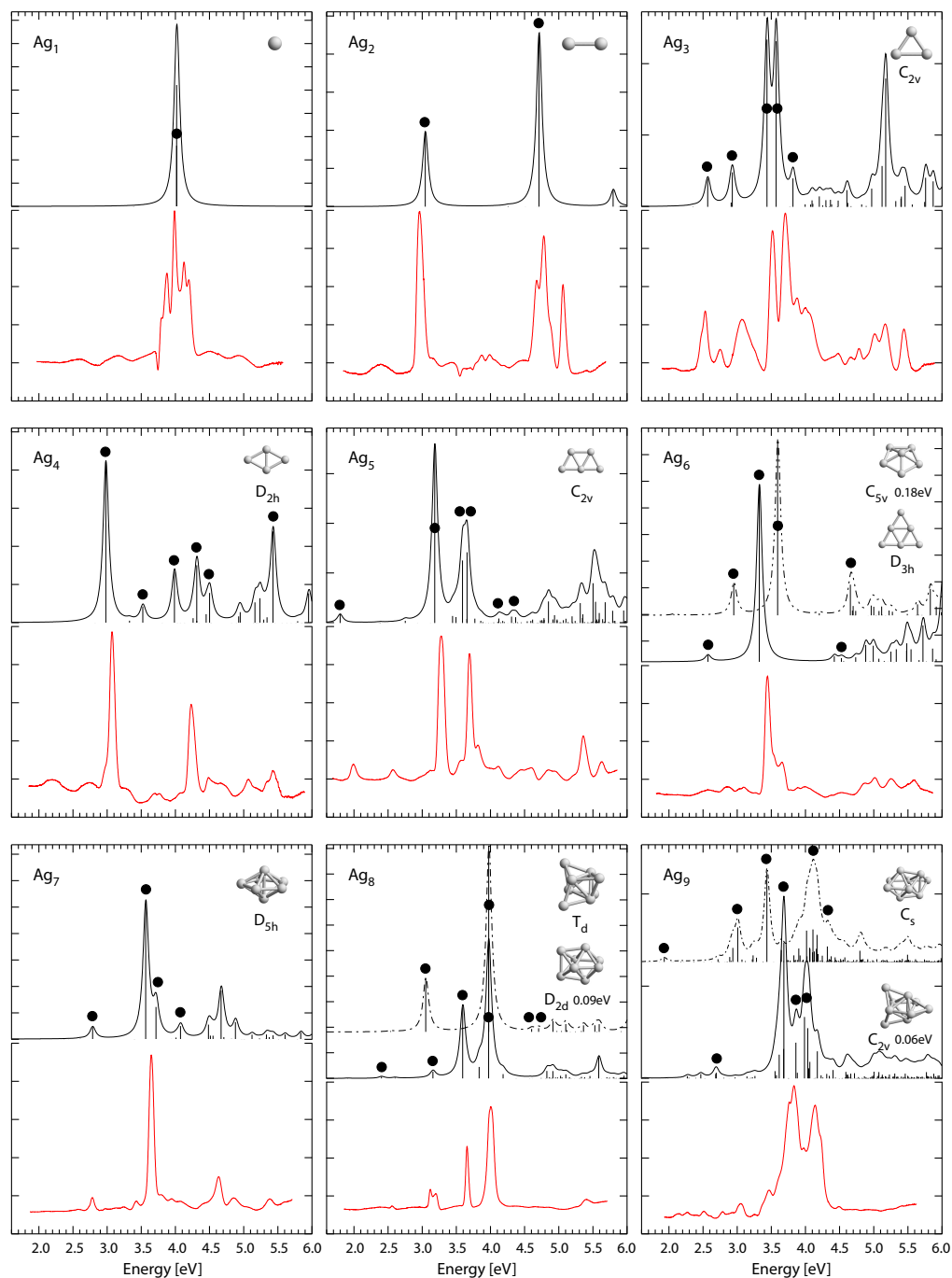


Figure 2.14 – Comparison between experimental and calculated absorption spectra of silver clusters. Experimental absorption for Ag_n ($n = 1 - 9$) – bottom curve. TD-DFT calculations for the best fitting isomer – continuous line – and energetically closest isomer – interrupted line. The black dots identify transitions whose initial state is predominantly of s-type. [51]

2.4 Surface enhanced Raman scattering (SERS)

SERS is currently the only method that can simultaneously detect a single molecule and provide its chemical fingerprint [67, 58]. SERS refers to the strong enhancement by factors as large as $10^6 - 10^{12}$ of the Raman signal of molecules in close proximity to nanostructures that exhibit plasmons [67]. However, even 35 years after its initial discovery, it is still not completely understood due to its highly complex nature and required experimental conditions. Most early theories of SERS focused on simple classical models, such as a dipole model where the adsorbate is approximated by a single dipole over a smooth surface with no chemical interaction between the two [83].

Recently, resulting from the experimental observations, two main methods of explaining the larger enhancements of SERS arose, one being an electromagnetic mechanism (EM) and the other being a chemical mechanism (CM). In its most general terms, CM arises from overlap between the metal and adsorbate wave functions, whereas EM is classical in nature and does not rely on this overlap.

Today, it is well accepted that EM arises due to resonances between the incident laser and the surface plasmons of the metallic nanostructured surface. EM typically is the largest contributor to SERS, yielding enhancements anywhere between 10^4 and 10^8 [67].

In contrast to EM, the nature of CM enhancement is less clear. It is generally accepted that there is a dynamic charge-transfer (CT) mechanism that arises from a resonance between the incident laser and a metal to molecule or molecule to metal excitation. Additionally, if the incident laser is resonant with an intermolecular excitation, the molecule will experience resonance Raman scattering (RRS). Although this is strictly not a surface effect, the metal does influence the RRS enhancement. CT and RRS have individually been known to contribute enhancements anywhere from 10 to 10^6 . Finally, there is a small enhancement that is gained simply by placing the molecule onto a metal surface, which is due to relaxation of the electronic structure of the molecule; this is called the nonresonant chemical mechanism (CHEM) and is expected to only yield enhancements on the order of 10^2 or less.

Of course, the two mechanisms EM and CM are not mutually exclusive but work together in concert to produce the overall SERS effect. However, depending on the specific system, the importance of individual mechanisms may vary. Figure 2.15 illustrates the different enhancement mechanisms.

2.4.1 The electromagnetic mechanism (EM)

EM is a result of surface plasmon resonances on the nanoparticle surface and is therefore considered to be independent of the nature of the molecule or the chemical bond between

2.4. Surface enhanced Raman scattering (SERS)

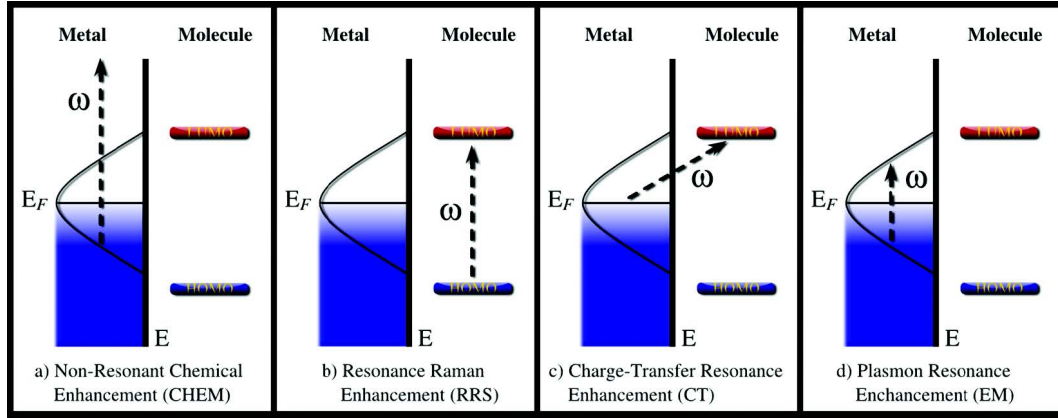


Figure 2.15 – Diagram of the mechanism of SERS, which includes EM and CM=RRS+CT+CHEM. (EM=electromagnetic mechanism; CM=chemical mechanism; RRS=resonance Raman scattering; CT=dynamic charge transfer; CHEM=nonresonant chemical mechanism). [67]

the metal and molecule. The enhancement factor due to EM can be written as:

$$EF_{EM} = |\vec{E}(\omega)|^2 |\vec{E}(\omega')|^2, \quad (2.68)$$

where EF_{EM} is the electromagnetic mechanism enhancement factor, $\vec{E}(\omega)$ is the frequency-dependent electric field at incident frequency ω , and $\vec{E}(\omega')$ is the frequency-dependent electric field at the Stokes shifted frequency ω' . However, since the Stokes shift is usually small compared with the wavelength of laser, equation 2.68 is typically simplified as:

$$EF_{EM} = |\vec{E}(\omega)|^4. \quad (2.69)$$

The local electromagnetic field due to plasmon excitations is largest in regions with high local curvature and in particular in the junction between dimers of nanoparticles, the so-called hot spots. An intriguing phenomenon related to EM is that the location of the maximum EF_{EM} does not coincide with the plasmon resonance peak ω , but rather is slightly blue-shifted. A simple explanation of this can be achieved by considering equation 2.68. Since EF_{EM} is dependent on both ω and ω' , the maximum EF_{EM} should occur halfway between these two values. This is indeed what is observed, which calls into question the validity of the $\omega \approx \omega'$ approximation that is generally assumed.

2.4.2 The chemical mechanism (EM)

SERS was shown to exist for nonplasmonic metals³⁴⁹ or flat surfaces where EM effects are not expected to be important. These observations pointed toward the existence of a chemical mechanism (CM). CM is also sometimes referred to as the electronic mechanism or first layer effect due to its short-range nature.

The chemical mechanism can be divided into three contributions:

- (1) A molecular resonance (RRS) mechanism. This is analogous to RRS for a free molecule except that the presence of the surface modifies the enhancements observed. This is not traditionally included as a chemical mechanism, but since it is in fact altered by the metal, we prefer to include it as a chemical mechanism. RRS is typically expected to contribute enhancements of $10^3 - 10^6$.
- (2) A charge transfer (CT) mechanism, in which the applied field is in resonance with either a metal molecule or molecule-metal transition and typically provides enhancements around $10 - 10^4$. It has been proposed that it may be as large as 10^7 in some situations, based on recent experimental work.
- (3) A nonresonant chemical (CHEM) mechanism, which arises simply from the ground-state interaction of the molecule with the metal. This is the weakest of the mechanisms, only leading to enhancements on the order of $10 - 100$.

2.4.3 Unifying EM and CM

Previous subsections focused on one of the main mechanisms of SERS. However, because the different mechanisms occur in concert, it is important to establish a model that describes their combined effect. Lombardi and Burke [84, 85] have recently developed a unified expression to explain many of the observations that are seen in SERS. This unified theory for SERS models EM, CT, and RRS simultaneously, and is written as:

$$R_k(\omega) = \frac{S_k}{((\epsilon_1(\omega) + 2\epsilon_0)^2 + \epsilon_2(\omega)^2) ((\omega_{CT}^2 - \omega^2) + \Gamma_{CT}^2) ((\omega_{RRS}^2 - \omega^2) + \Gamma_{RRS}^2)}. \quad (2.70)$$

Here $\epsilon_1(\omega)$ and $\epsilon_2(\omega)$ are the real and imaginary dielectric components of the metal, ϵ_0 is the permittivity of free space, ω is the incident laser frequency, and ω_{CT} , ω_{RRS} , Γ_{CT} and Γ_{RRS} are the CT and RRS excitation energies and excited state relaxation rates, respectively. The enhancement factor for a specific mode is then given by $EF_k(\omega) = |R_k(\omega)|^2$. The term S_k represents selection rules for the given vibrational mode k based on transition dipole moments and Herzberg-Teller coupling [86]. The denominator represents the different resonance conditions for the different enhancement mechanisms, where the first term is EM ($\epsilon_1(\omega) =$

2.4. Surface enhanced Raman scattering (SERS)

$-2\varepsilon_0$), the middle term is CT ($\omega_{CT} = \omega$), and the last term is RRS ($\omega_{RRS} = \omega$).

The expression of equation 2.70 illustrates that the different mechanisms are not isolated, because the three terms are multiplicative rather than additive.

3 Experiment

This Chapter focuses on the experimental setup developed during this thesis work that are designed for the fabrication, size selection and deposition of small metal clusters and metal-organic compounds as well as the optical measurements of absorption, fluorescence, excitation and Raman scattering in the UV-visible range.

3.1 Overview of apparatus

The experimental setup is designed and built to fabricate, size-select and deposit small metal clusters in a solid rare-gas matrix. Figure 3.1 shows a 2D drawing and 3D model of the apparatus which is composed of 4 vacuum chambers (source chamber, differential chamber, deflection chamber and deposition chamber) containing 3 main sections (cluster source, ion guide and deposition head). Clusters are produced from the cluster source, then guided and size-selected by the ion guide, and finally soft-landed and co-deposited with rare gas on the deposition head.

3.2 Vacuum system

The source chamber is pumped by two turbo-pumps $2 \times (1300 \text{ L/s})$ backed by a roots pump (70 L/s) to pump the large gas load of about 100 sccm. The differential chamber is separated into two chambers pumped by two turbo-pumps (500 L/s) each. The deflection chamber is pumped by one turbo-pump (260 L/s) to further reduce the pressure. Finally the deposition chamber is pumped by one turbo-pump (140 L/s) and one cyro-pump (50 K) to condense the contaminants like H_2O on its cold surfaces [87]. A residual gas analyzer is installed in the deposition chamber to inspect the vacuum and the purity of the matrix. Without the cluster source running, the background pressure in the chambers is about 10^{-8} mbar uniformly. When the cluster source is on with the input of He and Ar gas, the pressure in the source chamber is about 10^{-3} mbar with a typical gas load of 10^{-1} mbar in aggregation tube. Thanks to the differential chamber as shown in table 3.1, the pressure of residual gas in the deposition

Chapter 3. Experiment

chamber is finally reduced to 10^{-7} mbar which is only about 1% of the pressure of 10^{-5} mbar of Ne gas load for the matrix formation, ensuring a high matrix purity of about 99%.

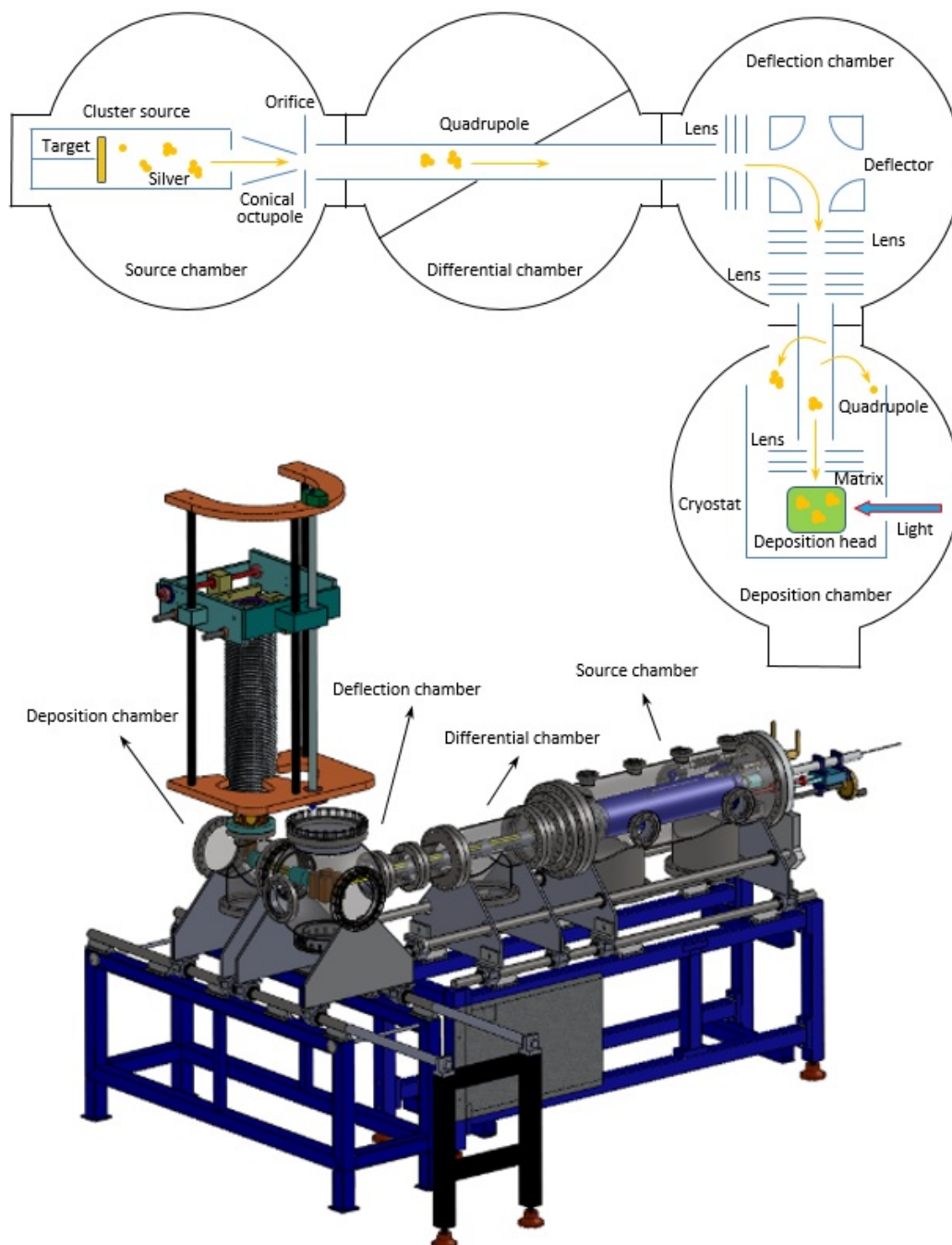


Figure 3.1 – Sketch of the experimental setup for fabrication, mass-selection and deposition of small metal clusters embedded in rare gas solid matrix. Here the inset shows the 3D model of the machine.

3.3 Gas aggregation cluster source

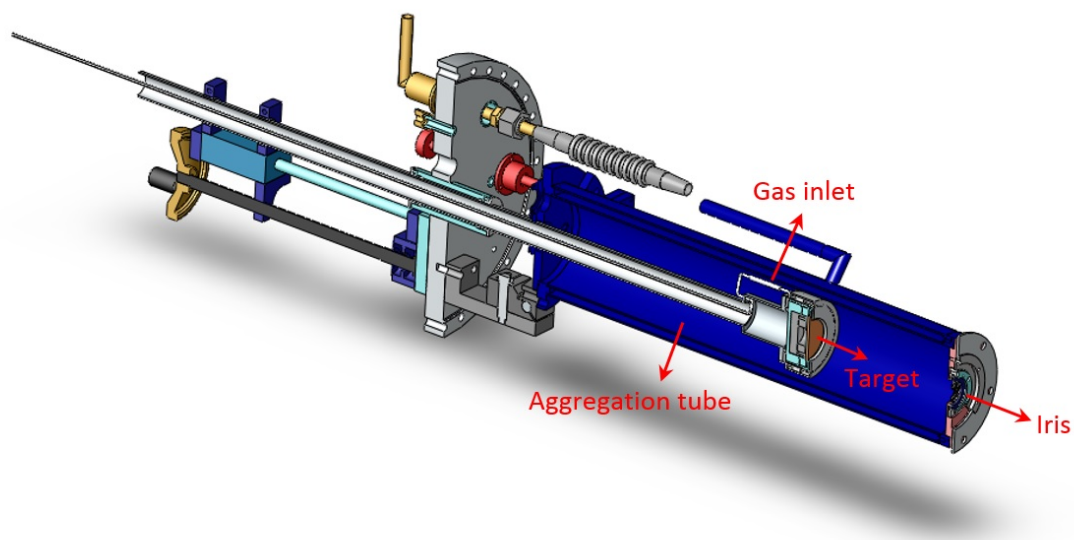


Figure 3.2 – 3D model of the gas aggregation cluster source.

3.3.1 Source setup

Clusters are produced in a combined sputter gas aggregation source given from Freiburg University [88, 89]. As shown in figure 3.2, the cluster source is composed of 4 main parts: metal target with magnetron sputtering head, gas inlet, aggregation tube, and iris.

An oblate metal target with 50.8 mm (2 inches) of diameter and 5 mm of thickness is placed on the magnetron head which is covered by a metal cap in front and connected by two water tubes behind. The cap has numerous millimeter-size pores, linking to the gas tubes, around its periphery towards the magnetron head in order to provide the He and Ar gas. The water tubes are used to cool down the magnetron head when the source is running. Two liquid nitrogen tubes are connected to the aggregation tube, serving to cool down the environment inside the aggregation tube. The position of the magnetron head inside the aggregation tube can be

Source	Matrix	Pressure (mbar)				
		Aggreg. tube	Sour. chamber	Dif. chamber	Def. chamber	Dep. chamber
OFF	OFF	10^{-8}	10^{-8}	10^{-8}	10^{-8}	10^{-8}
ON	OFF	10^{-1}	10^{-3}	10^{-4}	10^{-6}	10^{-7}
ON	ON	10^{-1}	10^{-3}	10^{-4}	10^{-6}	10^{-5}

Table 3.1 – Differential pressures in vacuum chambers of the experimental setup in different conditions.

changed by a spiral hand on the base.

There are two main process of the fabrication of clusters from the source: firstly the sputtering process that provides atoms, and secondly the aggregation process that forms the clusters.

3.3.2 Sputtering process

When the source is running, a constant discharge power of about tens of watts with a typical discharge voltage of hundreds of volts is provided between the magnetron head and the cap that connects to the ground, where the magnetron head serves as the anode and the cap serves as the cathode. Argon and Helium gases are co-injected from the gas inlet towards the magnetron head, the flux of which is controlled by a MKS mass flow controller. The argon atoms then get ionized and hit on the metal target with kinetic energy of about 0 – 100 eV, making the sputtering. The neutral metal atoms and charged metal ions then come out from the target. At this energy range, only atoms (not clusters) are produced from the metal target during the sputtering process.

3.3.3 Aggregation process

The hot metal ions then drift from the target toward the iris window inside the aggregation tube due to the electric field. The He atoms then collide with the metal atoms during the drift inside the aggregation tube. The collisions aggregate the metal ions together, the size of which grows with the process of drift. At the same time during the drift, the metal ions also reduce the heat and become cooler due to the collision, which transforms the metal vapor to metal cluster.

3.3.4 Characteristic of source

Compared with the conventional sputtering source, the biggest advantage of this aggregation source is its continuous and tunable size of clusters (normally from 1 to 10^4 atoms). The shape of the distribution of cluster size is very sensitive to the parameters of aggregation source: aggregation length (defined as the distance between the magnetron head and the iris, typically 10 cm), discharge power (typically 20 W), flux of Ar (typically 100 sccm) and flux of He (typically 200 sccm).

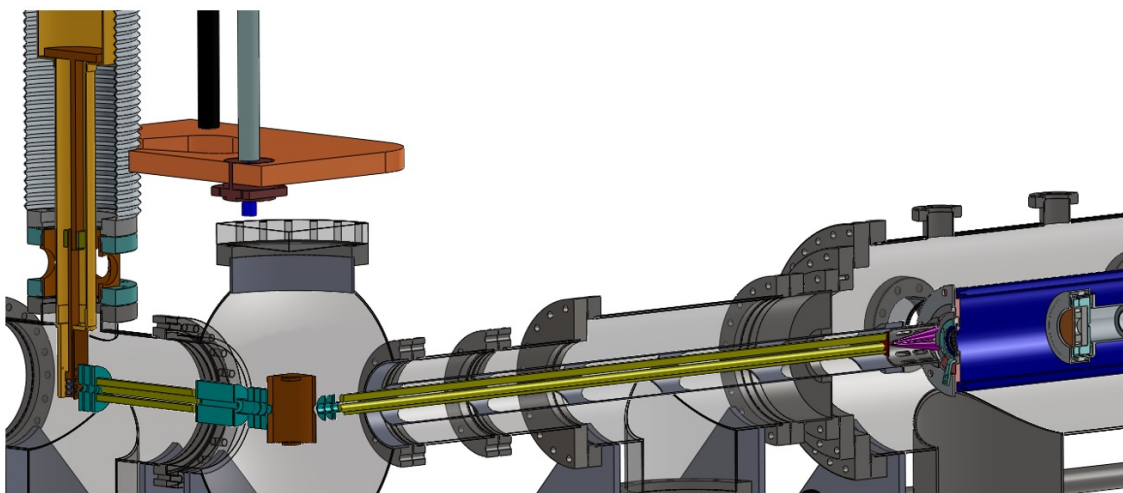


Figure 3.3 – 3D model of experimental setup which includes the cluster source (right part), the ion guide device (center part) and the deposition head (left part). Here the inset shows the whole view of the setup.

3.4 Ion guide device

One of the core parts of the machine is the ion guide device who transports and mass-selects the metal clusters. As shown in figure 3.3, this device includes a conical octupole, two quadrupoles, four electrostatic lenses and a deflector. Cluster ions coming out from the iris window of the cluster source are first focused by the conical octupole, then guided (or mass-selected) by the first long quadrupole, focused by the first lens, bended by the deflector, focused by the second and third lens, mass-selected (or guided) by the second short quadrupole, focused by the fourth lens, and finally soft-landed toward the deposition head.

3.4.1 Conical octupole

The custom-made conical octupole was designed following the concept of Röttgen et al. [90]. Its realization is shown in figure 3.4. The conical octupole is composed of two ceramic plates (grey part), eight identical conical metal rods (pink part) and an orifice (brown part), the whole of which is mounted in a cylindrical tube (transparent part in figure 3.4(f)). The eight conical rods are separated into two groups, each of which contains four rods, that are fixed on two electrical isolated ceramic plates forming two conical quadrupoles (as shown in figure 3.4(d)-(e)) in order to avoid short-circuit of the electrodes caused by the metallization of the ceramic due to the metal vapor transported by the rare gas. The two conical quadrupoles are provided with high frequency (≈ 1 MHz) AC voltage (≈ 1 kV) with opposite sign. In this way, the cluster ions can be well confined in the octupole due to the high frequency AC voltage, and focused toward the orifice due to the conical shape. Note that the octupole is the first ion guide piece after the cluster source, where a large collision of clusters exist inevitably. So the conical

octupole is an essential and irreplaceable part here for ions focusing, serving as a phase-space compressor that naturally compresses ions into a state of very low energy [91].

3.4.2 Quadrupole

Two quadrupoles, a long one (830 mm in length) and a short one (200 mm in length), are installed in the ion guide device. Each quadrupole has four identical cylindrical metal rods. The four rods are separated into two groups, each of which contains two rods, provided with high frequency AC voltage ($\approx 100 - 1000$ V) with opposite sign in positive and negative. In this way, the cluster ions can be confined and guided through the path in the quadrupole with high transmission. But when an additional DC voltage ($\approx 10 - 100$ V) is applied to the quadrupole with opposite sign in positive and negative on two groups of rods, only a certain mass range of ions are stable and can survive inside the quadrupole. All the other cluster ions are instable

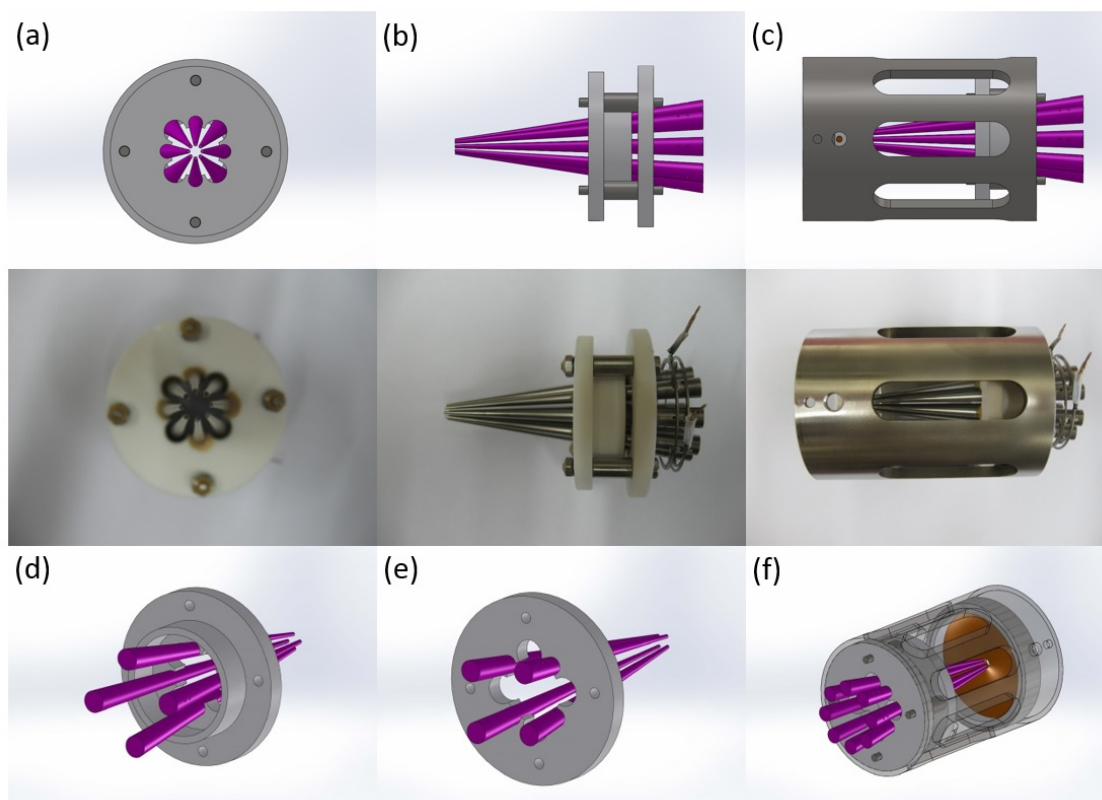


Figure 3.4 – Photos and model of the home-made conical octupole. (a) Top view. Side view (b) without (c) with the cylindrical tube. (d)-(f) The conical octupole is composed of two electrical isolated conical quadrupole. Here the diameter of the conical rod/octupole is 6/24 mm on one side and 1/4 mm on the other side respectively, and the vertical length of the octupole is 80 mm.

and will be filtered during the way of passing the quadrupole. In this way, the quadrupole serves as a mass selector.

According to the quadrupole theory [92, 93], the resolution of mass selection is

$$\frac{\Delta m}{m} = \frac{0.16784 - U/V}{0.126}, \quad (3.1)$$

where U and V are DC and AC voltages respectively. Clearly seen from the equation, a higher ratio of U/V results in a higher resolution, and the limit of $U/V = 0.16784$ gives the zero transmission. The long quadrupole with frequency of 880 KHz serves to mass select small cluster ions (1 – 4000 amu), and the short quadrupole with frequency of 440 KHz serves to mass select large cluster ions (1 – 16000 amu). This is because the maximum mass of ions that can be selected by the quadrupole (with 9.5 mm of diameter of the rods) is

$$m_{max} = \frac{0.822 V_{max}}{f^2}, \quad (3.2)$$

where f is the AC frequency of quadrupole.

3.4.3 Electrostatic lens

An electrostatic lens is composed of three hollow cylindrical metal plates. By tuning the voltages on the plates, normally a high voltage on the central piece and low voltage on two side pieces, an electric field with wave-packet shape can be formed, realizing the ion focusing. It's similar to the focus of light by an optical lens. Compared to conical octupole, electrostatic lens is easier to be used with small collision of clusters at low pressure.

3.4.4 Ion deflector

A deflector is composed of four hyperbolic-shaped rods as a quadrupole. When a low voltage is applied on one rod and a high voltage is applied on the other three, the beam of cluster ions will pass in and out the deflector by bending 90 degree around the rod with low voltage [94]. In this way, the ion beams will be bent and the neutral clusters will be filtered out from the ion guide device because the neutral particles do not respond to the electric field and always go straight. By manipulating the voltages on the deflector rods, the ions beam can be bent to the other direction. In this case, the current of the ions beam can be measured either by a channeltron (if the intensity of the beam is large) or a Faraday cup (if the intensity of the beam is small).

3.5 Pyridine injector

The experimental apparatus can also generate cluster-organic compounds like silver-pyridine clusters, as shown in figure 3.5. A pulsed electrical valve is installed to inject pyridine molecules from the reservoir into the vacuum chamber through a teflon tube. The other side of the tube connects to the conical octupole, guiding the pyridine molecules into the trajectory of silver clusters beam. The vapor pressure of pyridine is about 10^{-2} mbar at room temperature. With high pressure and strong collision inside the octupole, these pyridine molecules and silver clusters will form into silver-pyridine compounds. The efficiency of the generation of silver-pyridine can be optimized by manipulating the parameters of the pulsed valve (e.g. the opening time and the frequency).

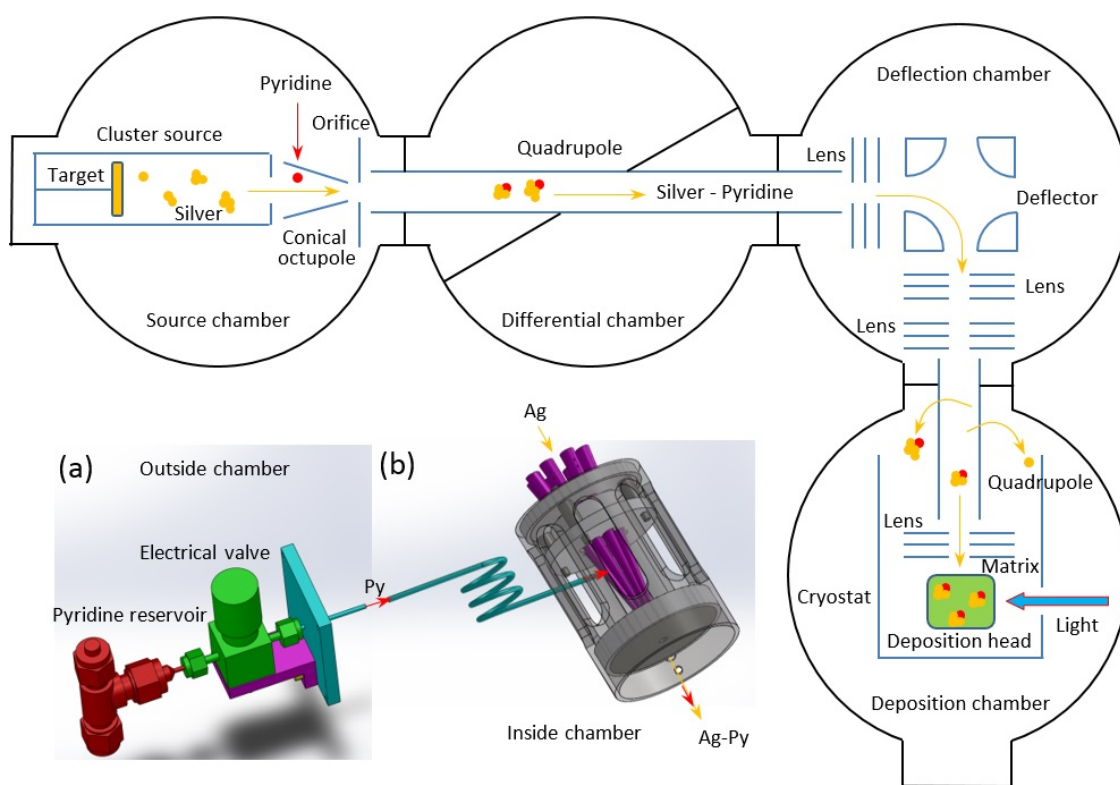


Figure 3.5 – Sketch of the experimental setup for fabrication, mass-selection and deposition of small metal clusters combined with organic compounds embedded in rare gas solid matrix. Here the inset of (a) shows the way of injection of organic compounds into vacuum chamber, and (b) shows the way of combination of metal clusters with organic compounds in a conical octupole.

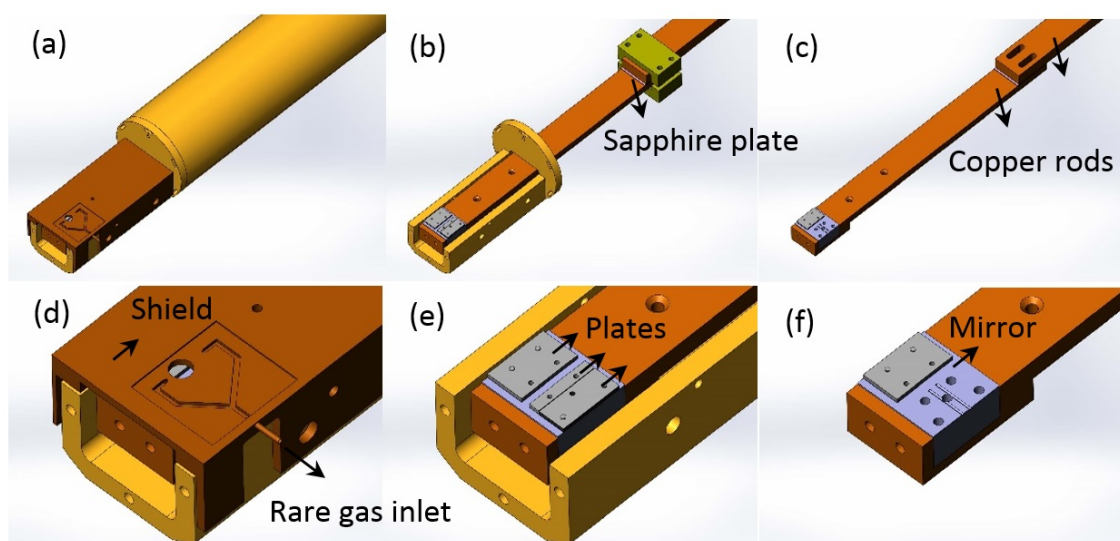


Figure 3.6 – 3D model of our sample holder of, which includes a polished aluminum mirror, three aluminum fixing plates, a copper shield and two copper rods that fixed by a sapphire plate.

3.6 Deposition head

The above discussions showed the fabrication and the guidance of clusters from cluster source to the ion guide device. In this Section, we will show how the clusters are soft-landed and deposited in the rare gas solid matrix on deposition head which has been done in previous thesis [87, 95].

3.6.1 Sample holder

Figure 3.6 show the sample holder, which includes a polished aluminum mirror, three aluminum fixing plates, a copper shield and two copper rods. The aluminum mirror, where the matrix sample is formed and the cluster current is detected, is fixed on the lower copper rod. The mirror offers a region of $2\text{ mm} \times 20\text{ mm}$ for the deposition. This region is confined by three aluminum plates that are electrically isolated from the mirror by kapton foil with a thickness of $50\text{ }\mu\text{m}$. The copper shield is further fixed above the plates with electrically isolation as well. The combination of mirror, plates and shield serve as an electrostatic lens, and by tuning the voltages, the ion beam can be focus on the mirror and the clusters can be soft-landed.

3.6.2 Cryostat

The sample holder needs to be cooled to cryogenic temperature in order to be able to condense rare gases. Hence, a cryostat is used here, which connects to the upper copper rod. The lower

copper rod with the aluminum mirror is then fixed on the upper rod with a depolished sapphire plate which allows good thermal contact and an electric isolation in order to make the measurement of cluster current on the aluminum mirror possible. The cooling is achieved with a plused tube cryocooler (SRP-052A, Sumitomo Heavy Industries Ltd.) using a helium compressor (CSW-71, Sumitomo Heavy Industries Ltd.). Temperature as low as 4.2 K with a cooling power of 0.5 W can be obtained. The copper shield works as a protection from the thermal radiation to the aluminum mirror. With the shield, temperature as low as 5 K can be achieved for the deposition region. This temperature is sufficient to condense neon since the sublimation temperature of neon is about 9 K at 10^{-8} mbar. All the temperatures are measured by the silicon diodes based on LakeShore 330 temperature controllers.

3.6.3 Rare gas inlet

Gas inlet for the deposition is located on the right side of the shield, with an outer diameter of 1 mm and an inner diameter of 0.5 mm. Injection of the gas onto the deposition region is achieved through a network of tubes within the shield ending with two tubes with an angle of 30° with respect to the surface of the deposition region. The rare gas will be solidified on the aluminum surface and form a matrix. During the same time, the incoming metal clusters will be soft-landed on the matrix surface, and embedded into the rare gas solid matrix with time of matrix growing. The rare gas pressure between $1 \times 10^{-5} - 2 \times 10^{-5}$ mbar is used during the deposition, the duration of which is between 1 – 4 hours.

3.6.4 Filament

The sample holder is placed after the ion guide device and aligned by the orifice on the shield. As discussed before, only the ions of clusters can be bent by the deflector and the neutral clusters will be filtered. So the positive charged clusters coming out from the last piece of electrostatic lens will fly into the sample holder and deposit on the aluminum mirror. But with time, the matrix will get more and more charged and make it more and more difficult to deposit ions. The typical charging time is about 10 s in our system. Therefore, a tantalum filament is placed close to the exit of the lens before the sample holder (as shown in figure 3.7) to neutralize the matrix by donating low energy electrons, which makes long time deposition possible.

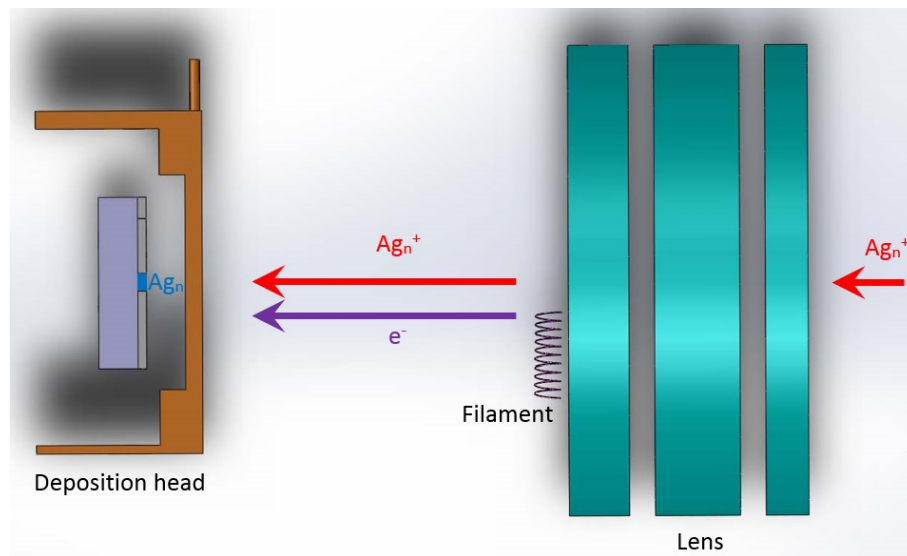


Figure 3.7 – Neutralization of positive cluster ions by the donation of electrons from a filament between the lens and the deposition head.

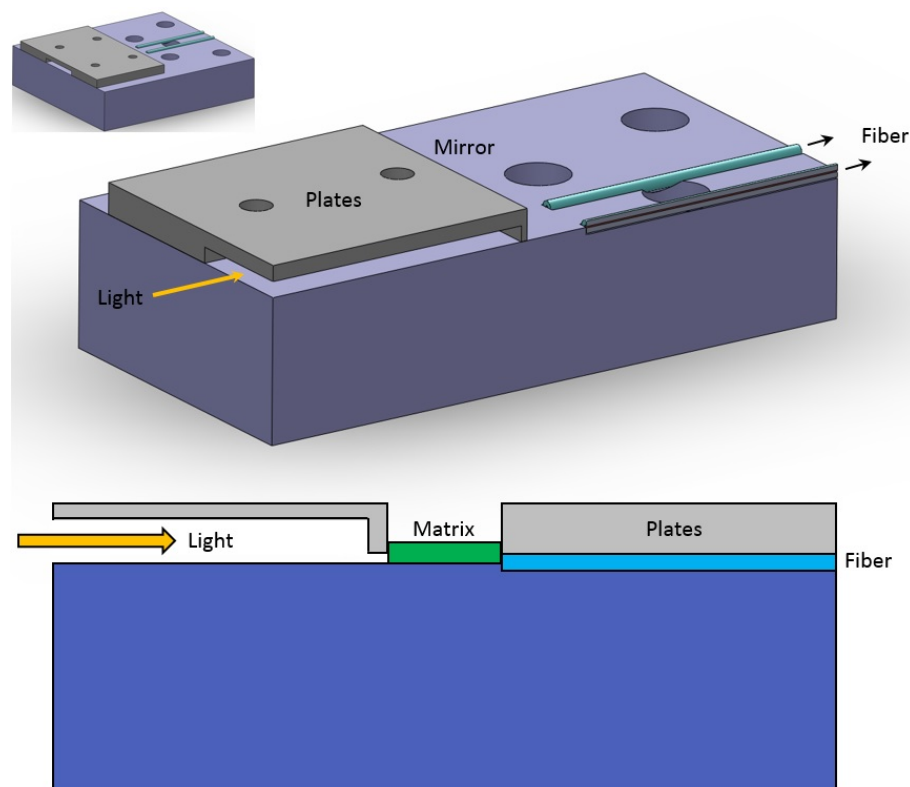


Figure 3.8 – Collection of optical signals by two optical fibers clamped inside the deposition head.

3.7 Optical setup

The optical setup is also an important part of the apparatus for the study of optical properties of small metal clusters. There are four main optical measurements: optical absorption, fluorescence, optical excitation and Raman scattering.

3.7.1 Light source and spectrometer

A T64000 spectrometer coupled to a liquid nitrogen-cooled charge coupled device is used for all the optical analyze. A deuterium (D₂) lamp (L7296, Hamamatsu Photonics K.K.) and a tungsten (W) lamp are used for the measurement of optical absorption. The diode lasers with separated wavelengths of 266, 375, 450, 473, 532, 635 nm and a YAG-MOPO laser with continuous wavelength of 450 – 650 nm are used for the measurements of fluorescence, excitation and Raman scattering.

3.7.2 Fixed optical fiber

The sample holder mentioned before is designed not only for the deposition of clusters in matrix but also for the optical measurements. As shown in figure 3.8, the aluminum mirror is constructed to increase the optical path (about 2 mm), by working in a plane perpendicular to the deposition. The aluminum plates serve to clamp one end of two fibers to collect the luminescence at less than 0.2 mm from the deposition region. The other end of the fiber is connected to the spectrometer. Two grooves are especially engraved on the aluminum mirror for this purpose. These optical fibers have a core diameter of 400 μm and a high transmission in 220 – 1000 nm, and are solarization-resistant (400-SR, Ocean Optics Inc.).

3.7.3 Optical absorption

The measurement of optical absorption is performed by injecting the light from the D₂ lamp or W lamp through the 2 mm length of the matrix and collecting the residual light on the other side with the optical fiber, as shown in figure 3.8. The collected light is analyzed by the optical spectrometer. Comparing the intensity of the light passing through a matrix doped with clusters to a reference signal of light passing through a pure neon matrix yields the optical absorption spectrum. According to the Beers law, the light intensity after absorption can be written as:

$$I = I_0 e^{-\alpha x}, \quad (3.3)$$

where I_0 is the light intensity before absorption, α is the absorption rate and x is the length of the matrix. To increase the sensitivity, the matrix need to fully cover the light passing directly

to the fiber, which means the thickness of matrix should be larger than the core radius of the fiber. The determination of the matrix thickness is made by measuring the intensity of light coming from a D₂ lamp that passes through the matrix solid which is collected by the optical fiber. The intensity decreases gradually as the thickness of the matrix grows. The reduction of intensity is due to the scattering of the light on the polycrystalline matrix and increases strongly with decreasing wavelength.

3.7.4 Fluorescence collection

The measurement of fluorescence is performed by injecting the laser light perpendicular to the surface of matrix, as shown in the blue trajectory of figure 3.9. Then there are two ways of the collection of fluorescence light. One way is collecting the light by the optical fiber mentioned before. In this way, less background of laser source will be intervened. The other way is collecting the light by an external fiber through two optical lenses, as shown in the red trajectory of figure 3.9. In this way, more fluorescence signal can be captured. Usually, the first way is used when the difference of wavelength between the incident laser and the out-coming fluorescence is large, and the second way is used when the difference is small.

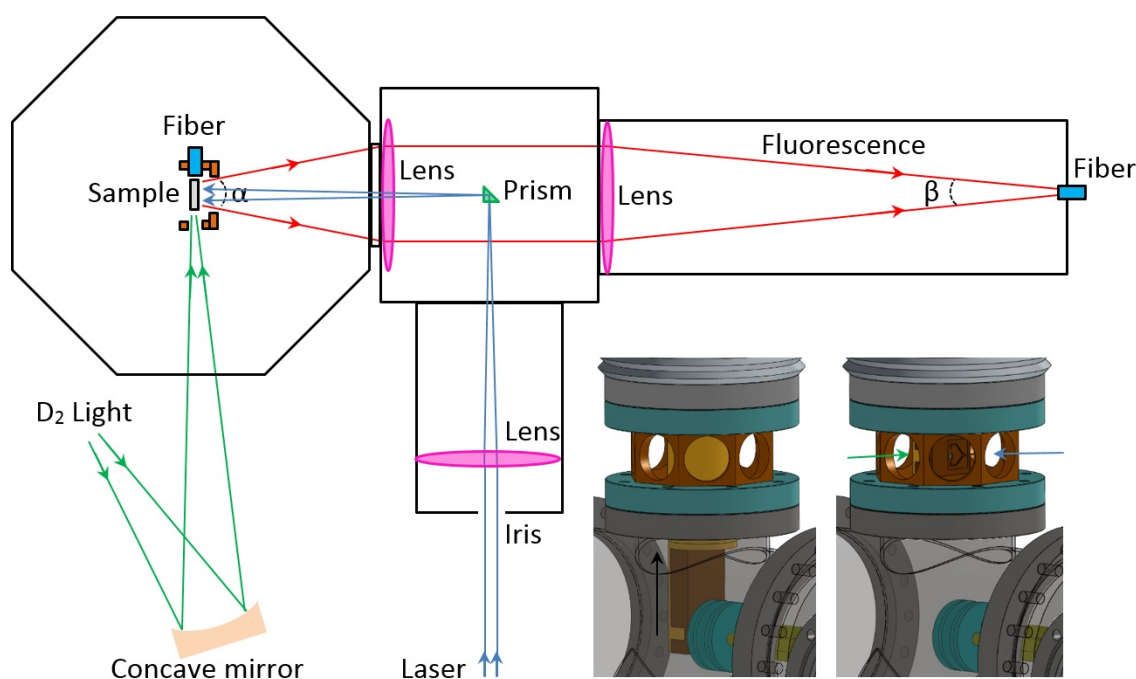


Figure 3.9 – Diagram of optical setup for the measurements of absorption, fluorescence and Raman scattering. Here the green lines represent the incident D₂ light for absorption measurement, the blue lines represent the incident laser for fluorescence or Raman measurement, and the red lines represent the out coming fluorescence or Raman signals.

3.7.5 Excitation measurement

The measurement of excitation is performed based on the the fluorescence signal by sweeping the wavelength of the incident light. The intensity of fluorescence response to the wavelength provides the excitation spectrum.

3.7.6 Raman measurement

The measurement of Raman scattering is performed the same way as that of fluorescence except for the replacement of a 300 lines/mm grating by a 2400 lines/mm one in the spectrometer. This is because for the Raman measurement, a higher resolution is essential. In this way, the resolution is enhanced by 8 times with the compensation of the reduce of the detection area to 1/8 times.

3.8 Simulations of ion particles passing through the device

In order to test the ion guide device as discussed in Section 3.4, we have performed simulations on cluster ions passing through the device by SIMION which is a software package used primarily to calculate electric fields and trajectories of charged particles in those fields via solving Laplace equations when given a configuration of electrodes with voltages and particle initial conditions [96].

3.8.1 Transmission of cluster ions

Figure 3.10(a) shows the simulation of ions passing through the device. As an example, here we use a group of 1000 ions with charge of +1 and mass of 5000 – 6000 amu starting at the entrance of the octupole with a homogeneous particle distribution of 4 mm in radius and an initial speed of 180 m/s (corresponding to 1 eV for 6000 amu).

One of the most significant factors for ion guide is the transmission of ions passing through the device. Figure 3.10(b) shows the distribution of number of cluster ions passing in (red bars) and out (blue bars). We found a transmission as high as 25% in the size range selected.

Another important factor is the kinetic energy of cluster ions at the exit of the ion guide since we want to soft-land the clusters which requires a low deposition energy of about 1 eV/atom [97]. Figure 3.10(c) shows the distribution of ion speed passing out each piece of device. Note that, for Ag clusters, the speed of 10^3 m/s corresponds to the kinetic energy of 0.56 eV/atoms. It is worth mention here that the initial ion speed of 180 m/s is the gas speed in the aggregation tube of the cluster source at liquid nitrogen temperature. We clearly see from figure 3.10(c) that the landing energy of clusters passing out from the last piece of ion guide device is about 0.1 – 0.5 eV/atom, largely sufficient for soft-landing.

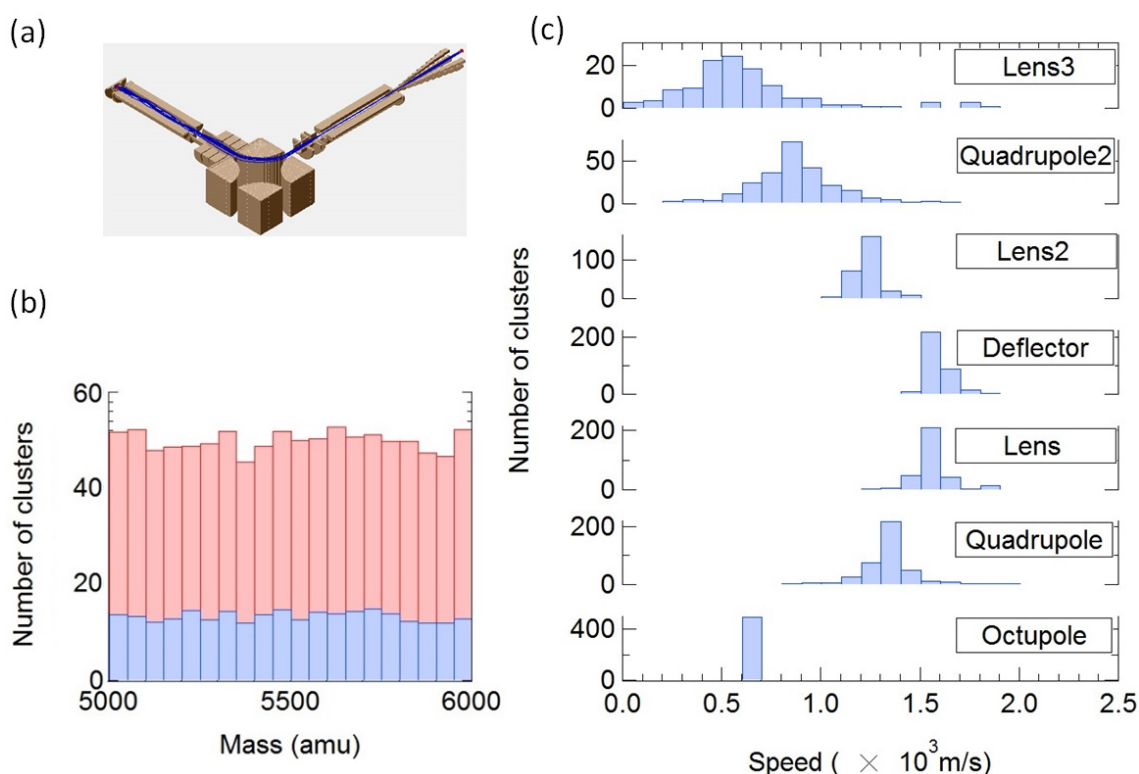


Figure 3.10 – (a) Diagram of SIMION simulation of cluster ions passing through the ion guide device, where the blue curves show the trajectories. (b) Distribution of number of cluster ions passing through the device. (c) Distribution of speed of cluster ions passing out each piece of device. Here the red (or blue) bars represent the cluster ions passing in (or out) the device.

3.8.2 Ions focusing and pre-mass selection

As discussed before, the home-made conical octupole was designed to focus the cluster ions. Figure 3.11(a) shows the simulations of particles passing in (red dots) and out (blue dots) the octupole. As clearly seen, the initial diameter of incoming cluster beam has been reduced from 8 mm to 3 mm when the particles pass out the octupole. This manifests that the conical octupole works well for the ion focusing. Figure 3.11(b) shows the transmission of clusters passing through the octupole. With mass ranged from 100 to 16,000 amu, cluster ions have an average transmission of about 70%. This means that the density of cluster beam passing through the octupole has been enhanced 5 times. Interestingly, as shown in figure 3.11(b), the optimal mass of cluster ions with the highest transmission can be manipulated by changing the AC voltage of octupole. The higher the voltage is, the larger the mass will be as expected. This means that the octupole also works as a pre-mass-selector.

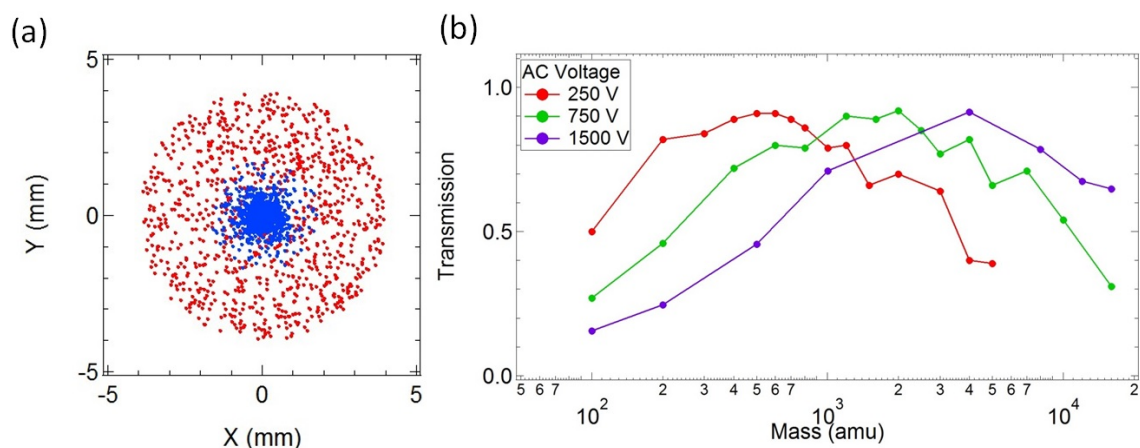


Figure 3.11 – Simulations of (a) cluster ions focusing and (b) pre-mass-selection by conical octupole with radio frequency of 2.4 MHz. Here the red (or blue) dots in (a) represent the cluster ions passing in (or out) the device.

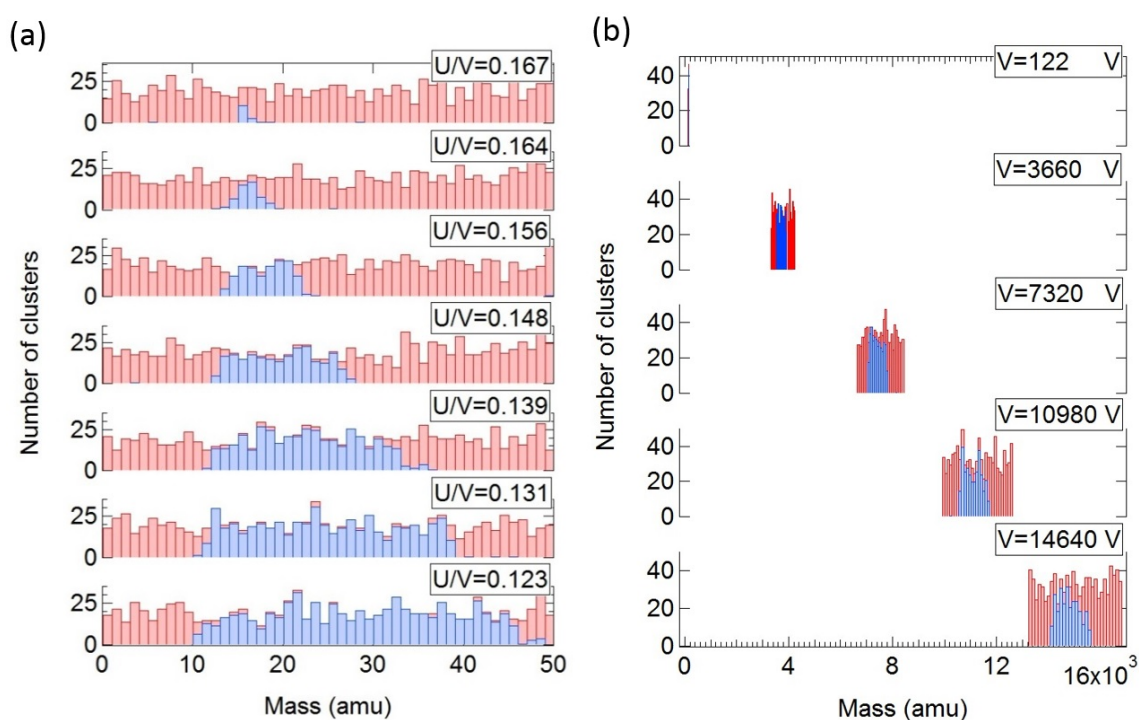


Figure 3.12 – Simulations of (a) resolution and (b) center mass shifting of mass selection of cluster ions by quadrupole with radio frequency of 1.0 MHz. Here the red (or blue) bars represent the cluster ions passing in (or out) the device.

3.8.3 Mass selection and resolution

Different from the octupole that roughly mass selects the ions with a low resolution, the quadrupole serves as a real mass selector. Theoretically, cluster ions passing through a

quadrupole will be mass selected and only a certain part of clusters with mass range of $m = m_0(+or-)\Delta m$ are stable and can survive inside the quadrupole. Here $m_0 = 0.822 \frac{V}{f^2}$ is the center mass of selected ions and $\Delta m = m_0 \times \frac{(0.16784 - U/V)}{0.126}$ is the resolution of mass selection, where U (or V) is the DC (or AC) voltage and f is the radio frequency of quadrupole. Usually when a resolution is chosen, the ratio of U/V (< 0.168) is fixed. Figure 3.12(a) shows the resolution of mass selection by the quadrupole as a function of U/V, and figure 3.12(b) shows the mass of selected ions as a function of V. Note from simulations that the response of resolution to mass is asymmetric, where the ions with lower mass are more sensitive to the mass selection than those with higher mass, as shown in figure 3.12(a). All of these simulation results are consistent to the quadrupole theory, which proves the reliability of the simulations.

3.9 Mass spectra

3.9.1 Mass selection and ion detection

As discussed in Section 3.4.2, the quadrupole serves as a mass selector. Cluster ions passing through it will be mass selected and only a certain part of clusters are stable and can survive inside the quadrupole. As changing the voltage (both DC and AC) through the range from minimum to maximum, a scanning of selected mass of cluster ions through the range of 1 – 16,000 amu will be given, showing a mass spectrum. The signal of cluster ions is detected by the aluminum mirror on the deposition head. All the electric currents are measured by Keithley 6517A electrometers. Please note, in experiment, we first sweep the voltage of quadrupole to obtain a whole range of mass spectrum, and then fix the voltage response to one size for the deposition of mass selected clusters.

3.9.2 Resolution and purity of mass selection

As shown in figure 3.13, if the single size spectrum has a Gaussian shape (see blue curve):

$$I = I_0 \times \exp(4 \ln 2 \times (m - m_0)^2 / \Delta m^2), \quad (3.4)$$

then the resolution of mass selection can be calculated as:

$$\begin{aligned} \Delta m / m_0 &= (\ln 2 / \ln(2/\alpha))^{1/2} & \text{when } \alpha \ll 1 \\ &= (\ln 2 / \ln(2/\alpha - 1))^{1/2} & \text{when } \alpha \approx 1, \end{aligned} \quad (3.5)$$

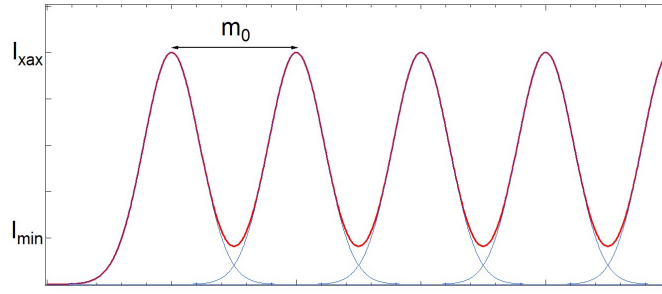


Figure 3.13 – Theoretical result of a mass spectrum on clusters with mass separation of m_0 .

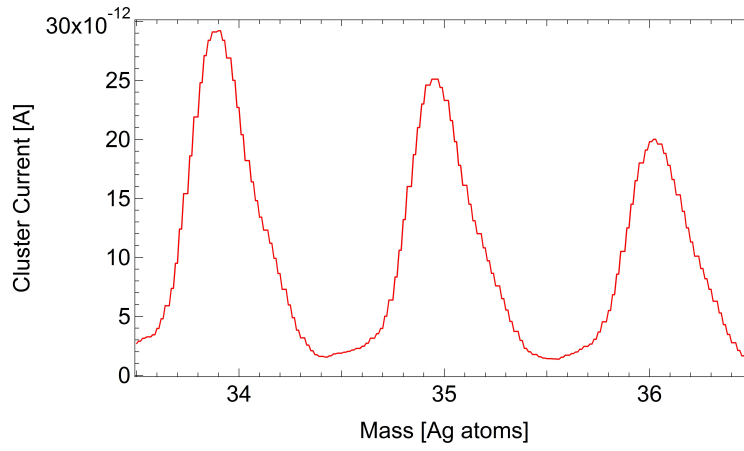


Figure 3.14 – Experimental result of mass spectrum of Ag clusters with size of 34, 35 and 36 atoms.

where $\alpha = I_{min}/I_{max}$ and m_0 is the mass separation of two neighbor sizes of clusters (see red curve). The proportion of ion current of the neighbor cluster of Ag_{n-1} (or Ag_{n+1}) response to that of selected cluster of Ag_n , that is approximately half of the impurity of Ag_n , is:

$$\begin{aligned} \beta &= (\alpha/2)^4 & \text{when } \alpha \ll 1 \\ &= (\alpha/(2-\alpha))^4 & \text{when } \alpha \approx 1, \end{aligned} \quad (3.6)$$

where $1 - 2\beta$ is the purity of Ag_n . Figure 3.14 shows the experimental result of mass spectrum of Ag clusters with size of 34, 35 and 36. Cluster current of about 30 pA (I_{max}) is obtained at one cluster size, and 2 pA (I_{min}) at the middle between two sizes with a separation of $m_0 = 108$ amu. Hence, according to equations and , the resolution of mass selection here is $48/108$ amu and the purity of Ag_{35} is $1 - 10^{-6}$ which is good enough for single size selection.

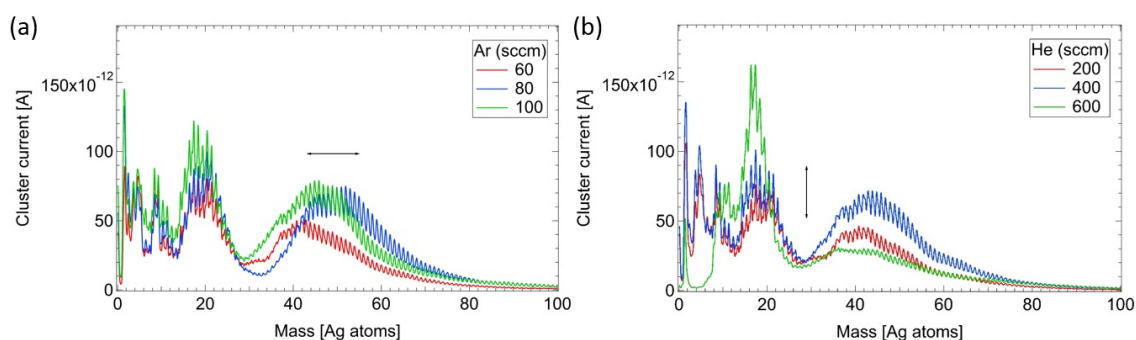


Figure 3.15 – Experimental mass spectra of Ag clusters response to the gas flux of Ar and He respectively.

In experiment, we sweep the voltage of quadrupole to obtain a mass spectrum. For the deposition of mass selected clusters, a voltage response to one size at the peak of mass spectrum is fixed, for example at the peak of Ag_{35} in figure 4.2.

3.9.3 Response to gas parameters

As discussed in Section 3.3, the parameter of cluster source play an important role on the size of clusters generated inside. Figure 3.15 shows the experimental mass spectra of Ag clusters response to the gas flux of Ar and He respectively. Ag clusters with mass range of 1 – 100 atoms are fabricated by the source. Cluster currents of about 100 pA are found on the aluminum mirror of the sample holder. The mass spectra show multi-peaks separated by the mass of 108 amu under an oscillated envelope including 3 groups of (1 – 10 amu), (10 – 30 amu) and (30 – 80 amu). The resolution of mass selection here is about 90/108 amu.

Interestingly, when the Ar flux is changed from 60 sccm to 100 sccm continuously, the curve of spectrum will move right and left in the direction of mass. By contrast, when the helium flux is changed from 200 sccm to 600 sccm, the curve of spectrum will move up and down in the direction of current. This means, as shown in figure 3.15, by controlling the gas flux of Ar and He, the position and the amplitude of mass spectrum can be manipulated.

3.9.4 Size selection shift

Figure 3.16 shows the experimental result of mass spectra of Ag clusters in the size range of 0 – 140 atoms in 4 cases with different parameters. Figure 3.16(a) shows a mass spectrum under an envelope with 2 groups, mainly in the range of 0 – 60 amu with current of cluster ions of about 400 pA. Figure 3.16(b) shows a mass spectrum under an envelope with 4 groups, mainly in the range of 0 – 80 amu with current of cluster ions of about 100 pA. Figure 3.16(c) shows a mass spectrum under an envelope with 5 groups, mainly in the range of 0 – 120 amu with current of cluster ions of about 150 pA. Figure 3.16(d) shows a mass spectrum under an

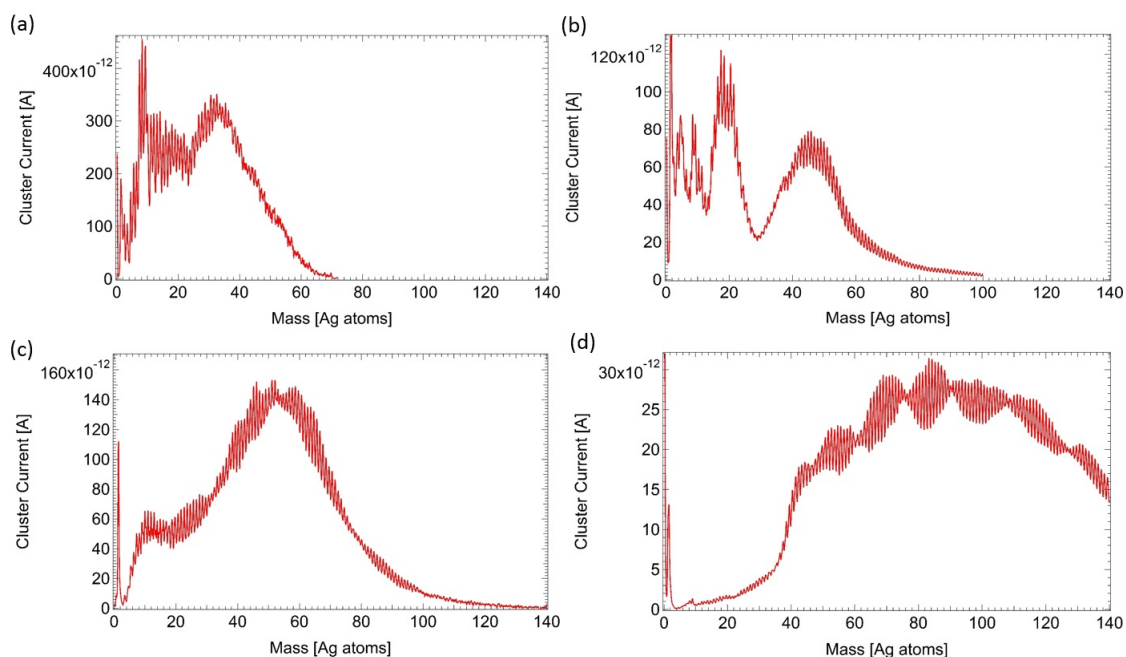


Figure 3.16 – Experimental result of mass spectra of Ag clusters in the size range of 0 – 140 atoms with different parameters.

envelope with 7 groups, mainly in the range of 0 – 140 amu with current of cluster ions of about 30 pA. These envelopes manifest a beat effect such as the interference between two acoustic waves. This may due to the interference of the radio frequency by two quadrupoles in the ion guide device.

3.9.5 Resolution effect

Figure 3.17 shows the experimental result of mass spectra of Ag clusters in the size range of 0 – 70 atoms. Figure 3.17(a) gives a current of cluster ions of 300 pA and a resolution of mass selection of 94/108 amu with purity of 95%, and figure 3.17(b) gives a current of cluster ions of 10 pA and a resolution of mass selection of 59/108 amu with purity of 99.9999%. As clearly seen, compared with figure 3.17(a), figure 3.17(b) shows a much better resolution and purity but a smaller current as compensation. In experiment, the current is usually optimized with a tolerance of purity of about 99%.

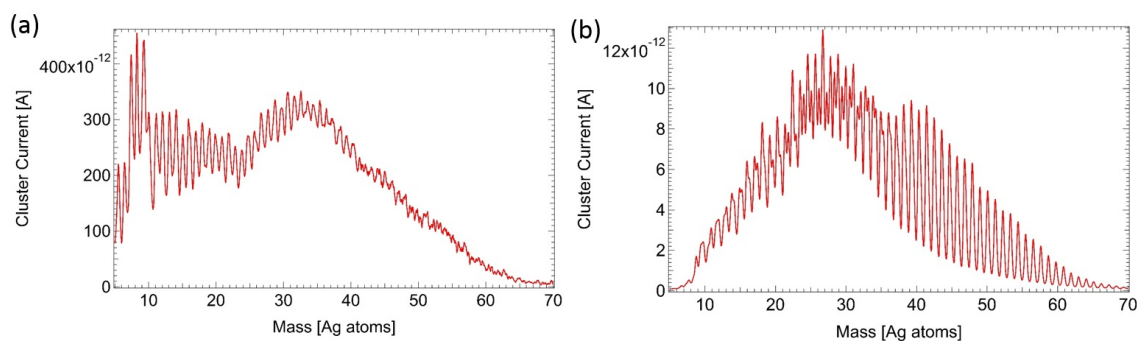


Figure 3.17 – Experimental result of mass spectra of Ag clusters with different resolutions.

3.9.6 Isotope spectrum

All the experimental spectra shown before are under mass selection by the short (second) quadrupole. Figure 3.18 shows the mass spectrum of Ag_n ($n = 1 - 5$) by the long (first) quadrupole. Interestingly, the isotopes of silver (107 and 109 amu) can be seen from the spectrum. This manifests that the resolution of mass selection here is better than 2 amu. Actually, as said before, a tolerance of the purity of 99% (equals to the resolution of 60 amu for Ag) is enough for the deposition of clusters of pure silver. But for the deposition of clusters of complex like silver-pyridine ($\text{Ag}_a\text{-Py}_b$), a good resolution is essential for the separation of different clusters. For example, the mass difference of $\text{Ag}_1\text{-Py}_5$ (503 amu) and $\text{Ag}_4\text{-Py}_1$ (511 amu) is only 8 amu.

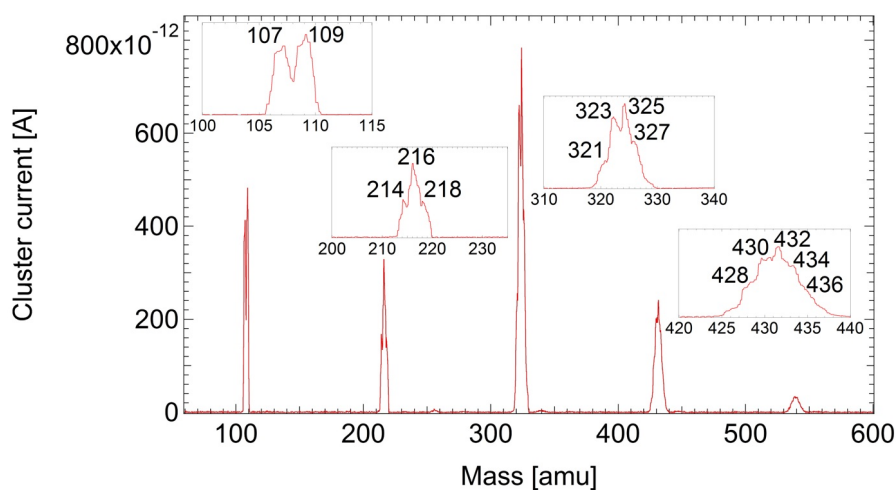


Figure 3.18 – Experimental result of mass spectrum of small silver clusters with high resolution of about 1 amu.

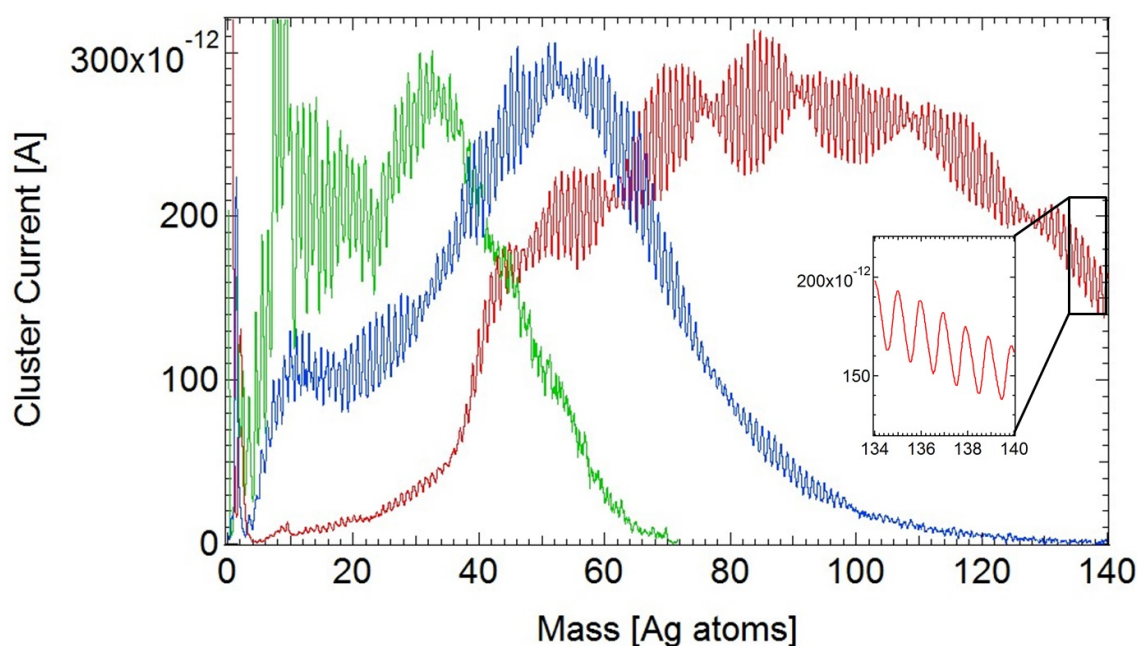


Figure 3.19 – Three groups (red, blue and green) of mass spectra of silver clusters in the range of 1 – 140 atoms with different parameters of cluster source. Red: $P = 27$ w, $\Phi(\text{Ar}) = 96$ sccm, $\Phi(\text{He}) = 410$ sccm, $p = 0.46$ mbar. Blue: $P = 18$ w, $\Phi(\text{Ar}) = 88$ sccm, $\Phi(\text{He}) = 245$ sccm, $p = 0.58$ mbar. Green: $P = 34$ w, $\Phi(\text{Ar}) = 95$ sccm, $\Phi(\text{He}) = 360$ sccm, $p = 0.42$ mbar. Here P is the discharge power of cluster source between anode and cathode, $\Phi(\text{Ar})$ and $\Phi(\text{He})$ are the flux of Ar and He gas, and p is the gas pressure inside the aggregation tube.

3.9.7 Silver clusters spectra

The parameters of the cluster source play an important role on the distribution of cluster sizes. Figure 3.19 shows the experimental results of three groups of mass spectra of Ag clusters response to different parameters of cluster source, which cover the whole range of size from 1 to 140 atoms continuously. Cluster current of 100 – 300 pA with resolution of about 90 amu and purity of about 95% are found in the green group with 1 – 40 atoms, the blue group with 20 – 70 atoms, and the red group with 50 – 140 atoms. Note that the resolution and purity can be improved with the compensation of the decrease of cluster current. Here all the three groups manifest a beat effect on the envelopes of spectra such as the interference between two acoustic waves. This may result from the interference among different sets of parameters of the cluster source. Please note, although only mass spectra of silver clusters are shown here, this machine can also produce size selected clusters of other metal materials like gold and copper.

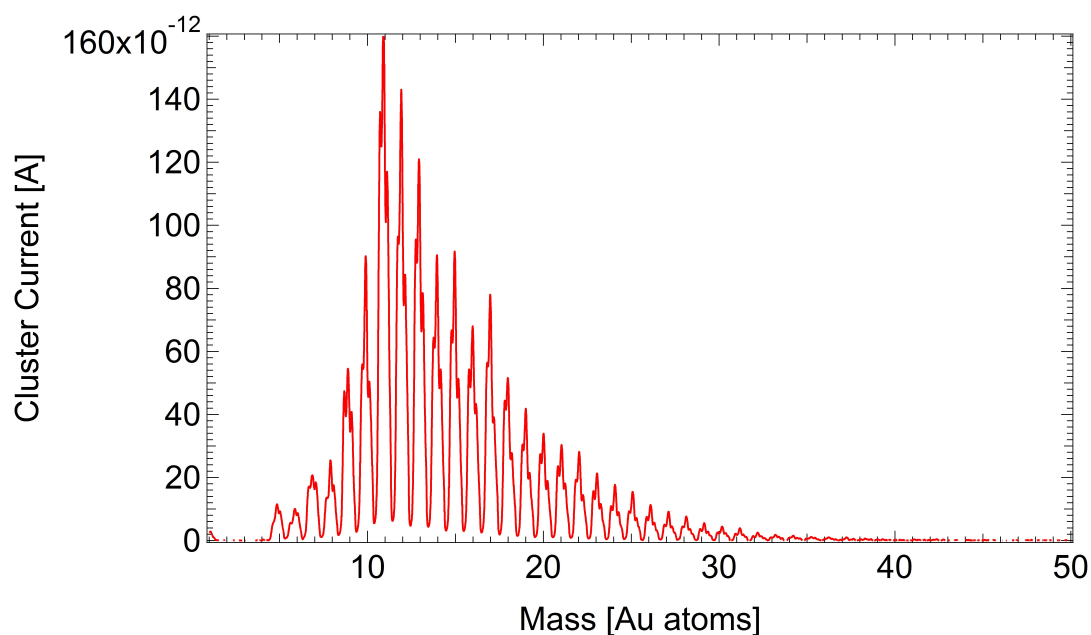


Figure 3.20 – Experimental result of mass spectrum of Au clusters.

3.9.8 Gold clusters spectra

By replacing the silver target with a gold target, the gold clusters can be fabricated by the cluster source and mass selected by the quadrupole as the same way. Figure 3.20 shows the experimental result of a typical mass spectrum of Au in the size range of 5 – 30 atoms. The spectrum is optimized for Au_{11} with a current of 160 pA and a resolution of 88 amu. Different from Ag clusters, the Au clusters have a mass separation of 197 amu instead of 108 amu. So for Au clusters, the purity is higher than Ag clusters with a same resolution. But for the same size, Au clusters have a larger mass, which results in the reduction of the limitation in size selected by quadrupole.

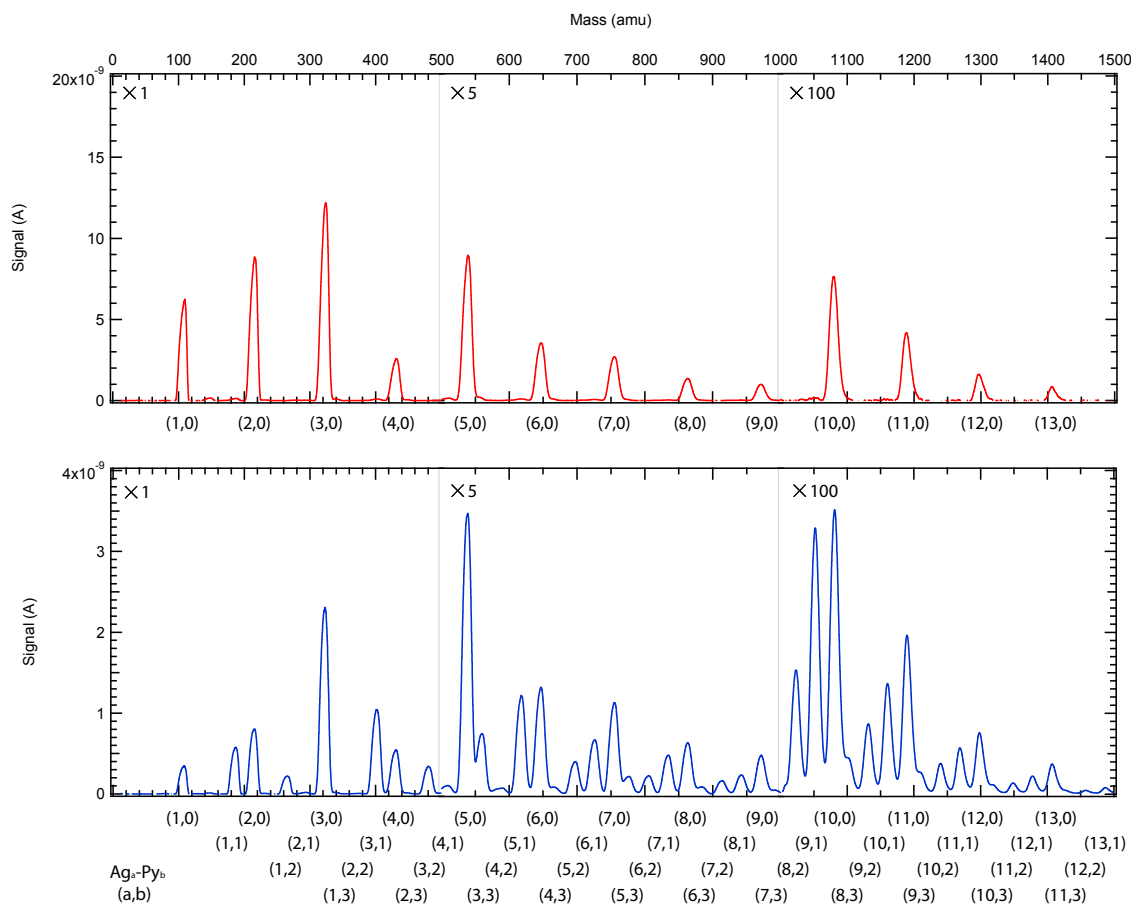


Figure 3.21 – Experimental result of mass spectra of Ag_n ($n=1-13$) and Ag_a-Py_b ($a=1-13$ with $b=0-3$) when the pyridine is injected or not respectively.

3.9.9 Silver-pyridine clusters spectra

As shown in figure 3.5, by opening the electric valve of pyridine, the Ag_a-Py_b clusters will be fabricated in the conical octupole and mass selected by the quadrupole as the same way for Ag_n clusters. A big challenge for the deposition of mass selected Ag_a-Py_b clusters is its single size selection. As discussed before, the mass selection of Ag_a-Py_b clusters requires a high resolution, which makes it important to use the long quadrupole instead of the short one as the mass selector. Figure 3.21 (a) and (b) show the experimental result of mass spectra of Ag_n ($n=1-13$) and Ag_a-Py_b ($a=1-13$ with $b=0-3$) when the pyridine is injected or not respectively. The current of Ag_a-Py_b cluster ions is about 100 pA - 1 nA. As clearly seen, each Ag_a-Py_b cluster is well separated from its neighbors due to the high resolution. This is very important for the single size selection.

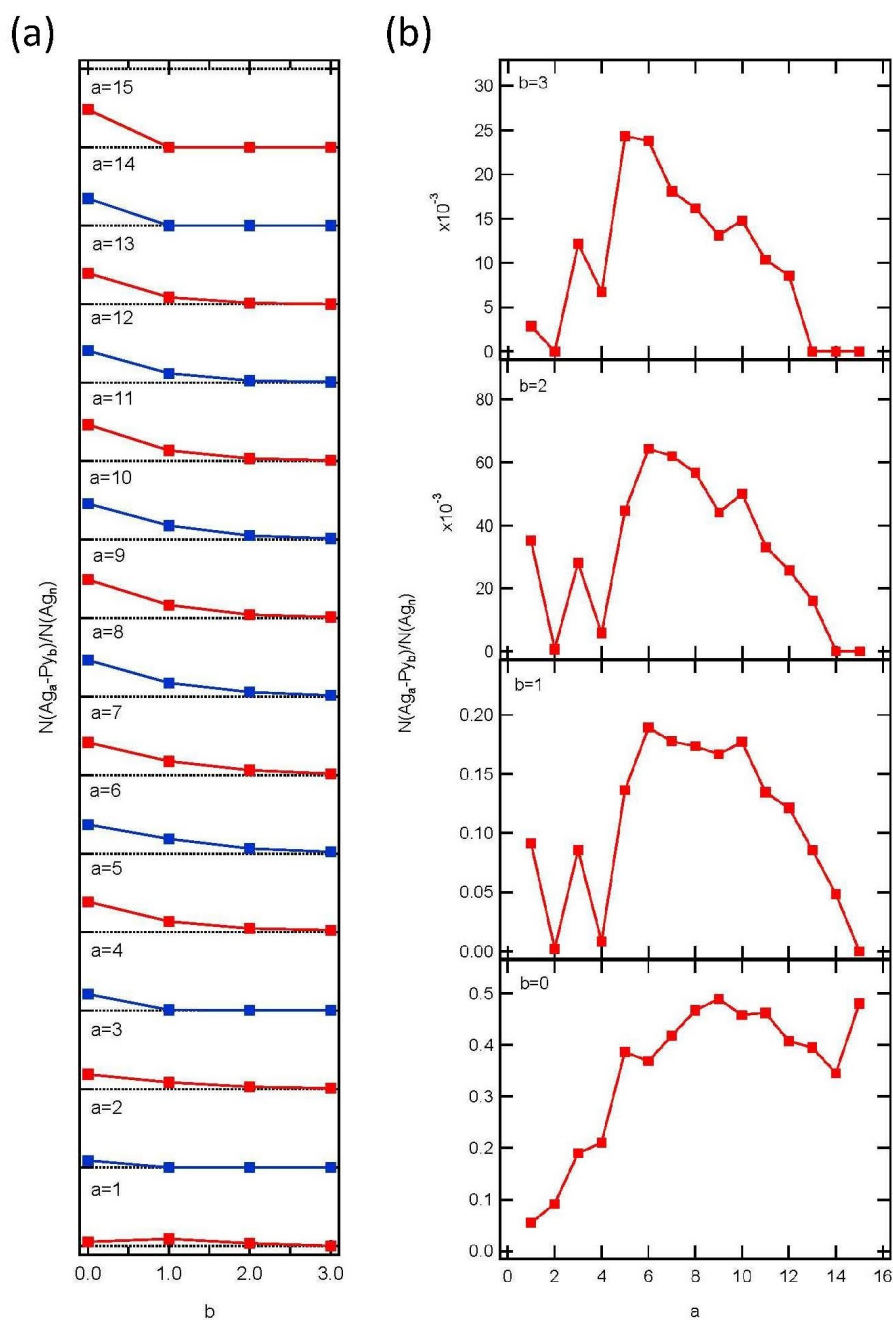


Figure 3.22 – (a)Statistic ratio of $\alpha_a(b) = N(Ag_a-Py_b)/N(Ag_n)$ of number of Ag atoms between Ag_a-Py_b clusters and Ag_n clusters response to the index number of pyridine of b with different index number of silver of a respectively. (b) Statistic ratio of $\beta_b(a) = N(Ag_a-Py_b)/N(Ag_n) = \alpha_a(b)$ of number of Ag atoms between Ag_a-Py_b clusters and Ag_n clusters response to the index number of silver of a with different index number of pyridine of b respectively.

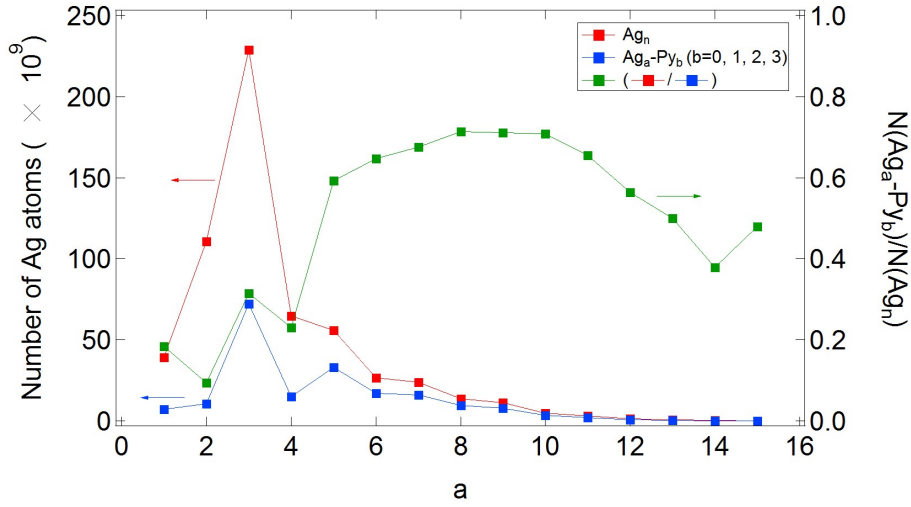


Figure 3.23 – The number of Ag atoms of Ag_n and Ag_a-Py_b clusters before and after the injection of pyridine respectively, and the ratio $\gamma(a) = \sum_b N(Ag_a - Py_b) / N(Ag_n) = \sum_b \beta_b(a)$ of total number of Ag atoms between Ag_a-Py_b clusters and Ag_n clusters response to the index number of silver of a.

Figure 3.22(a) shows the ratio

$$\alpha_a(b) = N(Ag_a - Py_b) / N(Ag_n) \quad (3.7)$$

of number of Ag atoms between Ag_a-Py_b clusters and Ag_n clusters response to the index number of pyridine of b with different index number of silver of a respectively. Except for Ag_1-Py_b , all the Ag_a-Py_b clusters show a decreased characteristic curve of current when b is increased. This manifests that the Ag_a-Py_b clusters with a smaller b is easier to be formed than those with a larger b. One possible case is that the Ag_a-Py_b clusters are formed as a sequence of Ag_a-Py_0 , Ag_a-Py_1 , Ag_a-Py_2 and Ag_a-Py_3 , where the latter is obtained by attaching one more pyridine atom on the former. The reason why Ag_1-Py_0 has a lower current than Ag_1-Py_1 is because the Ag atoms have been greatly donated for the formation of Ag_a-Py_b clusters.

Figure 3.22(b) shows the ratio

$$\beta_b(a) = N(Ag_a - Py_b) / N(Ag_n) = \alpha_a(b) \quad (3.8)$$

of number of Ag atoms between Ag_a-Py_b clusters and Ag_n clusters response to the index number of silver of a with different index number of pyridine of b respectively. Here β is the

survival rate of Ag_a from Ag_n after the injection of pyridine. Each group shows a different characteristic curve. The peak value of the curve is at a=9 for Ag_a-Py₀ group, at a=6 for Ag_a-Py₁ group, at a=6 for Ag_a-Py₂ group, and at a=5 for Ag_a-Py₃ group. This means that each group of Ag_a-Py_b clusters with different index number of pyridine of b has different response to the optimum number of combined silver atoms of a. Besides, here (1-β₀) reflects the consumption rate of pure Ag_n clusters after the injection of pyridine response to n. This sustains the assumption before that the Ag atoms have been donated most compared with all the other Ag_n clusters for the formation of Ag_a-Py_b clusters, since Ag₁ has the minimum value of β₀.

Figure 3.23 shows the number of Ag atoms of Ag_n and Ag_a-Py_b clusters before and after the injection of pyridine respectively, and the ratio

$$\gamma(a) = \sum_b N(Ag_a - Py_b) / N(Ag_n) = \sum_b \beta_b(a) \quad (3.9)$$

of total number of Ag atoms between Ag_a-Py_b clusters and Ag_n clusters response to the index number of silver of a. Here γ is the survival rate of Ag_n-Py_b from Ag_n after the injection of pyridine. In other way, (1-γ) reflects the deformation rate of Ag_n to Ag_n'Py_b after the injection of pyridine response to n. The optimum value of survival rate is at Ag₈-Py_b. As seen in the green curve compared with the bottom curve (b=0) of Figure 3.22(b), there are two valley values at Ag₂-Py_b and Ag₄-Py_b (not for Ag₂-Py₀ and Ag₄-Py₀). This means, for Ag₂ and Ag₄, it's more difficult to form silver-pyridine combination compared with the other Ag_n clusters.

3.10 Optical spectra (Ag₃)

Size selected silver clusters of Ag₃ with beam current of 200 pA and purity of 99% have been co-deposited with rare Ne gas at pressure of 1.5 × 10⁻⁵ mbar and temperature of 6 K during 2 hours. Figure 3.24 shows the experimental results of optical absorption spectrum of Ag₃ embedded in solid Ne matrix (red curve). Main absorption peaks at 2.52, 3.11, 3.52, 3.71, 4.06, 4.47, 4.64 and 4.80 eV are found in the spectrum, the result of which is consistent to the previous result (gray curve) [51] of Ag₃ fabricated by a sputtering source.

Figure 3.25 shows the experimental result of fluorescence spectra of Ag₃ excited by a 450 nm and a 473 nm laser respectively. A large fluorescent peak at 603 nm with FWHM of 9.0 nm is found for both excitations, which corresponds to the energy of 2.23 eV with FWHM of 0.015 eV in vacuum. Please note, here a blue shift of 0.17 eV is introduced due to the matrix effect of neon solid [98]. This is consistent to the previous fluorescence result found at 616 nm in Ag₃Ar system (corresponds to the energy of 2.26 eV by a blue shift of 0.25 eV for Ar matrix effect) [99].

All of these manifest that our experiment setup is reliable and works well for optical measurements on size selected metal clusters.

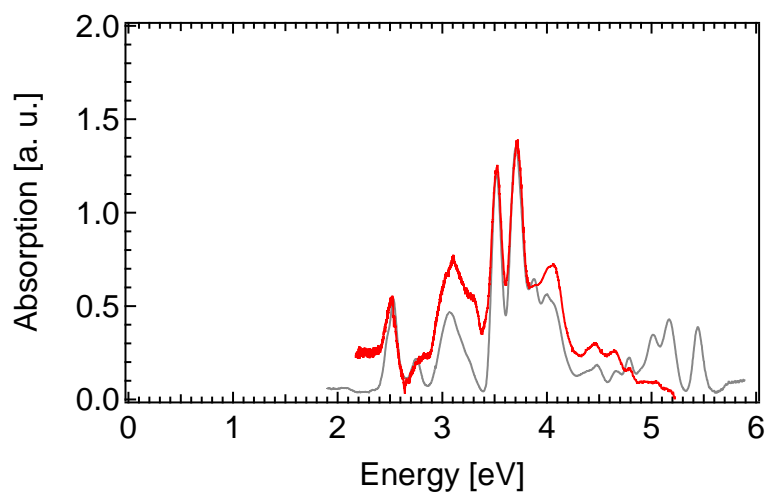


Figure 3.24 – Experimental result of optical absorption of Ag_3 in Ne matrix (red curve) compared with previous result of Ag_3 in Ar matrix (grey curve) [51].

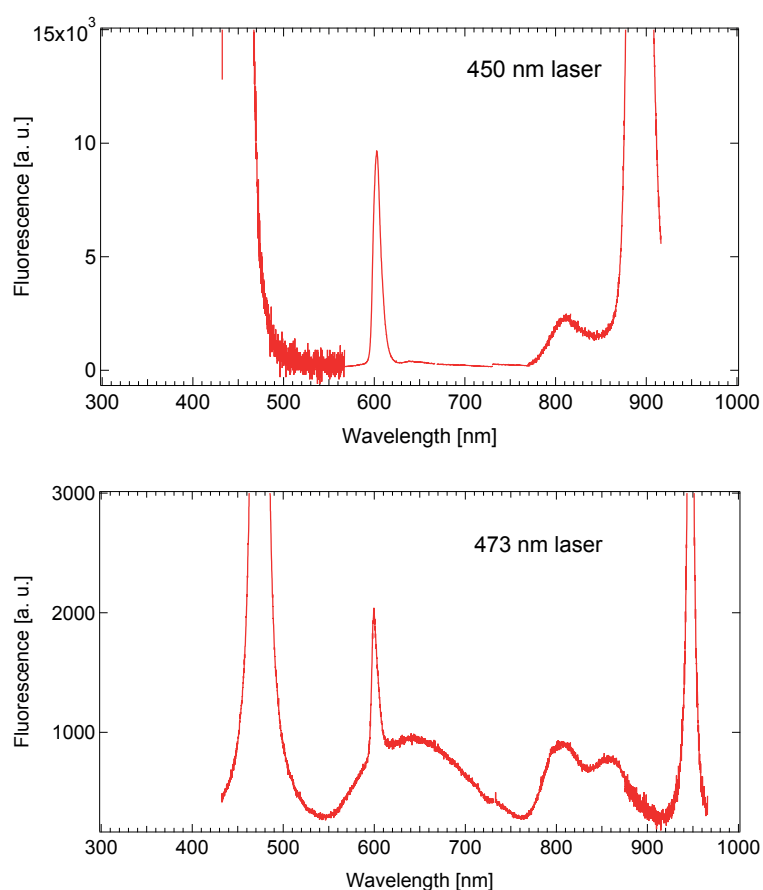


Figure 3.25 – Experimental result of optical fluorescence of Ag_3 in Ne matrix excited by a 450 nm and 473 nm laser respectively.

4 Result: Optical properties of silver clusters

Small noble metal clusters and nano-particles have unique optical properties related to the localized surface plasmon resonance which determine the optical absorption spectrum in the UV-visible wavelength range. These properties make them interesting for biolabelling, nanophotonics, light energy harvesting, sensing, electronics and catalysis [100, 42, 101, 102]. The determination and understanding of the optical properties of these small metal clusters are key for the development of applications. Larger particles in the nanometer size range can be characterized essentially in the framework of classical electromagnetic theory [42, 47] using the dielectric function of the bulk material. In the very small size range for noble metal clusters containing less than 10 atoms, single electron excitations dominate the optical spectra. They are successfully described in the framework of time dependent density functional theory (TDDFT) choosing appropriate functionals [51, 103]. In this size range, different isomers for one particular cluster size can be distinguished in the optical response experimentally as well as theoretically. There is strong interest in the intermediate, non scalable cluster size regime where the dielectric function evolves from single molecular transitions into the bulk regime and where each constituent atom changes the physical property of the cluster under investigation [49]. For the optical properties this is the range where molecular like electronic transitions evolve into surface plasmon resonances whose shape depend on the symmetry of the particle [50, 18]. Their center wavelength and width change as a function of size [47], smoothly for larger particles more dramatic for the very small ones.

Silver clusters, the electronic complexity of which lies between that of alkali clusters and gold and copper clusters, have been the object of numerous studies. Understanding their electronic properties and optical response remains an interesting challenge due to the close lying d-electrons, which quench the oscillator strengths by screening the s-electrons and get partially involved in the excitations. A recent paper [62] shows the center of the plasmon absorption (for small clusters the center of the absorption lines) as a function of silver cluster size. Large particles where the dielectric function is the same as for the extended solid, show a smooth behavior and are fairly well understood. Very small particles (up to 39 atoms) which have been measured on mass selected neutral clusters clearly do now follow the trend of a

monotonous redshift for increasing size but show shell closing and molecular like structures. The intermediate size regime (40 – 120 atoms) is not covered by measurements on size selected neutral clusters and that is the gap which is interesting to be filled.

In this Chapter, we present a series of optical absorption measurements on neutral, size selected (20 – 120 atoms) silver clusters embedded in a solid neon matrix at 6 K. These atom for atom precise optical spectra provide a unique way to investigate the evolution of the plasmon energy of these small clusters and successfully fills the gap in the intermediate size range of several tens of atoms [62].

4.1 Optical absorption spectra of Ag_n clusters ($n = 20, 35, 55, 58, 84, 92, 120$)

The optical absorption spectra in the UV-visible range of size selected neutral Ag_n clusters ($n = 20, 35, 55, 58, 84, 92, 120$) embedded in a solid neon matrix at 6 K are presented here. These spectra have been normalized by absorption intensity per atom, and the absorption energies have been blue shifted by 0.17 eV due to the matrix effects of neon solid [98].

4.1.1 Ag_{20}

Figure 4.1 shows the experimental results (red curve) of optical absorption spectrum of Ag_{20} . Using a multi-lorentzian fit, we have found 3 main absorption peaks at 3.85 eV (with amplitude of 1.10 a.u. and FWHM of 0.19 eV), 3.96 eV (with amplitude of 1.20 a.u. and FWHM of 0.17 eV), and 4.04 eV (with amplitude of 1.26 a.u. and FWHM of 0.24 eV) respectively.

4.1.2 Ag_{35}

Figure 4.2 shows the experimental results (red curve) of optical absorption spectrum of Ag_{35} . Using the multi-lorentzian fit, we have found 4 main absorption peaks at 3.87 eV (with amplitude of 2.37 a.u. and FWHM of 0.33 eV), at 4.00 eV (with amplitude of 0.96 a.u. and FWHM of 0.21 eV), at 4.11 eV (with amplitude of 1.50 a.u. and FWHM of 0.18 eV), and at 4.21 eV (with amplitude of 0.80 a.u. and FWHM of 0.19 eV).

4.1.3 Ag_{55}

Figure 4.3 shows the experimental results (red curve) of optical absorption spectrum of Ag_{55} . Using the multi-lorentzian fit, we have found 3 main absorption peaks at 3.77 eV (with amplitude of 0.12 a.u. and FWHM of 0.17 eV), at 4.04 eV (with amplitude of 1.56 a.u. and FWHM of 0.25 eV), and at 4.21 eV (with amplitude of 0.48 a.u. and FWHM of 0.20 eV).

4.1.4 Ag_{58}

Figure 4.4 shows the experimental results (red curve) of optical absorption spectrum of Ag_{58} . Using the multi-lorentzian fit, we have found 2 main absorption peaks at 3.81 eV (with amplitude of 0.59 a.u. and FWHM of 0.37 eV), and at 4.11 eV (with amplitude of 1.44 a.u. and FWHM of 0.32 eV).

4.1.5 Ag_{84}

Figure 4.5 shows the experimental results (red curve) of optical absorption spectrum of Ag_{84} . Using the multi-lorentzian fit, we have found 3 main absorption peaks at 3.79 eV (with amplitude of 2.32 a.u. and FWHM of 0.34 eV), at 3.93 eV (with amplitude of 1.73 a.u. and FWHM of 0.28 eV), and at 4.10 eV (with amplitude of 2.43 a.u. and FWHM of 0.31 eV).

4.1.6 Ag_{92}

Figure 4.6 shows the experimental results (red curve) of optical absorption spectrum of Ag_{92} . Using the multi-lorentzian fit, we have found 2 main absorption peaks at 3.79 eV (with amplitude of 0.07 a.u. and FWHM of 0.22 eV), and at 3.94 eV (with amplitude of 1.08 a.u. and FWHM of 0.28 eV).

4.1.7 Ag_{120}

Figure 4.7 shows the experimental results (red curve) of optical absorption spectrum of Ag_{120} . Using the multi-lorentzian fit, we have found 4 main absorption peaks at 3.61 eV (with amplitude of 0.20 a.u. and FWHM of 0.16 eV), at 3.74 eV (with amplitude of 0.25 a.u. and FWHM of 0.18 eV), at 3.86 eV (with amplitude of 0.28 a.u. and FWHM of 0.23 eV), and at 4.04 eV (with amplitude of 0.37 a.u. and FWHM of 0.42 eV).

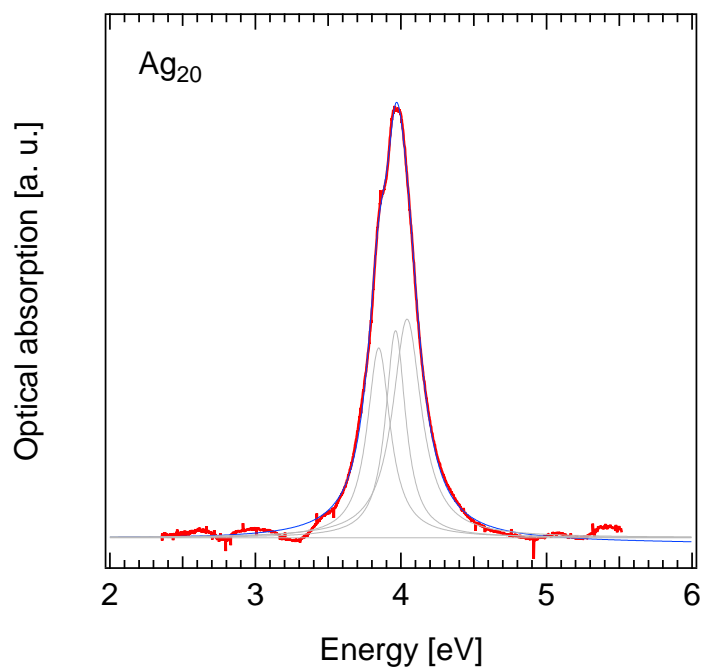


Figure 4.1 – Optical absorption of Ag_{20} , where the red curve represents the experimental result and the blue curve represents the multipeak fitting result by lorentzian lineshape (grey curve).

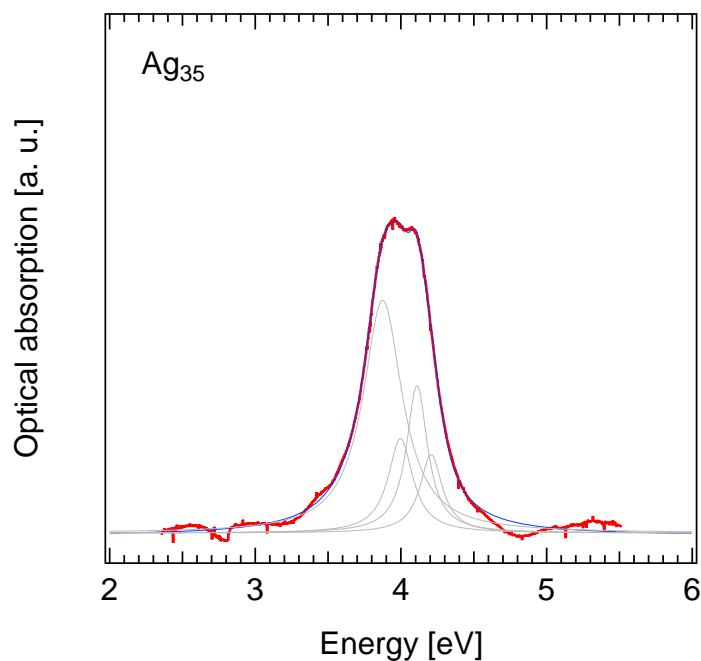


Figure 4.2 – Optical absorption of Ag_{35} , where the red curve represents the experimental result and the blue curve represents the multipeak fitting result by lorentzian lineshape (grey curve).

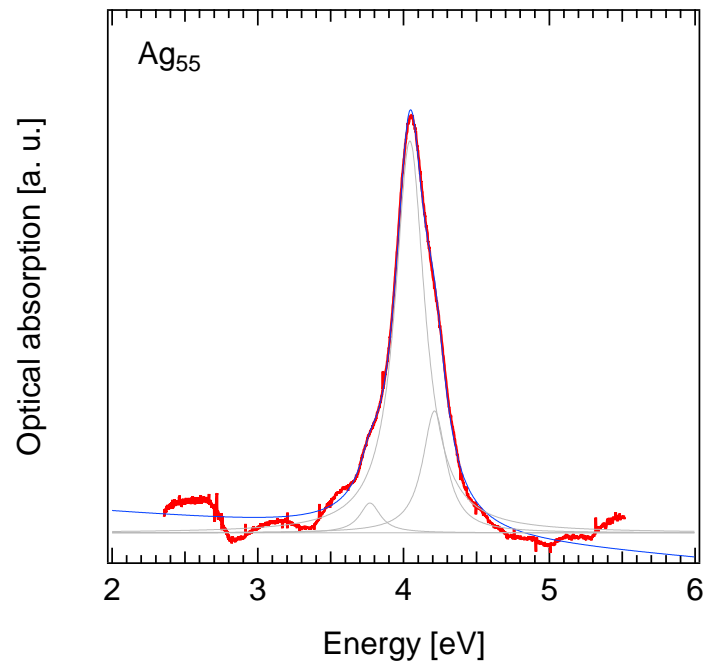


Figure 4.3 – Optical absorption of Ag_{55} , where the red curve represents the experimental result and the blue curve represents the multi-peak fitting result by Lorentzian lineshape (grey curve).

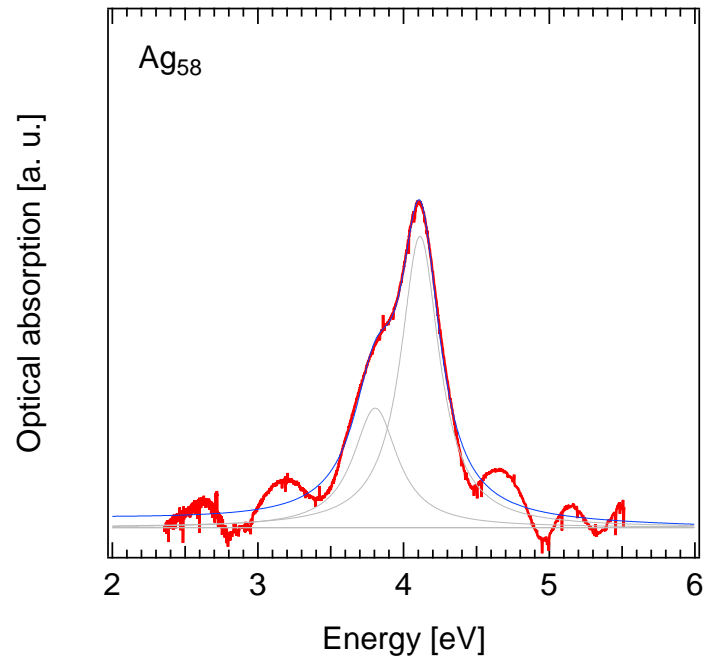


Figure 4.4 – Optical absorption of Ag_{58} , where the red curve represents the experimental result and the blue curve represents the multi-peak fitting result by Lorentzian lineshape (grey curve).

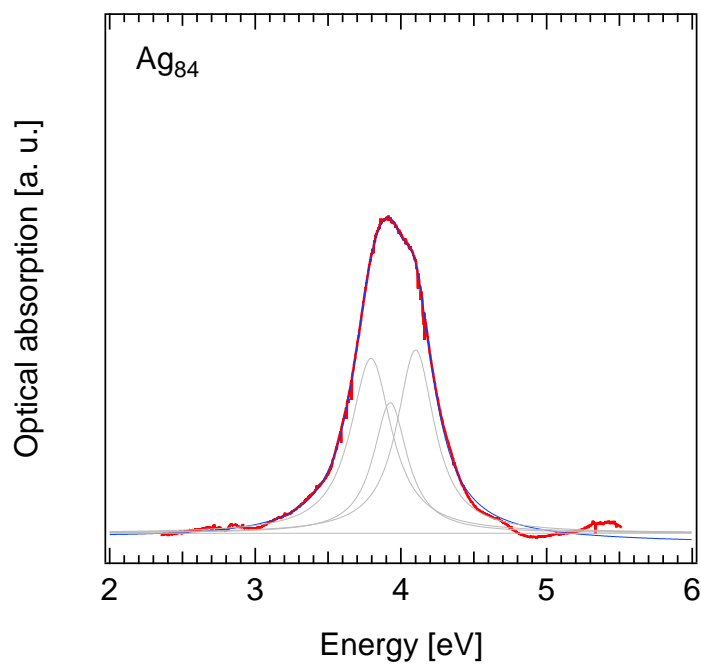


Figure 4.5 – Optical absorption of Ag_{84} , where the red curve represents the experimental result and the blue curve represents the multipeak fitting result by lorentzian lineshape (grey curve).

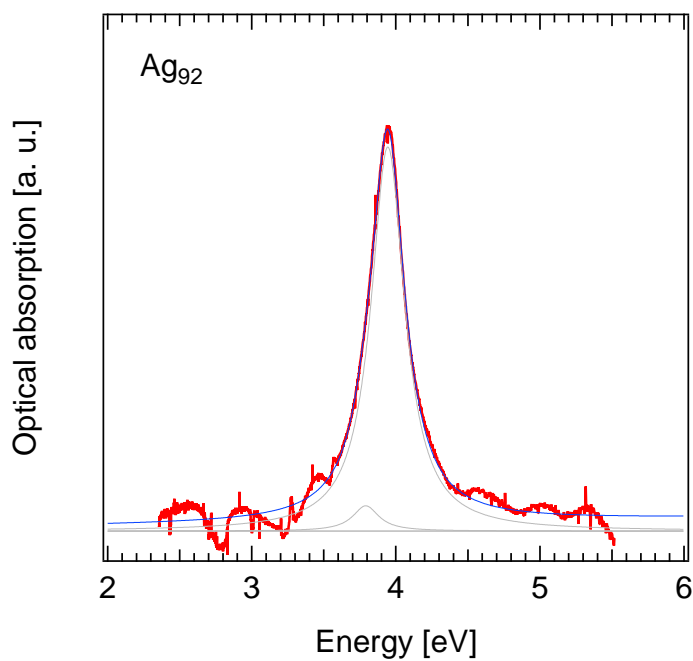


Figure 4.6 – Optical absorption of Ag_{92} , where the red curve represents the experimental result and the blue curve represents the multipeak fitting result by lorentzian lineshape (grey curve).

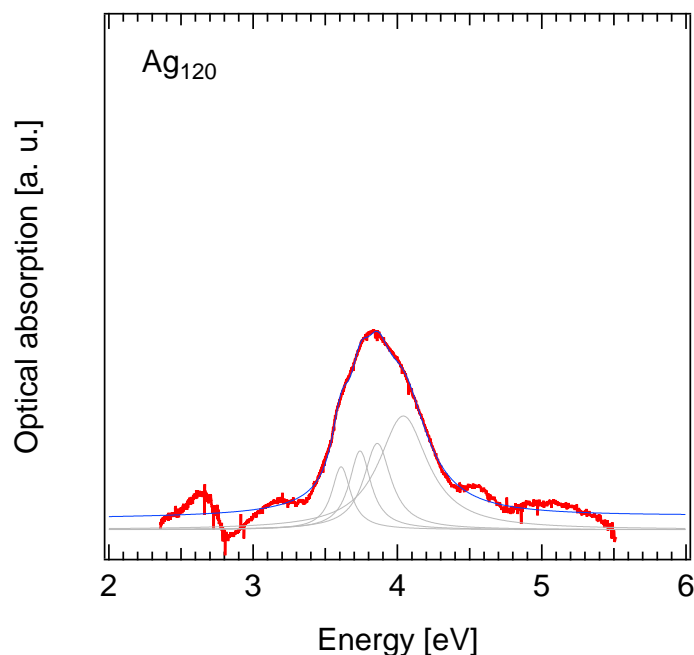


Figure 4.7 – Optical absorption of Ag_{120} , where the red curve represents the experimental result and the blue curve represents the multipeak fitting result by Lorentzian lineshape (grey curve).

4.2 Comparison to TDDFT calculations

As discussed before, TDDFT calculation is a very powerful tool to explore the electronic structures and optical properties of small clusters theoretically. For example, TDDFT calculations have been very successful to explain the optical spectra for small cluster with sizes up to $n = 9$ [20, 51]. It was found that only energetic close lying isomers coexist in a neon matrix while in all other cases only the ground-state was present. This manifests that our optical measurements are performed not only on monodispersed samples but even on isomeric clean samples.

Ag_{20} has been calculated by the Lyon group using different functionals [20, 103]. The most recent ones, using the CAM-B3LYP and LC-M06L functional, show excellent agreement with the experimental spectrum as shown in figure 4.8 for the latter one. In these calculations the groundstate structure has been calculated and found to be of D_s symmetry, different from the highly symmetric tetrahedral T_d structure like in Au_{20} [16]. The optical absorption spectrum calculated by Aikens et al. [18] shows a fairly similar absorption profile in a comparable energy range as seen in figure 4.9. However the highly symmetric tetrahedral structure is characterized by one strong electronic transition at around 4 eV. The experimental spectrum clearly is composed of multiple transitions (see table 4.1) which together account for the total

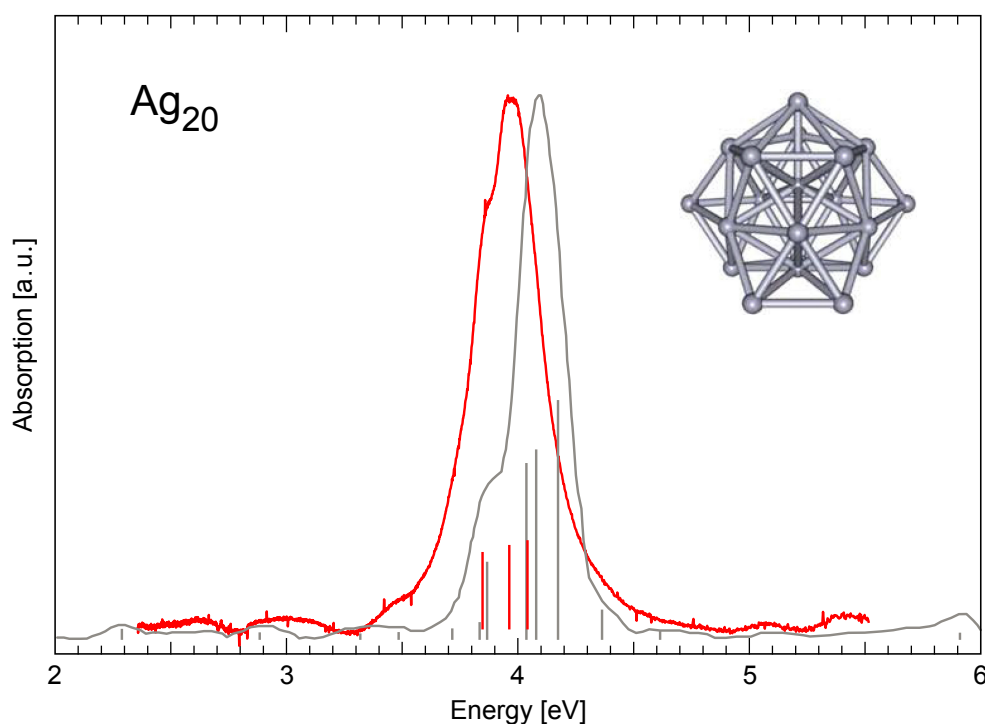


Figure 4.8 – Comparison of experimental measurements (red curve) to TDDFT calculation using LC-M06L/SDD model (grey curve [20]) of optical absorption on Ag_{20} cluster.

width of the absorption peak. It seems therefore plausible to adopt the calculated D_s symmetry as the lowest lying ground state.

Aikens et al. [18] have performed a comparative study over a large set of cluster sizes focussing on tetrahedral shell closings ($n = 20, 35, 84, 120$). It should be noted that the geometric structure in the calculations was not relaxed but the T_d structure imposed. In contrast to the experimental data where the oscillator strength clearly bunches around 4 eV with a very weak redshift to larger sizes, this shift is much more pronounced in the calculations. Furtheron the high symmetry leads to a plasmon width which is rather narrow and does not show an increase in the calculations, while the experimental spectra are broad compared to Ag_{55} and Ag_{92} which would indicate that these clusters clearly possess a higher symmetry correspond to subshell closings in the geometrical. A comparison of the calculations with the corresponding experimental data is given in figure 4.9. Their results showed that for the selected tetrahedral clusters, the plasmon width does not increase with decreasing cluster size. They claimed that this lack of sensitivity of plasmon width to cluster size is specific to tetrahedral clusters with filled shells, in which the low symmetry clusters give much broader spectra.

We have also compared our experimental result of optical absorption spectrum of Ag_{55} to the TDDFT calculation of Ag_{56}^+ by Aikens group [18]. Although owning the same number of free valence electrons according to jellium model (see section 2.3.2), two isoelectronic spectra show

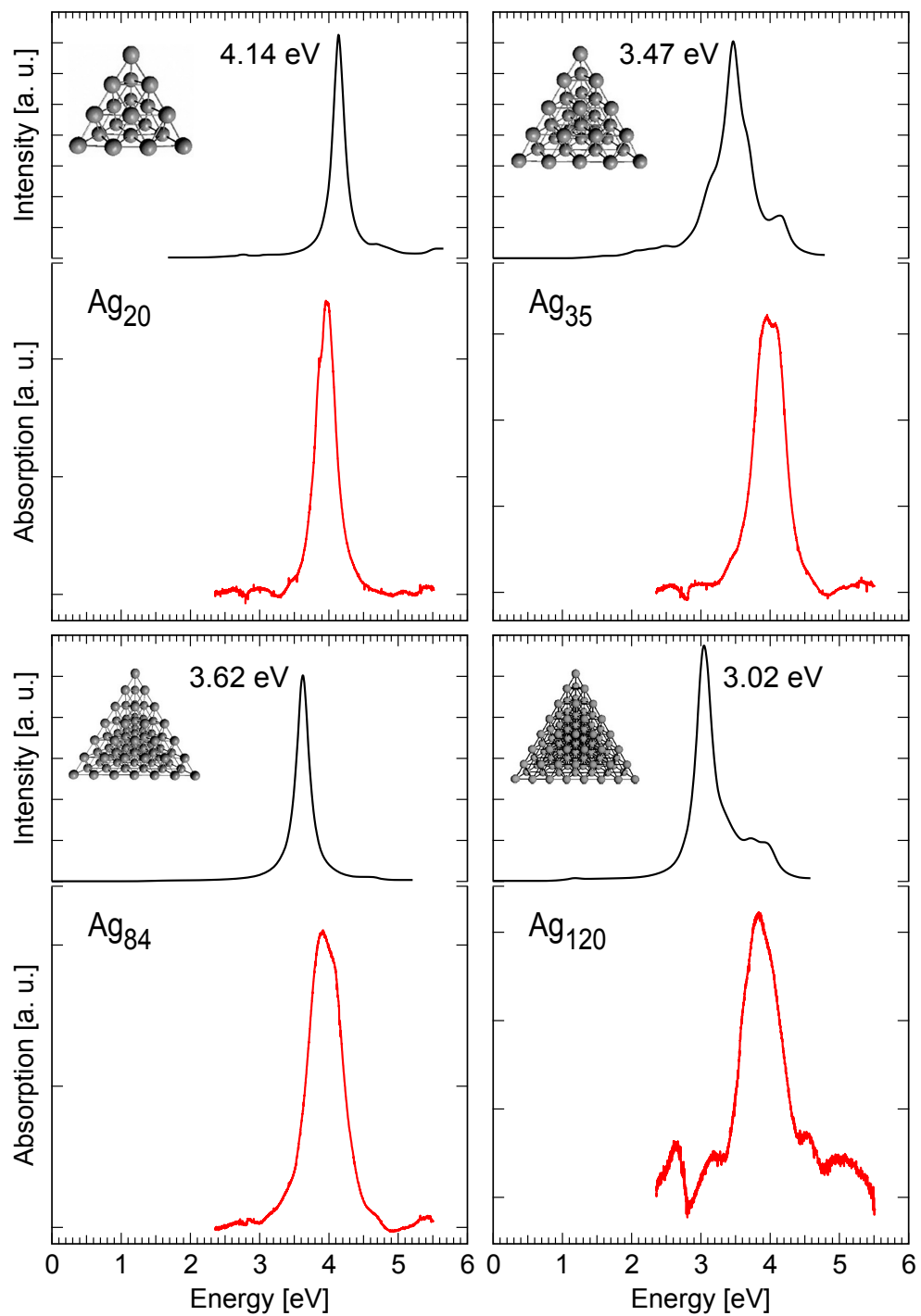


Figure 4.9 – Comparison of experimental measurements (red curve) to TDDFT calculation (grey curve [18]) of optical absorption on Ag_n ($n = 20, 35, 84, 120$) clusters.

completely different features. As shown in figure 4.10, Ag_{55} gives a single narrow absorption peak at about 4.0 eV with FWHM of only about 0.3 eV. But Ag_{56}^+ presents a much broader

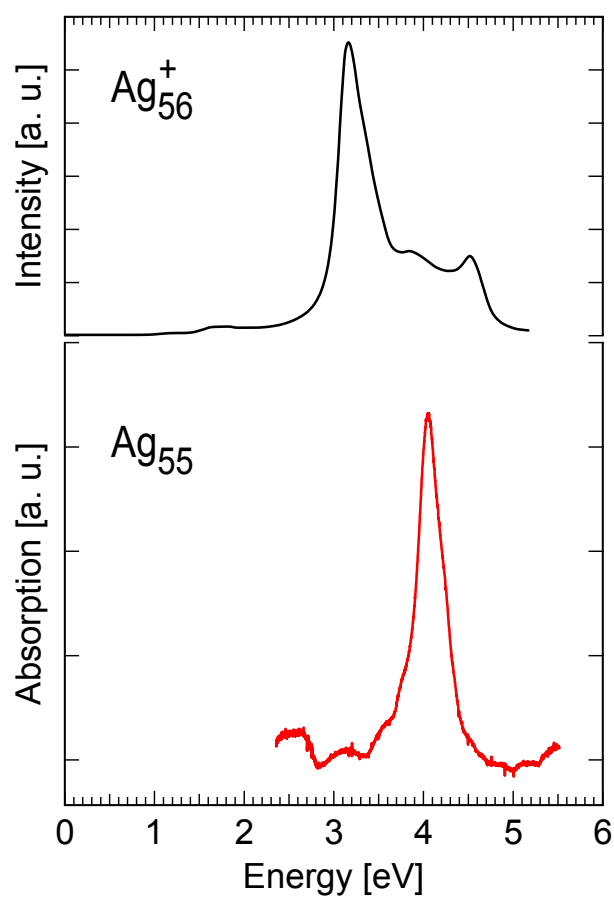


Figure 4.10 – Comparison of experimental measurements of optical absorption on Ag_{55} cluster (red curve) to TDDFT calculation (grey curve [18]) on Ag_{56}^+ .

absorption spectrum with two main peaks at about 3.2 eV and 4.7 eV . This manifests that the core ions of small metal clusters play an important role on the dielectric function which can be reflected by its optical response due to the intrinsic effect (see Section 2.3).

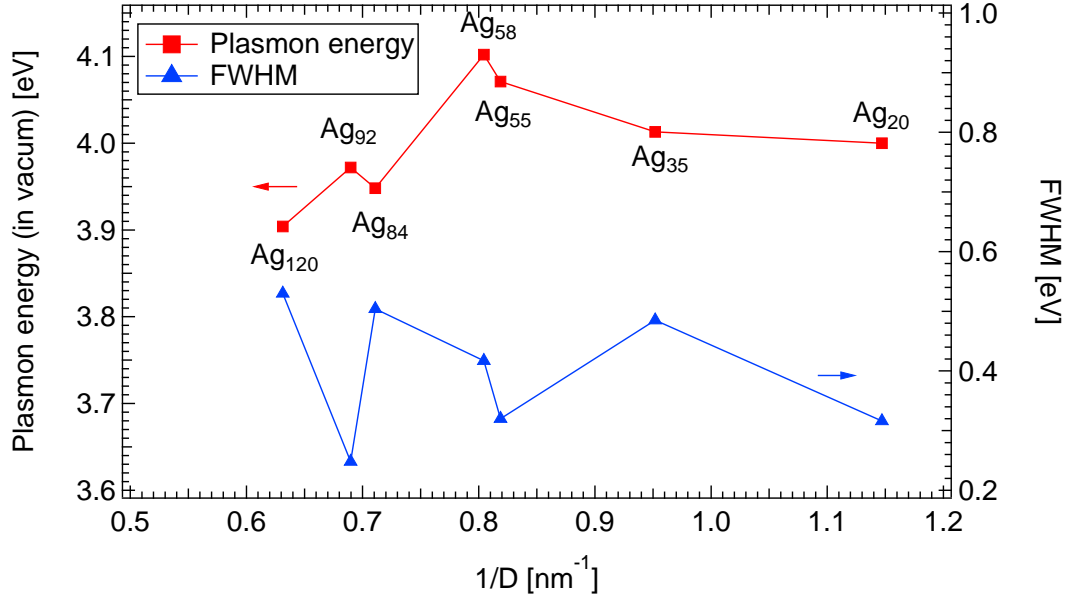


Figure 4.11 – Plasmon energy and width as a function of the inverse particle diameter of $1/D$ with cluster size from 20 to 120 atoms.

4.3 Plasmon energy of Ag_n clusters

Plasmon, as a quantum of plasma oscillation, is an oscillation of free electron density at the plasma frequency with respect to the fixed positive ions. Plasmon plays an important role in the optical properties of metals. For the small metal clusters, only the surface plasmon can be excited by light. The plasmon energy, that is the mean absorption energy, can be defined as [104]:

$$E_p = \hbar \cdot \langle \omega \rangle = \hbar \cdot \frac{\int_0^\infty \omega \cdot \sigma(\omega) d\omega}{\int_0^\infty \sigma(\omega) d\omega}. \quad (4.1)$$

where σ is the absorption cross section. Therefore, by using equation 4.1, we can obtain the plasmon energies of Ag_n clusters from the optical absorption spectra as shown in figure 4.1-4.7.

4.3.1 Plasmon energy and width with cluster size

Figure 4.11 shows the plasmon energy and width as a function of the inverse particle diameter of $1/D$ with cluster size from 20 to 120 atoms. The central absorption energies of these clusters are around 3.9 – 4.1 eV, which are typical plasmon energies for small silver clusters. Ag_{58} has the highest plasmon energy of 4.10 eV and Ag_{120} has the lowest plasmon energy of 3.90 eV. Besides, we can see that Ag_{20} , Ag_{55} , Ag_{92} show respectively narrow absorption widths (< 0.32

eV of FWHM), while Ag₃₅, Ag₅₈, Ag₈₄, Ag₁₂₀ show respectively wide absorption widths (> 0.42 eV of FWHM).

For small metal clusters, the plasmon energy reflects the resistance of conduction electrons of the cluster forced by the external electric field: higher the resistance is, higher the plasmon energy is. In addition, the width of plasmon reflects the geometrical symmetry of conduction electrons cloud of the cluster particle: more symmetrical the cluster particle is (e.g. a sphere shape of s electrons), a smaller width of plasmon it has. Interestingly, as shown in figure4.11, a relatively higher plasmon energy corresponds to a relatively smaller FWHM. This manifests that a cluster with a higher symmetrical electrons cloud has a higher resistance of conduction electrons to the external electric field.

4.3.2 Bridge the gap between atom and bulk

As we mentioned before, the intermediate size regime (40 – 120 atoms) of silver was not covered by measurements on size selected clusters. Now this gap has been filled. Figure4.12 shows the optical absorption spectra of silver from atom to bulk, with our size by size the measured absorption spectra of Ag_n ($n = 20, 35, 55, 58, 84, 92, 120$) clusters embedded in solid neon at 6 K. Spectra have been normalized to cluster density and to the number of atoms per cluster. The whole absorption spectrum has further on be blue shifted by 0.17 eV to account for the dielectric matrix shift [98]. This allows to compare the spectra to gas phase values. For comparison, we have calculated the bulk limit, i.e. the optical spectrum in the dipolar approximation using the dielectric function of bulk silver [105]. The experimental data are given in red. The blue line corresponds to a multi-lorentzian fit with variable energy, intensity and line-width. The relative positions and intensities are represented as grey bars. The data are summarized in table4.1, which list energy, intensity and line-width for a given transition.

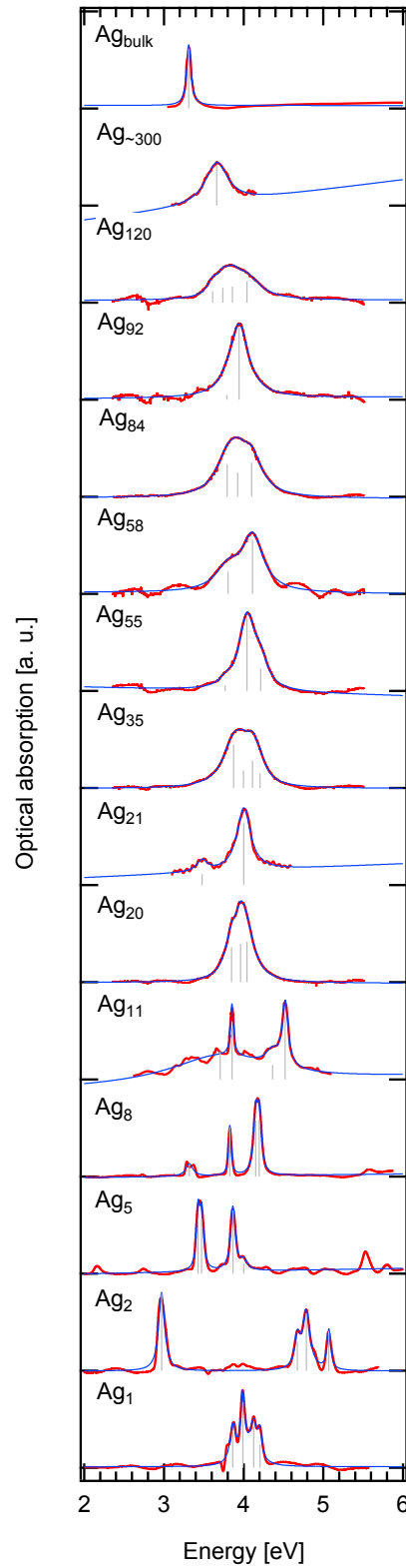


Figure 4.12 – Optical absorption of silver from atom to bulk. Ag_1 , Ag_2 , Ag_5 , Ag_8 [51]; Ag_{11} , Ag_{21} [106]; Ag_n ($n = 20, 35, 55, 58, 84, 92, 120$) (our results); Ag_{300} [107]; Ag_{bulk} [105].

Chapter 4. Result: Optical properties of silver clusters

Ag _n	Plasmon		Abs. peak 1			Abs. peak 2			Abs. peak 3			Abs. peak 4		
	En. (eV)	FWHM (eV)	En. (eV)	Int. (a.u.)	FWHM (eV)	En. (eV)	Int. (a.u.)	FWHM (eV)	En. (eV)	Int. (a.u.)	FWHM (eV)	En. (eV)	Int. (a.u.)	FWHM (eV)
•1	4.03	—	3.86	0.97	0.09	3.99	1.67	0.06	4.12	1.07	0.13	4.21	0.61	0.05
•2	—	—	2.97	2.71	0.09	4.67	1.01	0.08	4.79	1.99	0.11	5.07	1.37	0.05
•5	3.57	—	3.43	2.86	0.05	3.47	2.86	0.06	3.87	3.29	0.07	4.00	0.49	0.10
•8	4.10	—	3.32	0.65	0.11	3.83	2.56	0.04	4.15	2.91	0.06	4.20	2.97	0.06
*11	3.87	—	3.71	0.36	1.54	3.85	0.67	0.05	4.36	0.19	0.20	4.52	0.82	0.09
★20	4.00	0.316	3.85	1.10	0.19	3.96	1.20	0.17	4.04	1.26	0.24	—	—	—
*21	3.92	—	3.48	0.14	0.16	4.00	0.81	0.21	—	—	—	—	—	—
*35	4.01	0.485	3.87	2.37	0.33	4.00	0.96	0.21	4.11	1.50	0.18	4.21	0.80	0.19
*55	4.07	0.320	3.77	0.12	0.17	4.04	1.56	0.25	4.21	0.48	0.20	—	—	—
*58	4.10	0.417	3.81	0.59	0.37	4.11	1.44	0.32	—	—	—	—	—	—
*84	3.95	0.504	3.79	2.32	0.34	3.93	1.73	0.28	4.10	2.43	0.31	—	—	—
*92	3.97	0.248	3.79	0.07	0.22	3.94	1.08	0.28	—	—	—	—	—	—
*120	3.90	0.530	3.61	0.20	0.16	3.74	0.25	0.18	3.86	0.28	0.23	4.04	0.37	0.42
◦300	3.66	0.34	3.66	1.41	0.34	—	—	—	—	—	—	—	—	—
◊ bulk	3.31	0.07	3.31	0.63	0.07	—	—	—	—	—	—	—	—	—

Table 4.1 – Energies, intensities and widths of plasmons and transitions contributing to the absorption spectra. ★ figure4.1-4.7; • [51]; * [106]; ◦ [107]; ◊ [105].

Our experimental results of clusters with size range from 20 to 120 fill the gap in the size range of several tens of atoms. The central absorption energies of these clusters are around 4 eV, which is a typical plasmon energy for small free silver clusters. Besides, we can see that Ag₂₀, Ag₅₅, Ag₉₂ show narrow absorption widths (around 0.3 eV full width at half-maximum (FWHM)), while the absorption profile for Ag₃₅, Ag₅₈, Ag₈₄, Ag₁₂₀ is much wider (around 0.5 eV of FWHM). Moreover, clearly seen from figure4.12, by multi-lorentzian fit, Ag₂₁, Ag₅₈ and Ag₉₂ show two peaks, Ag₂₀, Ag₅₅ and Ag₈₄ show three peaks, and Ag₃₅ and Ag₁₂₀ show four peaks. Compared with the narrow peak of plasmon energy at about 3.3 eV for bulk silver on one hand, the silver clusters of Ag₂₀-Ag₁₂₀ show a higher and wider peak of plasmon energy. Compared with the spread multi-peaks of plasmon energy of very small clusters of Ag₁-Ag₁₁ on the other hand, the silver clusters of Ag₂₀-Ag₁₂₀ show a wide absorption peak formed by several very closed narrow peaks.

4.3.3 Sub-shell effect

An interesting question is the size dependence of the surface plasmon resonance energy which can be well defined by the single symmetric absorption peak for larger particles supposed to be spherical in shape. This situation is more complicated for smaller clusters whose shape deviates from the sphere with a splitting of the plasmon resonance in multiple peaks. A further complication arises from the perturbation of this resonance due to the dielectric influence of the substrate for supported clusters (inhomogenous dielectric environment) and embedded clusters (homogenous dielectric environment). Most measurements for larger clusters are, because of technical difficulties restricted to an ensemble of sizes which makes the attribution of an absorption profile to a specific size difficult. Exceptions are the very recent electron energy loss measurements on single Ag clusters supported on carbon grids from Scholl et al [62] and on silicon nitride by Raza et al.[72].

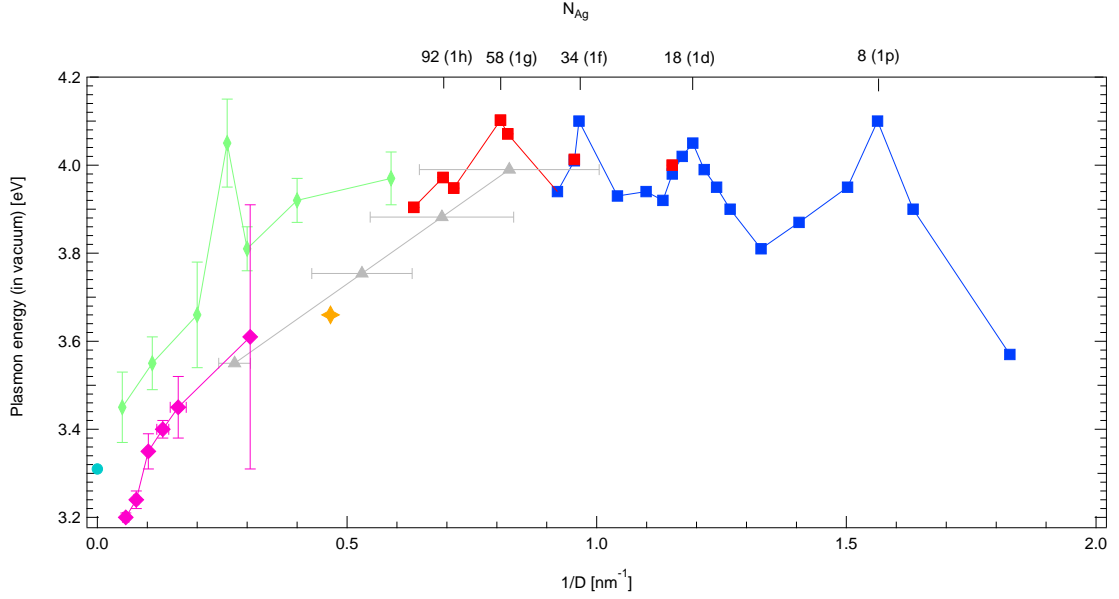


Figure 4.13 – Experimental results of plasmon energy of silver clusters response to the inverse cluster diameter of $1/D$. ■ [106]; ▲ [108]; ◆ [62]; ◆ [72]; ★ [107]; ● [105].

Figure 4.13 shows the experimental results of plasmon energy of silver clusters response to the cluster size. Here the plasmon energy is calculated by using equation 4.1 and is plotted against the inverse particle diameter of $1/D$. The data of ref [62, 106, 108] have been scaled to obtain the resonance energies in vacuum. Please note, here we use 0.25 eV instead of 0.29 eV to blue shift the plasmon energy from argon matrix to vacuum according to the matrix effect [98]. Our present results on Ne matrices coincide perfectly with the older data from plasmon energies in Ar [106]. This shows that matrix effects [98] will only weakly influence the optical absorption of embedded clusters except for the red shift.

Moreover, we have noticed that our results show a higher plasmon energy of about 0.03 eV, compared with the results of ref [108]. Note that the silver clusters used in ref [108] are not mass-selected, having a wide size distribution with constant $1/D$. This means the average plasmon energy of a cluster group with a certain size distribution of $1/D$ is lower than that of its center size of $1/D$, which indicates the plasmon energy of silver cluster has an open-down parabola relationship with inverse particle diameter, as shown in figure 4.14. This conclusion is completely consistent with our theoretical calculation based on ref [109].

Clearly seen from the figure 4.13, the plasmon energy shows an oscillated characteristic response to the cluster size. Interestingly, we can find that the silver clusters with atom numbers of 8, 18, 34, 58, 92 show a localized maximum value of plasmon energy. According to the well-known shell model as shown in figure 2.8, these numbers correspond to the fully filled states of $1p$, $1d$, $1f$, $1g$ and $1h$. This manifests that the clusters with fully filled states have

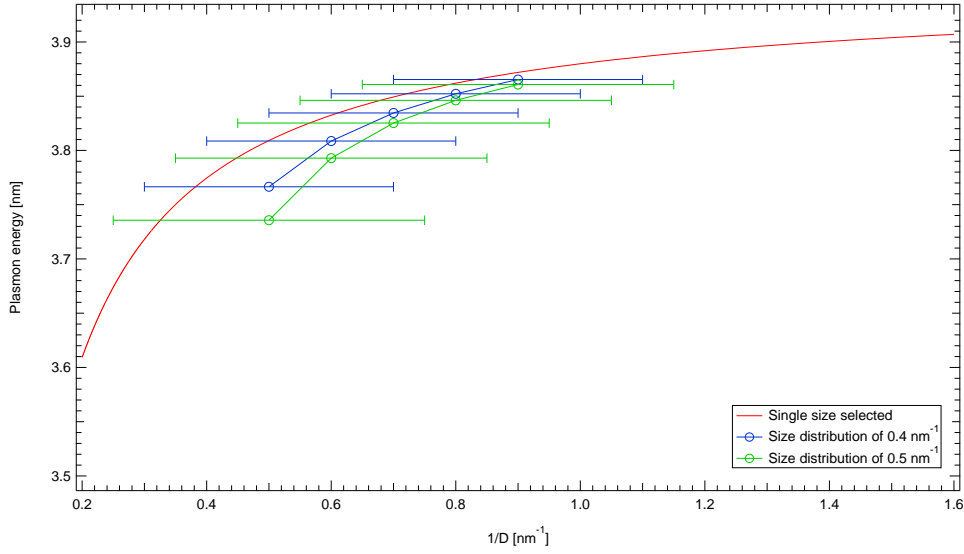


Figure 4.14 – Calculations of mean plasmon energy as a function of the mean inverse cluster diameter with different cluster size distribution.

higher plasmon energies than those of clusters with partial filled states, showing a sub-shell effect.

4.4 Polarizability of Ag clusters

As discussed in Section 2.2.2, for a small metal particle, the positive charged core in the clusters is assumed to be immobile and the negative charged conduction electrons are allowed to move under the external field. Thus a displacement between the positive charges and the negative ones occurs if a metal cluster is placed in an external field. The polarizability of clusters can be defined and calculated from the absorption spectra as [104]:

$$\alpha = \frac{Ne^2}{\epsilon_0 m_e} \cdot \left\langle \frac{1}{\omega^2} \right\rangle = \frac{Ne^2}{\epsilon_0 m_e} \cdot \frac{\int_0^\infty \frac{1}{\omega^2} \cdot \sigma(\omega) d\omega}{\int_0^\infty \sigma(\omega) d\omega}. \quad (4.2)$$

Therefore, by using equation 4.2, we can obtain the polarizability of Ag_n clusters from the optical absorption spectra as shown in figure 4.1-4.7.

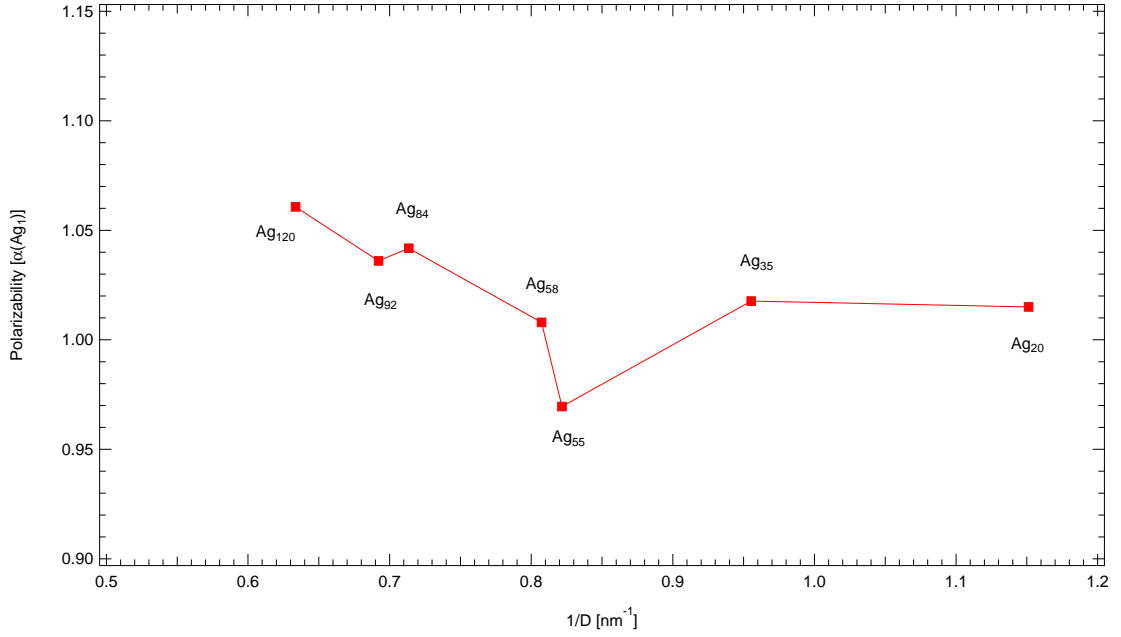


Figure 4.15 – Experimental results of polarizability of silver clusters of Ag_n ($n = 20, 35, 55, 58, 84, 92, 120$) as a function of the inverse cluster diameter.

4.4.1 Polarizability with cluster size

Figure 4.15 shows our experimental results of polarizability of silver clusters of Ag_n ($n = 20, 35, 55, 58, 84, 92, 120$). Here the polarizability is calculated by using equation 4.2. Polarizabilities in the range of 0.97 – 1.07 are found. We can see from the figure that Ag_{55} and Ag_{92} show localized minimum of polarizability. Compared with figure 4.11, as expected, we can find that a higher plasmon energy results in a lower polarizability. This is because the cluster with a higher plasmon energy is more stiff, which indicates a smaller displacement under external field.

4.4.2 Comparison with theoretical model

Figure 4.16 shows theoretical calculation of shape of clusters with different cluster size using harmonic spheroidal model according to equation 2.41 and table 2.4 based on Section 2.3.3. Please note that, by comparison, figure 2.11 gives the cluster shapes using unharmonic spheroidal model with harmonic oscillator of $u = 0.04$ [63].

Based on Section 2.3.3 and using equation 2.43, 2.44 and 2.47, the polarizability of clusters can be calculated from the cluster shape. Figure 4.17 shows our experimental and theoretical results of polarizability of silver clusters as a function of inverse diameter of cluster size of $1/D$. We can see that the unharmonic model shows a better agreement with the experimental result than the harmonic model.

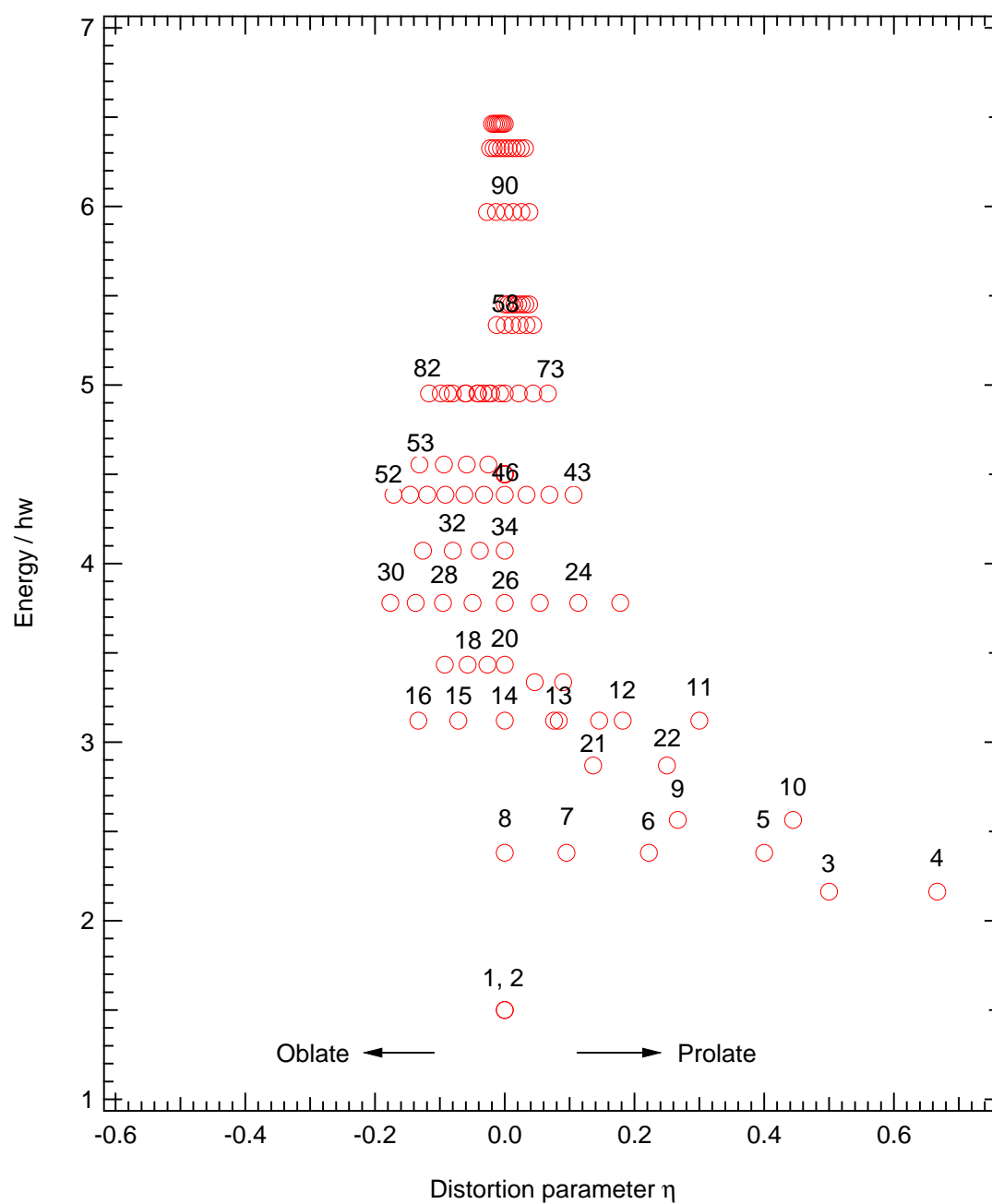


Figure 4.16 – Theoretical calculation of shape of small clusters using harmonic spheroidal model.

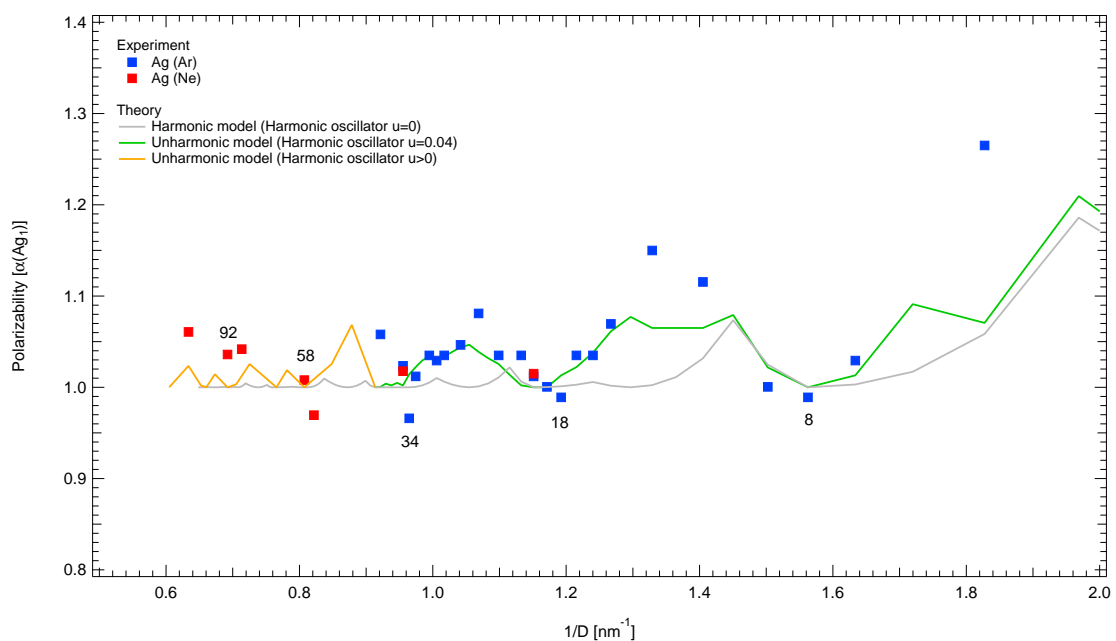


Figure 4.17 – Experimental and theoretical results of polarizability of silver clusters as a function of inverse diameter of cluster size. ■[106]; –[63]; –[110].

5 Result: Optical properties of gold clusters

Gold clusters and nanoparticles are in the center of an intense research effort and have attracted considerable interest due to their potential technological applications such as nanoelectronics by single molecule electronics with gold nanowires [111]. Gold nanoparticles also exhibit novel optical, electronic, and magnetic properties such as chiroptical activity in glutathione-passivated clusters [112]. In addition, small gold clusters have been found to be good catalysts for the oxidation of small molecules such as CO and H₂ [113, 114].

From a fundamental point of view, clusters of noble metal elements are of particular interest because they form the natural bridge between clusters made from free electron like metal elements and transition-metal clusters, and thus constitute an interesting ground for the testing of theoretical approaches. Gold clusters are much more complex systems compared to silver clusters as discussed in Chapter 4. Having a smaller s-d separation and showing strong relativistic effects, the optical spectra of Au are of larger complexity. Until now, reliable optical spectra of the neutrals are still not available except for the recent optical absorption measurements on small gold clusters Au_{*m*} (*m* = 1 – 5, 7 – 9) [53].

The important features of Au_{*n*}, particularly relevant to nanophotonic applications, are their dielectric and optical properties. Experimentally, the optical absorption spectra of small Au clusters were obtained using a variety of techniques such as noble-gas matrix spectroscopy, resonant two-photon ionization spectroscopy, photodepletion spectroscopy, and photodissociation spectroscopy [115, 116, 52, 117]. For the neutral Au clusters, the experimental study of the optical absorption was limited only up to Au₉ so far [53].

Recently, the studies of fluorescence on Au nano-particles have shown great potential and attracted much interest due to its wide applications in a variety of disciplines, such as the switchable fluorescence in Au nanoparticle/DNA rotaxane hybrid nanostructures [118], the enhanced fluorescence from dye molecules by Au nanoparticles [119], the nonbleaching fluorescence of gold nanoparticles for the application in cancer cell imaging [120], the multiphoton fluorescence in human insulin–Au nanodots [121], the molecular fluorescence by Au@SiO₂ core-shell nanoparticles [122], and the label-free fluorescence on protein-protected

Au clusters [123]. Understanding the fluorescence origin is of critical importance for the applications of bioimaging and photonics.

Au clusters with a few atoms usually show fluorescence in the blue or green region with a very broad bandwidth [124]. Despite considerable theoretical efforts on Au clusters [125, 126, 127, 128, 129], the optical properties of Au clusters have been rarely reported experimentally and the fundamental understanding remains far from being completed. Furthermore, their electronic and geometric structures remain unclear due to the complexity and lack of experimental evidence. Experimentally, fluorescence studies of Au clusters are mostly based on ligand-protected or protein-encapsulated Au nanoparticles [130, 131, 132, 123], and optical measurements on pure neutral Au clusters don't exist for cluster sizes above 9 atoms. Actually, fluorescence measurements on size-selected neutral Au clusters have never been performed before except for the gold atom and dimer [133].

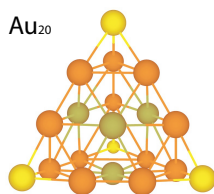
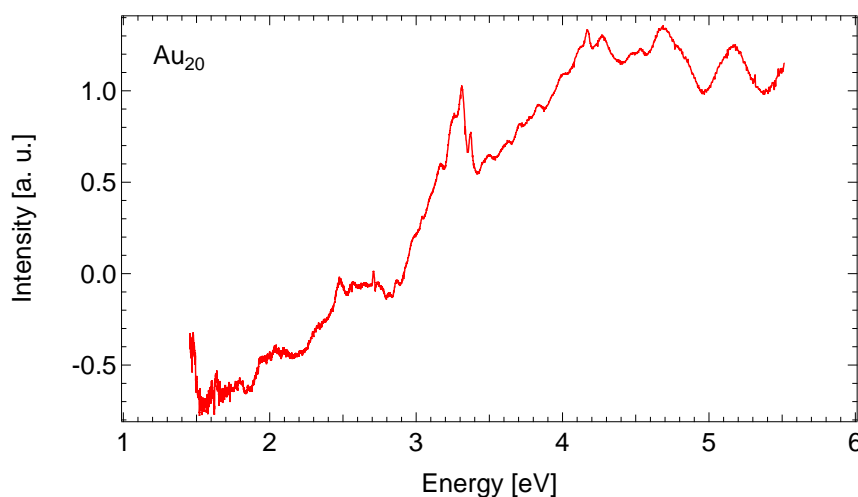
In this Chapter, we present optical absorption and fluorescence measurements on neutral, size selected Au_m ($m = 19, 20, 21$) gold clusters embedded in a solid neon matrix at 6 K. These optical spectra provide a unique way to investigate their electronic and geometric structures.

5.1 Optical response of Au_{20}

5.1.1 Absorption spectrum of Au_{20}

Recent photoelectron spectroscopy and relativistic density functional calculations have suggested that Au_{20} has a tetrahedral geometry (see figure 5.1) similar to a fragment of bulk face-centered cubic (fcc) gold [16]. This similarity suggests the use of this cluster as a model of the bulk surface where each of the four faces of the tetrahedron represents a (111) surface. Besides, the apex and edge atoms have different coordination numbers and may also provide useful sites for catalysis and other applications. Hence, acquiring a high resolution reliable optical absorption of size-selected Au_{20} clusters can give further confirmation for this structure and, in addition, permit to test TDDFT calculations that report the optical properties.

Figure 5.2 shows the experimental result of the optical absorption on mass selected Au_{20} clusters embedded in Ne matrix at 6 K. Here the optical spectrum has been blue-shifted by 0.17 eV in order to compensate the energy offset on the electronic states caused by the Ne matrix [52]. Different from the absorption spectra of Ag_n ($n = 20 - 120$) clusters mentioned in Section 4.1 that all show a plasmon-like peak at about 4.0 eV, the Au_{20} cluster shows a continuous rich-structured absorption spectrum from 2.0 eV to 5.5 eV. The strongest absorption peak is presented at 3.31 eV with several other main peaks at 2.48, 3.37, 4.16, 4.28, 4.69 and 5.17 eV. Moreover, the blue (higher energy) part has a larger optical absorption than the red (lower energy) part, which is consistent with the feature of optical absorption of a bulk gold [105].

Figure 5.1 – Tetrahedral structure of Au₂₀ [16].Figure 5.2 – Measurement of optical absorption on mass selected Au₂₀ clusters embedded in Ne matrix at 6 K.

5.1.2 Fluorescence spectrum of Au₂₀

Figure 5.3 shows the spectra of fluorescence on Au₂₀ excited by lasers at wavelengths of 266 nm, 375 nm, 473 nm and 532 nm respectively. We can clearly see that, despite of the change of the incident light wavelength, Au₂₀ cluster presents a very strong fluorescence at 739.2 nm (equaling to 1.85 eV considering matrix effect) with a bandwidth (FWHM) of about 35 nm (equaling to 0.08 eV). Note that, for excitations at 266 and 375 nm, a group of continuous fluorescence peaks is presented closed to the excitations, as shown in figure 5.3(a) and (b). Interestingly, the fluorescence peak of Au₂₀ at 1.85 eV is extremely close to that of 1.83 eV on Au₂. But the bandwidth of Au₂₀ of 0.08 eV is much smaller than that of 0.2 eV on Au₂ [133].

Compared to the fluorescence measured on other Au cluster systems like ligand-protected or protein-encapsulated Au nanoparticles, our result on pure Au₂₀ clusters shows a much smaller bandwidth. For example, Wu et al. showed a fluorescence on Au₂₅(SCH₂CH₂Ph)₁₈[−] system at 750 nm with 150 nm bandwidth [131]. Xu et al. found the fluorescence on Au nanoclusters/BSA (bovine serum albumin) systems from 650 to 700 nm with 100 nm bandwidth [130]. Wen et al. gave a fluorescence on Au₂₅/BSA systems at 690 nm with 120 nm bandwidth [132]. Liu et

al. presented a fluorescence on human insulin–Au nano-dots at about 700 nm with 150 nm bandwidth [121]. We think that the small bandwidth of the fluorescence peak of Au₂₀ may be due to the different cluster size or its ligand-free property.

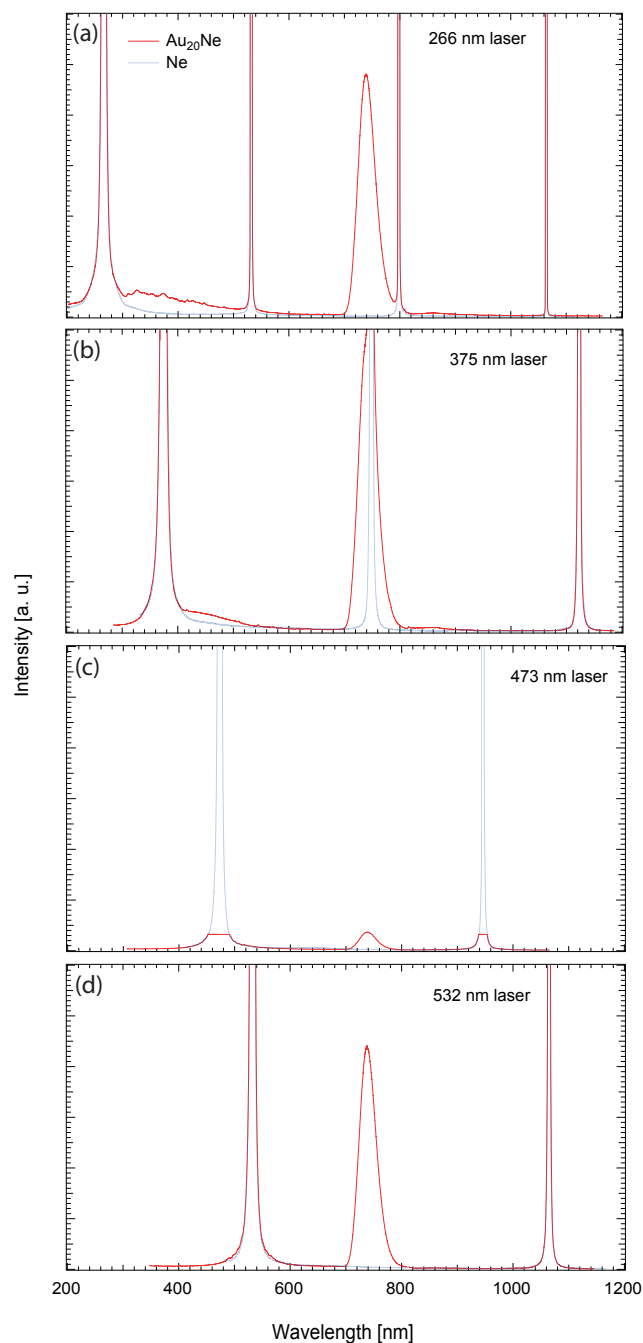


Figure 5.3 – Measurement of optical fluorescence on mass selected Au₂₀ clusters excited by a 266 nm, 375 nm, 473 nm and 532 nm respectively.

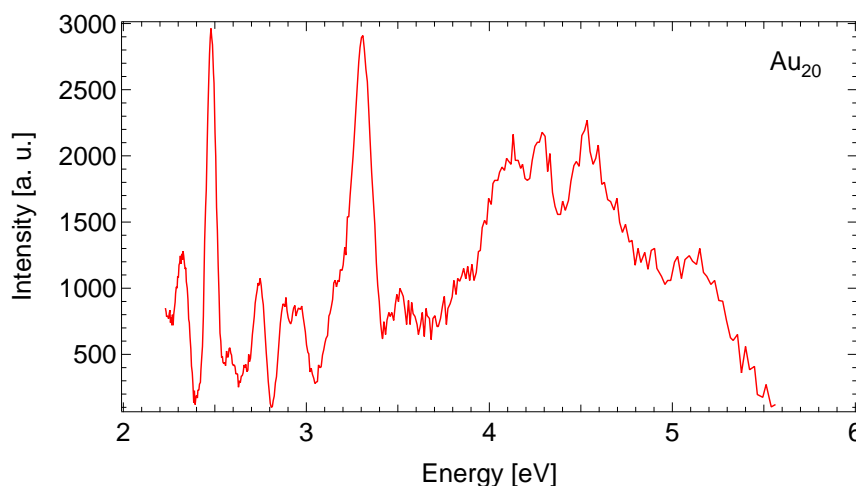


Figure 5.4 – Measurement of optical excitation on mass selected Au₂₀ clusters by measuring the intensity of fluorescence at 739.2 nm as a function of incoming photon energy.

5.1.3 Excitation spectrum of Au₂₀

Based on the fluorescence observation found at 739.2 nm, the excitation measurement is then performed by changing the incident light wavelength. Figure 5.4 shows the experimental result of excitation spectra on Au₂₀. The strongest peaks are presented at 2.48 and 3.31 eV with several main peaks at 2.33, 4.16, 4.28, 4.53 eV. Compared with the absorption spectrum shown in figure 5.2, the excitation spectrum provides a higher resolution on transition peaks. It's worth mentioning that the lack of the peaks in the excitation spectrum compared to the absorption spectrum is due to either the dark tunnels of relaxation of electrons without fluorescence after absorption, or the other fluorescence tunnels (not the 739.2 nm one) at different wavelengths as shown in figure 5.3(a) between 266 and 532 nm, or the surface plasmon. Please note, the peaks of the excitation spectrum cannot be the surface plasmon.

5.1.4 Conclusion of optical response of Au₂₀

Now we summarize the optical response of Au₂₀. As shown in figure 5.5 and 5.6, the absorption, fluorescence, and excitation spectra show consistent transition peaks. We have listed all the transition peaks in table 5.1. Four strongest main peaks at $b = 2.48$ eV, $k = 3.31$ eV, $p = 4.16$ eV and $q = 4.28$ eV can be clearly seen from the table.

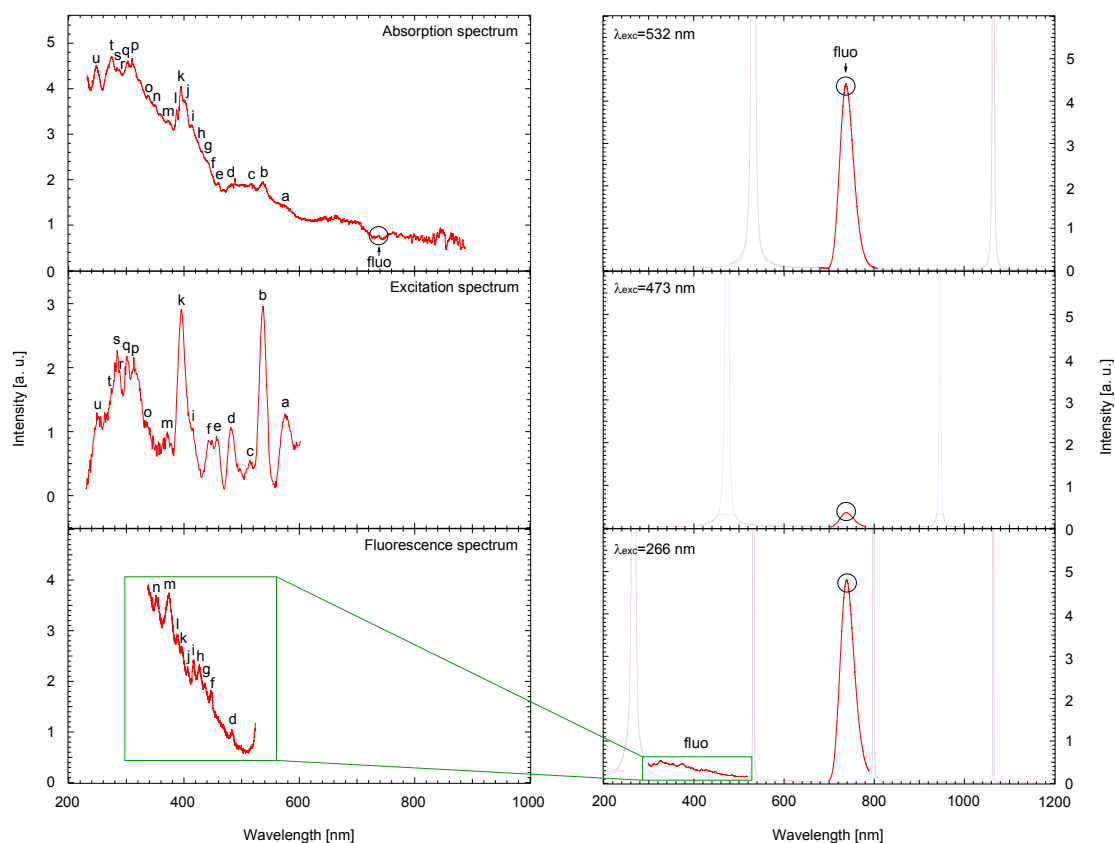


Figure 5.5 – Comparison of optical absorption, fluorescence and excitation spectra of Au_{20} in wavelength.

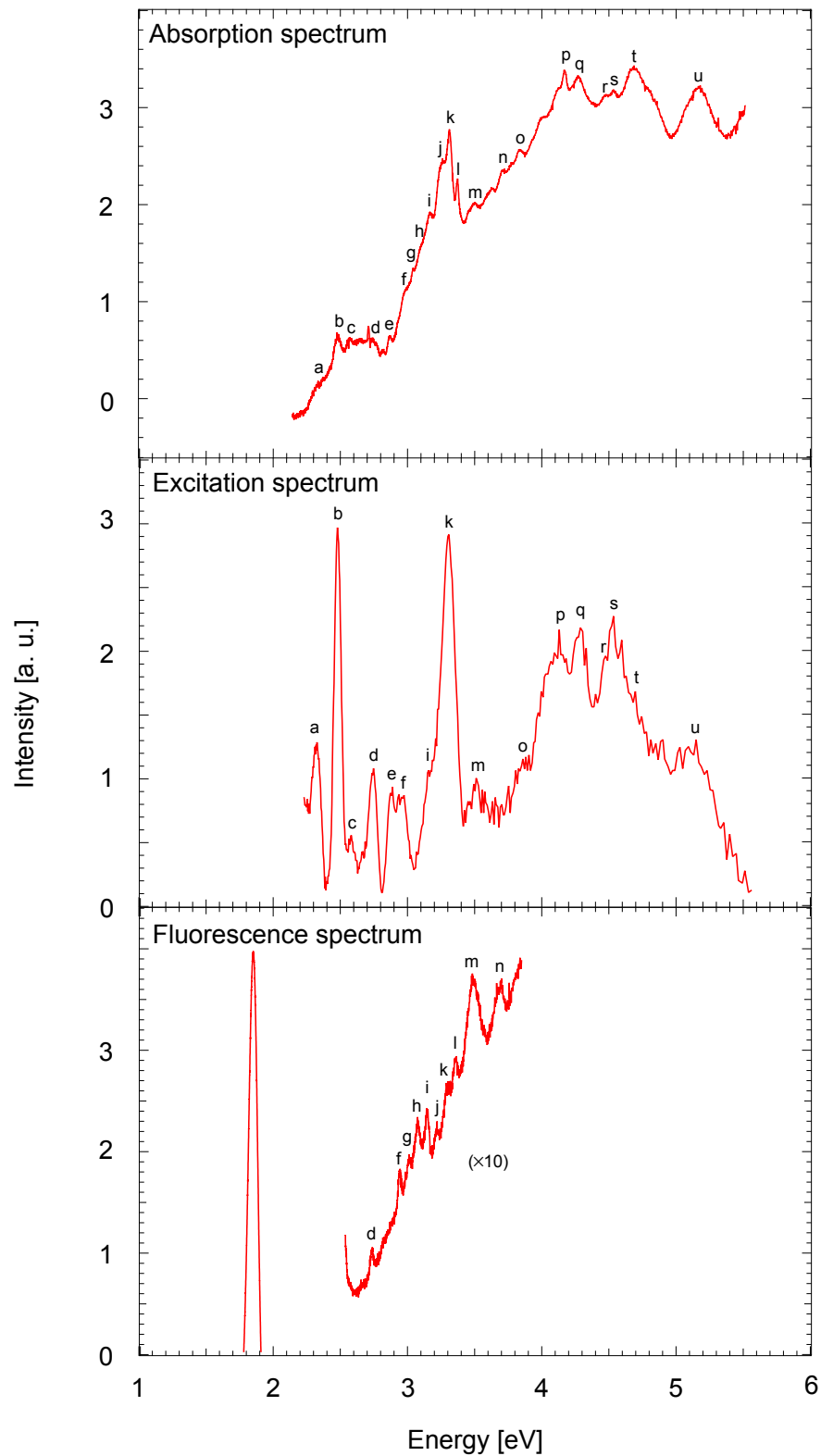


Figure 5.6 – Comparison of optical absorption, fluorescence and excitation spectra of Au₂₀ in energy.

Chapter 5. Result: Optical properties of gold clusters

Peaks	Energy (eV)	Wavelength (nm)	Absorption	Excitation	Fluorescence
fluo	1.85	739.2			S
a	2.33	574.1	W	S	
b	2.48	536.8	S	S	
c	2.58	514.5	W	W	
d	2.75	480.6	W	S	W
e	2.88	457.6	W	W	
f	2.95	446.0	W	W	W
g	3.02	435.1	W		W
h	3.08	426.1	W		S
i	3.15	416.1	W	W	S
j	3.23	405.2	W		W
k	3.31	394.9	S	S	W
l	3.37	387.5	S		W
m	3.51	371.3	W	W	S
n	3.71	350.3	W		S
o	3.86	336.0	W	W	
p	4.16	310.8	S	S	
q	4.28	301.7	S	S	
r	4.48	287.7	W	W	
s	4.53	284.4	W	S	
t	4.69	274.3	S	W	
u	5.17	248.0	S	W	

Table 5.1 – Comparison of transitions peaks of optical absorption, fluorescence and excitation on Au₂₀. Here 'S' represents strong peak and 'W' represents weak peak.

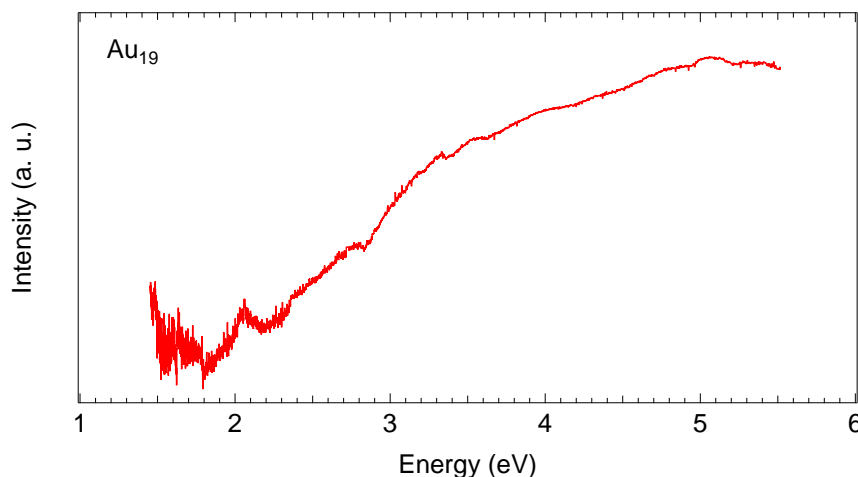


Figure 5.7 – Measurement of optical absorption on mass selected Au₁₉ clusters embedded in Ne matrix at 6 K.

5.2 Optical response of Au₁₉

5.2.1 Absorption spectrum of Au₁₉

It is interesting to look into Au clusters with one atom size above and one below 20 to see the close shell effect according to the shell model as discussed in Section 2.3.3. Therefore, we have also performed the optical measurements on Au₁₉ and Au₂₁. Figure 5.7 shows the optical absorption spectrum on mass selected Au₁₉ embedded in solid Ne at 6 K. As discussed before, here a blue shift of 0.17 eV has also been applied due to the matrix effect of Ne. We found that the absorption spectrum presents continuous transition peaks from 2.0 eV to 5.5 eV, and the absorption increases with the increase of photon energy, the characteristics of which are similar to those of Au₂₀. But different from the rich-structured absorption spectrum of Au₂₀, Au₁₉ here presents a poor-structured spectrum. The strongest absorption peak is shown at 3.33 eV with several main peaks at 2.39, 2.77, 3.54, and 5.08 eV.

5.2.2 Fluorescence spectrum of Au₁₉

Figure 5.8 shows the spectra of fluorescence on Au₁₉ excited by the lasers with wavelengths of 473, 532 and 635 nm. We can see that Au₁₉ has a strong fluorescence peak at 737 nm (equaling to 1.85 eV) with a bandwidth of 34 nm (equaling to 0.08 eV). Interestingly, this is exactly the same as that of Au₂₀. But clearly seen from figure 5.8, Au₁₉ has additional fluorescence peaks depending on the excitation light wavelength. For the incident 473 nm laser, Au₁₉ shows a small additional peak at 689 nm (equaling to 1.97 eV) with a bandwidth of 12 nm (equaling to 0.03 eV). For the incident 532 nm laser, Au₁₉ shows a large additional peak at 650 nm (equaling to 2.08 eV) with a bandwidth of 110 nm (equaling to 0.33 eV). For the incident 635 nm laser,

Au₁₉ shows a small additional peak at 713 nm (equaling to 1.91 eV) with a bandwidth of about 20 nm (equaling to 0.05 eV).

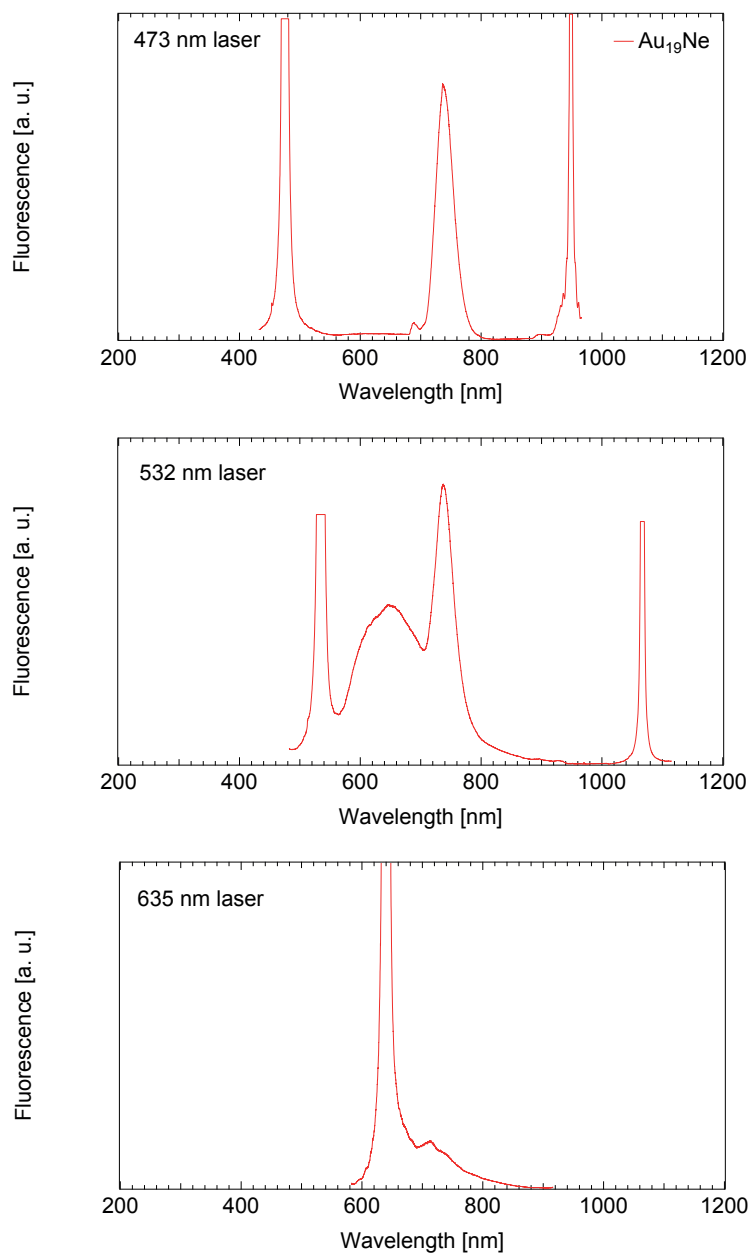


Figure 5.8 – Measurement of optical fluorescence on mass selected Au₁₉ clusters excited by a 473 nm, 532 nm and 635 nm respectively.

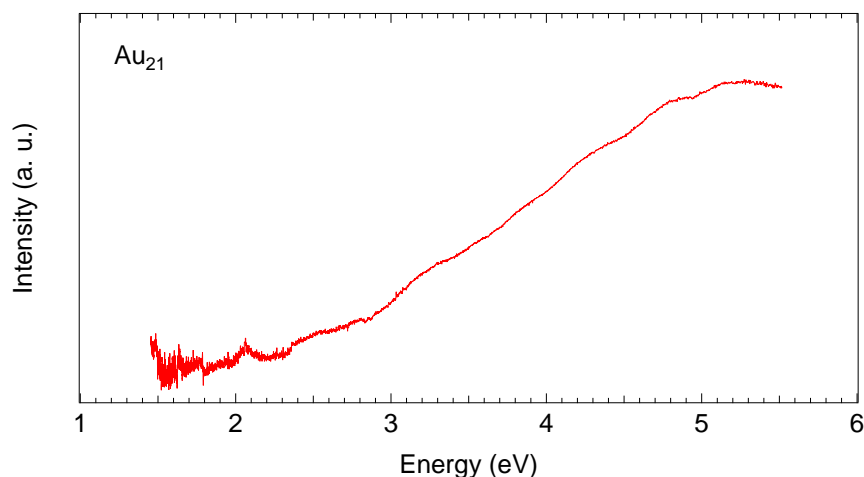


Figure 5.9 – Measurement of optical absorption on mass selected Au₂₁ clusters embedded in Ne matrix at 6 K.

5.3 Optical response of Au₂₁

5.3.1 Absorption spectrum of Au₂₁

Optical measurements on Au₂₁ have also been performed. Figure 5.9 shows the spectrum of optical absorption on Au₂₁ again blue shifted by 0.17 eV. Similarly to Au₁₉ and Au₂₀, the spectrum of Au₂₁ presents continuous absorption peaks from 2.0 eV to 5.5 eV, increasing with the increase of photon energy. Similar to Au₁₉, Au₂₁ also presents a poor-structured spectrum. But different from Au₁₉ and Au₂₀, there is no obvious main absorption peak in Au₂₁.

5.3.2 Fluorescence spectrum of Au₂₁

Figure 5.10 shows the spectra of fluorescence on Au₂₁ excited by the lasers with wavelengths of 473, 532 and 635 nm. We can see that, for excitations at 473 and 532 nm, Au₂₁ presents a strong fluorescence peak at 660 nm (equaling to 2.05 eV) with a bandwidth of 150 nm (0.43 eV). In addition, a small adjacent fluorescence peak at 730 nm (equaling to 1.87 eV) is also obscurely immersed inside the main peak of 660 nm because of the wide bandwidth. But for the excitation at 635 nm, the main peak is quenched and only the small peak of 730 nm is shown. This is because the excitation position is too close to the fluorescence position.

Most important, given that all three Au_m ($m = 19, 20, 21$) clusters show strong fluorescence centered at around 1.85 eV (see Sections 5.1.2, 5.2.2 and 5.3.2), comparing the fluorescence results of our ligand-free Au clusters to those of the ligand-protected Au clusters as discussed in Section 5.1.2 clearly proves that the fluorescence comes from the Au cluster itself and is only weakly influenced by the ligands.

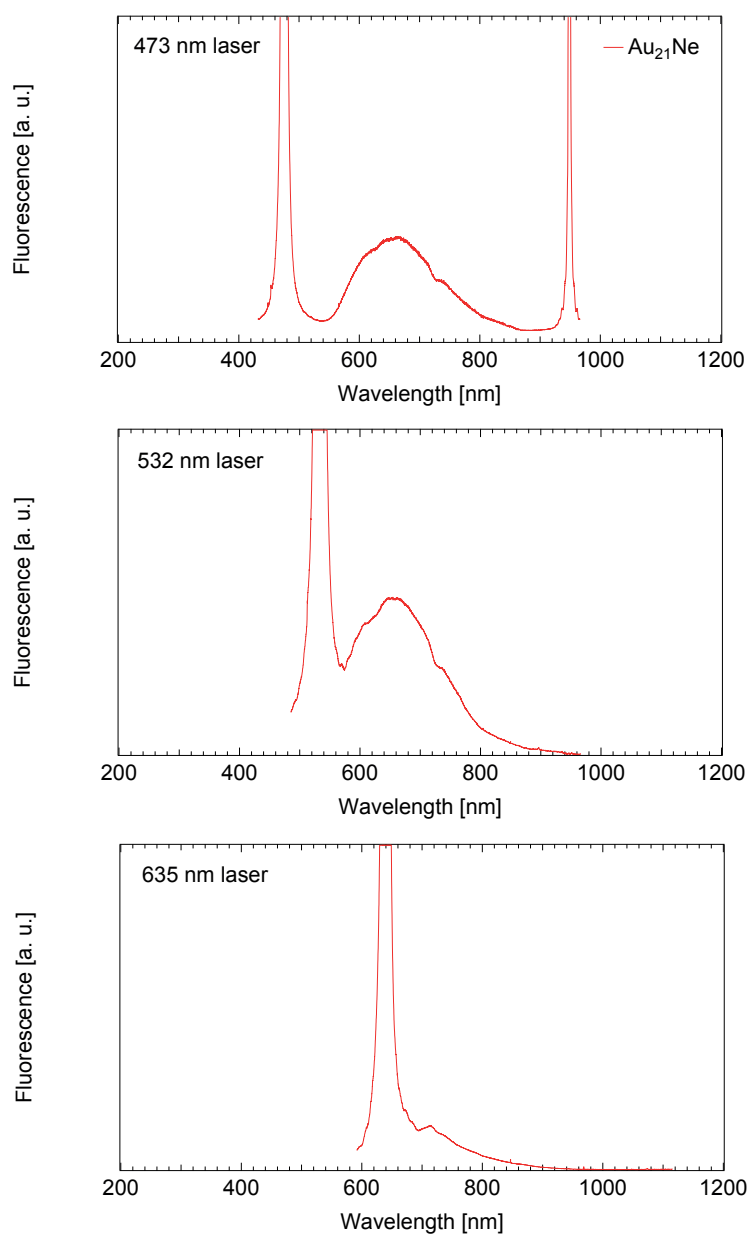


Figure 5.10 – Measurement of optical fluorescence on mass selected Au_{21} clusters excited by a 473 nm, 532 nm and 635 nm respectively.

5.4 Comparison to TDDFT calculations

Theoretically, there have been few studies on the dielectric and optical properties of small and medium sized Au clusters. Among the issues considered were the size dependence and anisotropy of the static dipole polarizabilities [134, 135, 136] and the features of the absorption and vibration spectra [137, 138]. Most of these studies were performed within the framework of density functional theory (DFT) and time-dependent DFT (TDDFT), and some using quantum chemistry techniques such as coupled cluster and configuration interaction methods. All the theoretical explorations for the absorption spectra of Au_n clusters have so far focused on a single size or a set of clusters in a narrow size range. Wang et al. [139], Itkin and Zaitsevskii [140], and Wang and Ziegler [141] computed the low-energy excitations of Au_2 . The infrared vibronic absorption spectrum of Au_3 was investigated by Guo et al. [137]. For Au_6 , Omary et al. [142] computed the absorption spectrum of a three-dimensional (bicapped tetrahedron of D_{2h} symmetry) isomer, while Rao et al. [143] investigated the spectrum of three low-lying isomers. In a combined experimental and theoretical study, absorption spectra for gold cluster anions complexed with one Xe atom, Au_n^-Xe , were measured and computed for the $n=7-11$ size range. Lecoultre et al. has reported the optical absorption measurements as well as TDDFT calculations on small gold clusters Au_n ($n = 1 - 5, 7 - 9$) [53].

While there was no experimental data available for the absorption spectrum of the tetrahedral Au_{20} cluster before, several groups have recently reported its computed spectrum within TDDFT, such as Wu et al. [144], Xie et al. [145], Aikens et al. [138], and Idrobo et al. [127]. Figure 5.11 shows the comparison of our experimental Au_{20} optical absorption spectrum on Au_{20} cluster to the TDDFT computational calculations mentioned above. Our experiment is in good agreement with those of Idrobo's calculations, except for a blue shift of about 0.3 – 0.4 eV. The computed values of Idrobo et al. are also in good agreement with those of Aikens et al., other than a 0.1 – 0.2 eV energy shift toward red. The computations of Wu et al. has given the similar spectra but shifted to blue by 0.3 – 0.4 eV compared to that of Aikens' result. Xie et al. found two absorption peaks at 2.74 and 1.93 eV which are in good agreement with the corresponding values of 1.86 and 2.78 eV of Idrobo's result.

We have also compared our experimental excitation spectrum with the TDDFT calculations of absorption result by Anak et al. [20]. As obviously seen in figure 5.12, our result shows a very good consistency with the calculation except for a –0.2 eV shift. Many of the transition peaks in table 5.1 are also presented in the spectrum of TDDFT calculation, such as b, k, m, o, p, r and u.

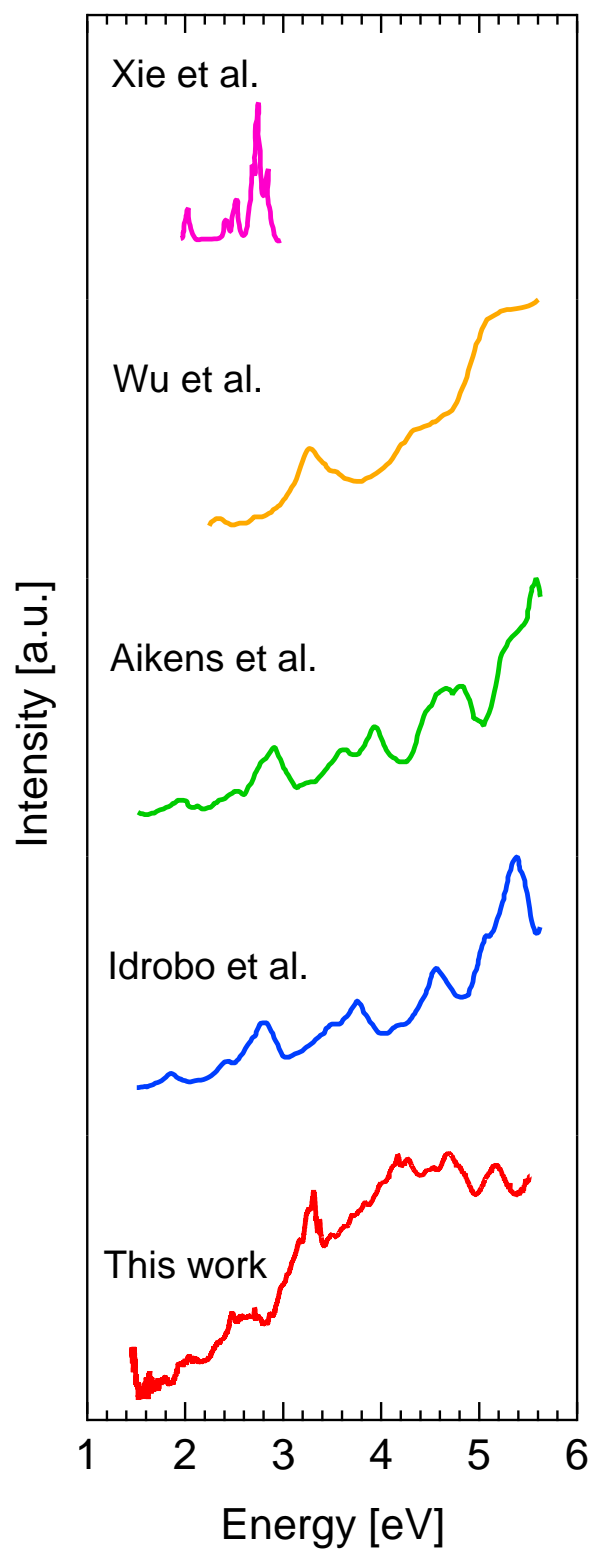


Figure 5.11 – Comparison of our experimental result to TDDFT calculations of optical absorption on Au₂₀. Idrobo et al. [127], Aikens et al. [138], Wu et al.[144], and Xie et al. [145].

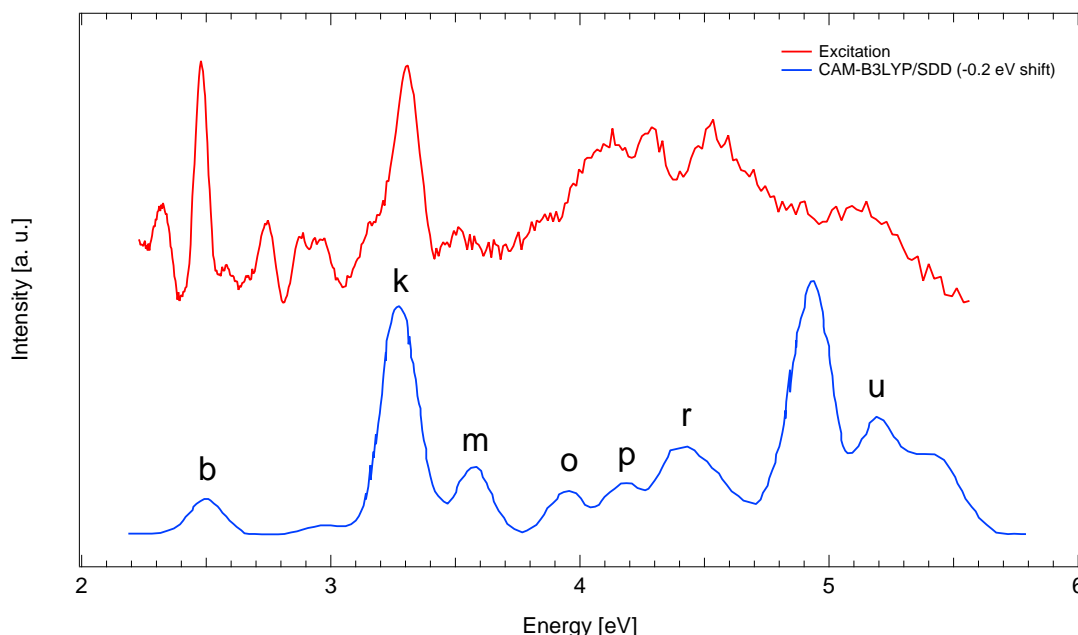


Figure 5.12 – Comparison of our experimental result to TDDFT calculation by Anak et al. [20] of optical absorption on Au_{20} .

5.5 Transition of optical response of gold from atom to bulk

Figure 5.13 shows the optical absorption spectra of gold from atom to bulk, with our measured absorption spectra of Au_n ($n = 19, 20, 21$) clusters embedded in solid neon at 6 K. The whole absorption spectrum has been blue shifted by 0.17 eV to account for the dielectric matrix shift [98]. This allows to compare the spectra to gas phase values. For comparison, we have calculated the bulk limit, i.e. the optical spectrum in the dipolar approximation using the dielectric function of bulk gold [105].

We can see from figure 5.13 that, for very small gold clusters of Au_n ($n = 1, 2, 3, 4$), the spectra present several molecular like transitions between 2.5 and 5.5 eV. For small gold clusters of Au_n ($n = 5, 7, 8, 9$), the spectra show many more transition peaks. The intermediate-sized gold clusters of Au_n ($n = 19, 20, 21$), as discussed above, exhibit continuous absorption spectra from 2.0 to 5.5 eV that change from unstructured to multipeak and back to unstructured for single atom size increments. This may be attributed to the close-shell effect. Finally, for bulk gold, a smooth absorption spectrum exhibits a plasmon peak at about 2.5 eV. Through figure 5.13, we can see the evolution from molecular like single electron transitions in atom into collective type transitions (surface plasmon) in bulk, where Au_{20} interestingly shows both types of transitions. Please note, Au_{20} with an absorption peak profile around 2.5 eV is also shown, which suggests the existence of the surface plasmon if compared to the bulk gold.

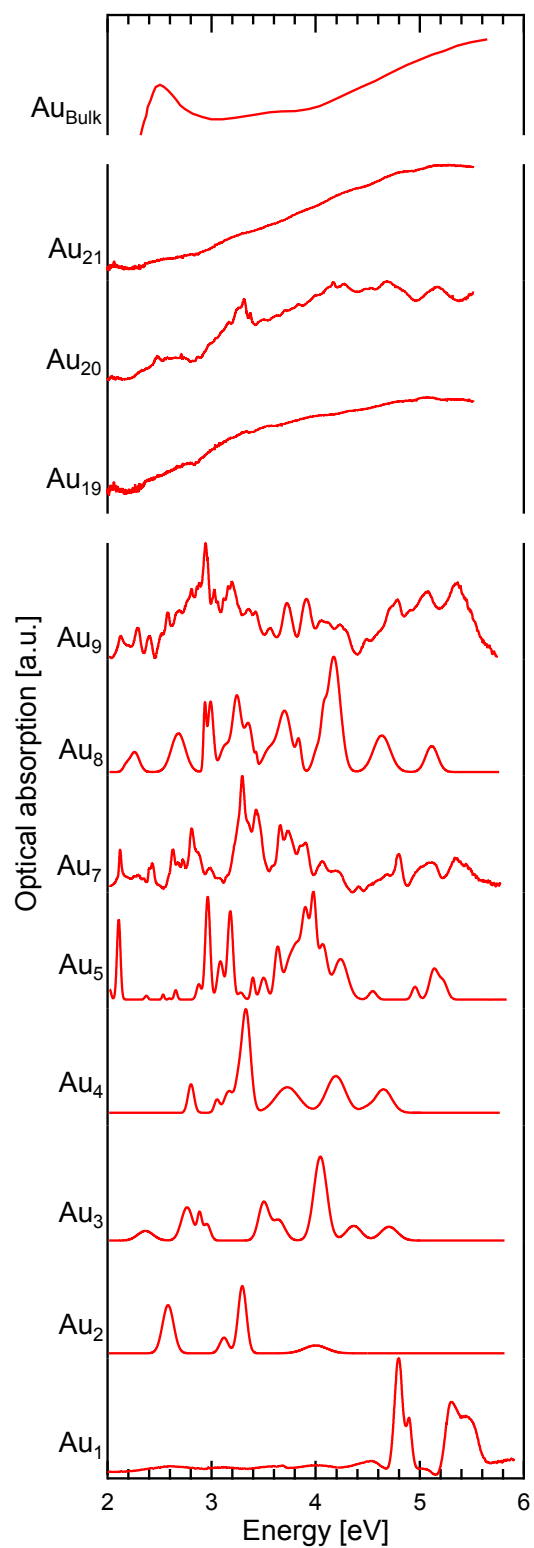


Figure 5.13 – Optical absorption spectra of gold from atom to bulk. Au_m ($m=1-5, 7-9$) [53]; Au_{bulk} [105].

6 Result: Optical properties of silver-pyridine clusters

Detecting single molecules with high sensitivity and molecular specificity is of great scientific and practical interest in many fields such as chemistry, biology, medicine, pharmacology, and environmental science [146]. Surface-enhanced Raman scattering (SERS) is a useful technique resulting in strongly increased Raman signals from molecules which have been attached to nanometer sized metallic structures. Although the ordinary Raman effect is extremely weak (characterized by cross sections of 10^{-30} cm² per molecule), a dramatic signal enhancement may occur if the analyte molecule is adsorbed to metal particles of subwavelength dimensions [147]. Raman cross sections as large as 10^{-15} cm² have been found which makes single molecule detection possible when adsorbed on silver nanoparticles [58]. The amplification of the electrostatic field in the surface plasmon excitation of silver plays an important role in SERS.

SERS has been discovered already more than 40 years ago [56, 57], but a complete understanding has not yet been achieved. It is generally agreed that more than one effect contributes to the observed large effective SERS cross section. The enhancement mechanisms are roughly divided into electromagnetic and chemical effects. Of course, the two mechanisms are not mutually exclusive but work together in concert to produce the overall SERS effect. It's a combination of the very high local electromagnetic fields at the junction of the molecule and the nanoparticle (electromagnetic enhancement) and a chemical enhancement due to the interactions (most likely charge transfer processes) between the two constituents.

The SERS was successfully employed by Kneipp et al. 20 years ago, who have observed extremely large Raman cross sections on the order of 10^{-17} to 10^{-16} cm² per molecule in SERS experiments using near-infrared (NIR) excitation for dyes adsorbed on colloidal silver [148]. More recently it was shown by Peyser-Capadona et al. [149] that small (2 – 8 atom) Ag clusters encapsulated in a peptide or dendrimer scaffold can produce comparable enhancement factors. In this size regime the classical description, where the strongly enhanced local field near the nanoparticle surface is caused by the surface plasmon excitation is not longer valid, since molecular type electronic excitations are dominant. These results have renewed an effort of understanding the Raman enhancement at the molecular level.

Theoretical calculations predicted large enhancement factors for molecules like pyridine (Py) attached to small silver clusters [59, 60, 61]. Zhao et al. have calculated in the TDDFT scheme the surface enhancement of the Raman cross section for pyridine in contact with a single Ag₂₀ nanocluster [59]. Enhancement factors of 10⁵ at best have been found. Jensen et al. have presented a TDDFT study of the size-dependence of the absorption and Raman scattering properties of pyridine interacting with small silver nanoclusters Ag_n ($n = 2 - 8, 20$) [60]. They found that both the absorption and Raman properties depend strongly on cluster size and adsorption site. The total enhancements for the complexes are between 10³ and 10⁴ and the strongest enhancement is found for the Ag₂-Py complex.

Giving the importance of SERS with small metal clusters for applications as well as a fundamental understanding of the underlying processes, it is highly desirable to obtain experimental data on size-selected neutral cluster molecule complexes. Freezing the Ag_aPy_b complexes in Ne matrices should provide an ideal system to measure Raman cross sections for a well-defined cluster size and environment. Based on this system, optical absorption, fluorescence and Raman spectroscopy should allow to test the theoretical predictions and thereby make a first step to the detailed understanding of the enhancement effect.

As mentioned in Section 3.5, silver-pyridine compounds are fabricated in a conical octupole by combining pyridine molecules injected from the reservoir and silver clusters produced from the cluster source due to high pressure and strong collision. The silver-pyridine compounds are then mass selected by a quadrupole as shown in figure 3.21, and co-deposited with Ne rare gas under low temperature of 6 K, forming a solid matrix.

In this Chapter, we will present the experimental results of optical measurements of absorption, fluorescence, and Raman scattering on size-selected silver-pyridine compounds of Ag_aPy_b ($a = 1, 3; b = 1, 2$).

6.1 Optical response of Ag₁Py₁

6.1.1 Absorption of Ag₁Py₁

Figure 6.1 (red curve) shows the experimental result of absorption spectrum on size-selected Ag₁Py₁ clusters embedded in solid neon. Four main peaks at 3.93, 4.06, 4.20 and 4.56 eV and six small peaks at 2.06, 2.55, 3.19, 3.40, 4.27 and 4.39 eV are found. As discussed before, here the spectrum has been blue shifted by 0.17 eV in order to compensate the energy offset caused by the matrix. Please note, all the following optical spectra in this Chapter will be shifted by this amount in order to be representative for gas phase species.

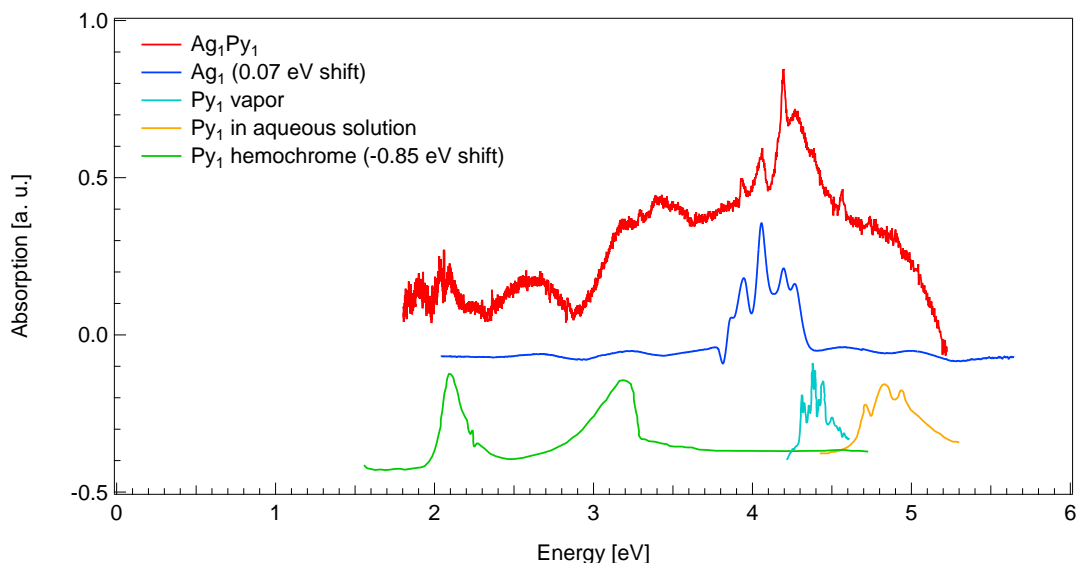


Figure 6.1 – Comparison of optical absorption spectrum of Ag_1Py_1 to that of pure Ag_1 and pure Py_1 . Here Ag_1 embedded in solid Ne [51], vapor pyridine [150], pyridine in aqueous solution [151], pyridine hemochrome [152].

Comparing the absorption spectrum of Ag_1Py_1 to that of Ag_1Py_0 as shown in the blue curve of figure 6.1, we can see that the four absorption peaks of Ag_1Py_1 at 3.93, 4.06, 4.20 and 4.27 eV are consistent to the corresponding values of 3.93, 4.06, 4.19 and 4.28 eV in the spectrum of Ag_1 except for an energy shift of 0.07 eV. This is attributed to the effect of the pyridine molecule attached to the silver atom. Interestingly, the TDDFT calculations by Jensen et al. has also shown an energy shift of the absorption spectrum of Ag_nPy_1 compared to that of pure Ag_n [60]. For example, Ag_2Py_1 presents a blue shift of 0.27 eV compared to that of pure Ag_2 , and for larger clusters like Ag_4Py_1 and $\text{Ag}_{20}\text{Py}_1$ a red shift of 0.07 eV is displayed.

The cyan curve in figure 6.1 shows the absorption spectrum of pyridine vapor which presents three main peaks at 4.31, 4.38 and 4.45 eV [150]. The first two peaks are consistent with those of 4.27 and 4.39 eV in Ag_1Py_1 spectrum. In contrast, the spectrum of pyridine in aqueous solution shows three main absorption peaks at 4.71, 4.83 and 4.94 eV (the orange curve in figure 6.1) [151] which are higher in energy than all the absorption peaks of Ag_1Py_1 . The green curve shows the spectrum of pyridine hemochrome [152]. Two main peaks at 2.05 and 3.20 eV are in good agreement with those of 2.06 and 3.19 eV of Ag_1Py_1 except for a -0.85 eV shift.

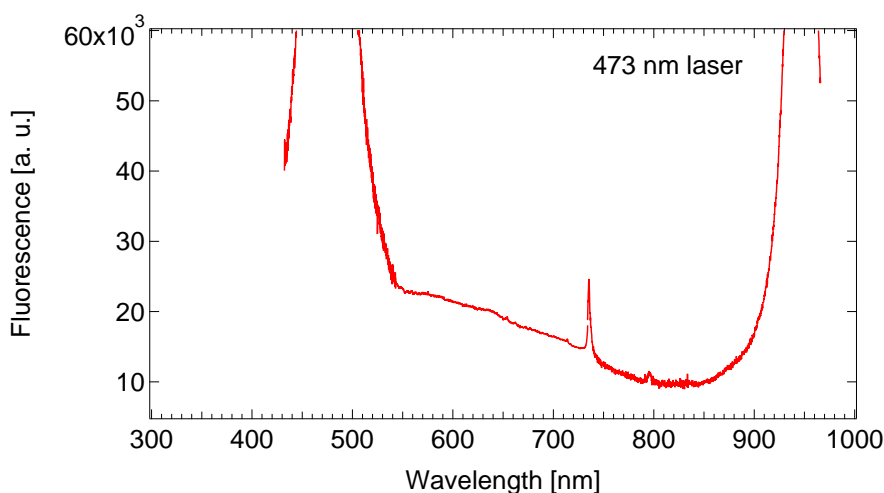


Figure 6.2 – Fluorescence spectrum of size-selected Ag_1Py_1 clusters embedded in solid neon matrix.

6.1.2 Fluorescence of Ag_1Py_1

Figure 6.2 shows the experimental result of fluorescence spectrum on Ag_1Py_1 excited by a 473 nm laser. A very small peak at 735 nm is found, which corresponds to the energy of 1.86 eV in vacuum. Note that the width of this peak is very small - only 2.5 nm of FWHM in wavelength (corresponding to 0.006 eV in energy).

Lecoultré et al. have performed the fluorescence measurements on pure silver atoms embedded in Ne matrix [66]. Fluorescence peaks at 3.75 and 3.55 eV are shown by the excitation at 4.00 eV. Kolb et al. have also performed the fluorescence measurements on silver atoms in solid Kr [153], and found fluorescence peaks at 531, 492 and 415 nm (corresponding to 2.69, 2.87 and 3.34 eV respectively considering a blue shift of 0.35 eV for Kr matrix effect) by the excitation at 309, 314 and 323 nm. Besides, Yamazaki et al. [150] have done the fluorescence measurements on pure pyridine vapor and found peaks at 333 nm (corresponding to 3.72 eV) with the FWHM of 45 nm (corresponding to 0.5 eV) by the excitation at 287 nm (corresponding to 4.32 eV).

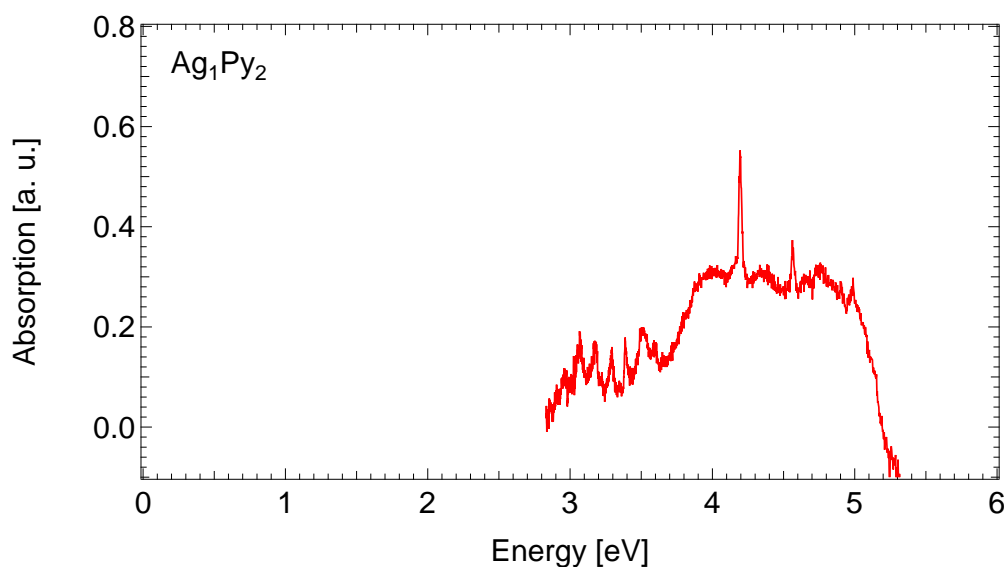


Figure 6.3 – Optical absorption spectrum of size-selected Ag₁Py₂ clusters embedded in solid neon matrix.

6.2 Optical response of Ag₁Py₂

6.2.1 Absorption of Ag₁Py₂

Figure 6.3 shows the experimental result of absorption spectrum on size-selected Ag₁Py₂ clusters embedded in solid neon. Two main peaks at 4.20 and 4.56 eV and seven small peaks at 3.08, 3.18, 3.29, 3.39, 3.52, 3.60 and 4.75 eV are found. Compared the absorption spectrum of Ag₁Py₂ with that of Ag₁Py₁, we can see that the four absorption peaks of Ag₁Py₂ at 3.18, 3.39, 4.20 and 4.56 eV are in good agreement with the corresponding values of 3.19, 3.40, 4.20 and 4.56 eV in the spectrum of Ag₁Py₁. This manifests that these four peaks can serve as the fingerprints for compounds of pyridine molecules attached to a silver atom.

6.2.2 Fluorescence of Ag₁Py₂

Figure 6.4 shows the experimental result of fluorescence spectrum on Ag₁Py₂ excited by a 450 nm laser and a 473 nm laser respectively. A large fluorescent peak at 735 nm with FWHM of 2.5 nm is found for both excitations, which corresponds to the energy of 1.86 eV with FWHM of 0.006 eV in vacuum. This is interestingly the same as that of Ag₁Py₁. In addition, a small peak at 795 nm with FWHM of 2.0 nm (corresponding to 1.73 eV with FWHM of 0.004 eV) is presented for both excitations at 450 and 473 nm. However, for the excitation at 473 nm, Ag₁Py₂ shows a very wide peak at about 650 nm with FWHM of 130 nm (corresponding to 2.08 eV with FWHM of 0.17 eV), while for the excitation at 450 nm, a tiny peak at about 613 nm (corresponding to 2.19 eV) is shown.

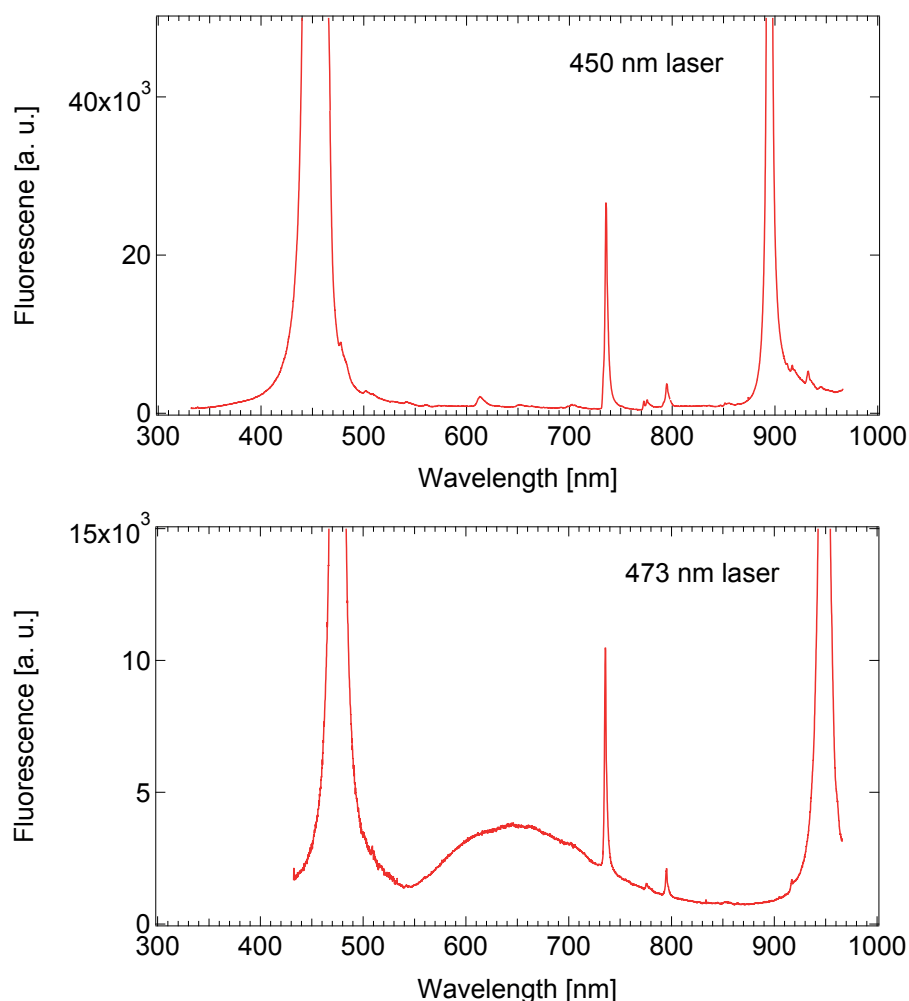


Figure 6.4 – Fluorescence spectrum of size-selected Ag_1Py_2 clusters embedded in solid neon matrix.

6.2.3 SERS of Ag_1Py_2

Figure 6.5 shows the Raman scattering measurements on size-selected Ag_1Py_2 clusters. Two Stokes shifted Raman peaks are found at 1075 and 1102 cm^{-1} (corresponding to 0.1316 and 0.1365 eV in energy) excited by a 473 nm laser. These two peaks are the typical Raman peaks of silver-pyridine compounds, which are slightly shifted from those (992 and 1031 for pyridine vapor [154] and 988 and 1027 for pyridine liquid [155]) of pure pyridine that are always used as a fingerprint for pyridine, depending on the composition and structure. For example, the Raman peaks of pyridine adsorbed at a silver electrode are found at 1005 and 1037 cm^{-1} [56], and the TDDFT calculations of $\text{Ag}_n\text{-Py}$ ($n = 2 - 8$) clusters have given the Raman peaks at 979 and 1022 cm^{-1} [60].

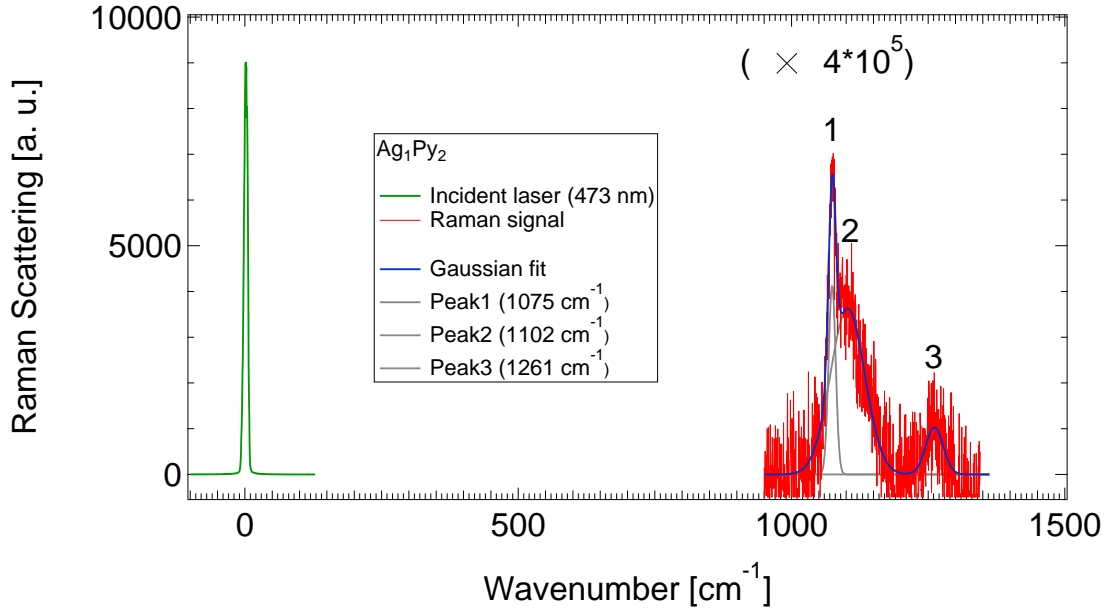


Figure 6.5 – Raman scattering spectrum of size-selected Ag_1Py_2 clusters embedded in solid neon matrix.

According to theory, the light intensity I_R after Raman scattering by clusters can be written as

$$I_R = \frac{24\pi\omega^4}{c^4} I_0 \alpha^2, \quad (6.1)$$

where I_0 is the initial light intensity before Raman scattering, ω is the frequency of the excitation light, and α is the total Raman cross section [156]. Hence, from equation 6.1 the Raman cross section per cluster can be calculated as

$$\alpha_0 = \frac{\alpha}{N} = \left(\frac{\beta}{3 \times 2^7 \pi^5} \right)^{\frac{1}{2}} \frac{\lambda^2}{N}, \quad (6.2)$$

where $\beta = I_R / I_0$, λ is the wavelength of the excitation light, and N is the number of clusters in the matrix. For the 1075 cm^{-1} Raman peak, $\beta(1075) = 2.1 \times 10^{-6}$; and for the 1102 cm^{-1} Raman peak, $\beta(1102) = 8.8 \times 10^{-6}$. The total number of Ag_1Py_2 clusters is about 9×10^{12} estimated by the cluster current of 100 pA and deposition time of 2.5 h. Therefore, according to equation 6.2, the Raman cross sections of Ag_1Py_2 are $1200 \times 10^{-30} \text{ cm}^2$ for the peak of 1075 cm^{-1} and $4000 \times 10^{-30} \text{ cm}^2$ for the one of 1102 cm^{-1} , which have an estimated enhancement factor of about 10^3 compared to the normal Raman cross section of $1 \times 10^{-30} \text{ cm}^2$ [60].

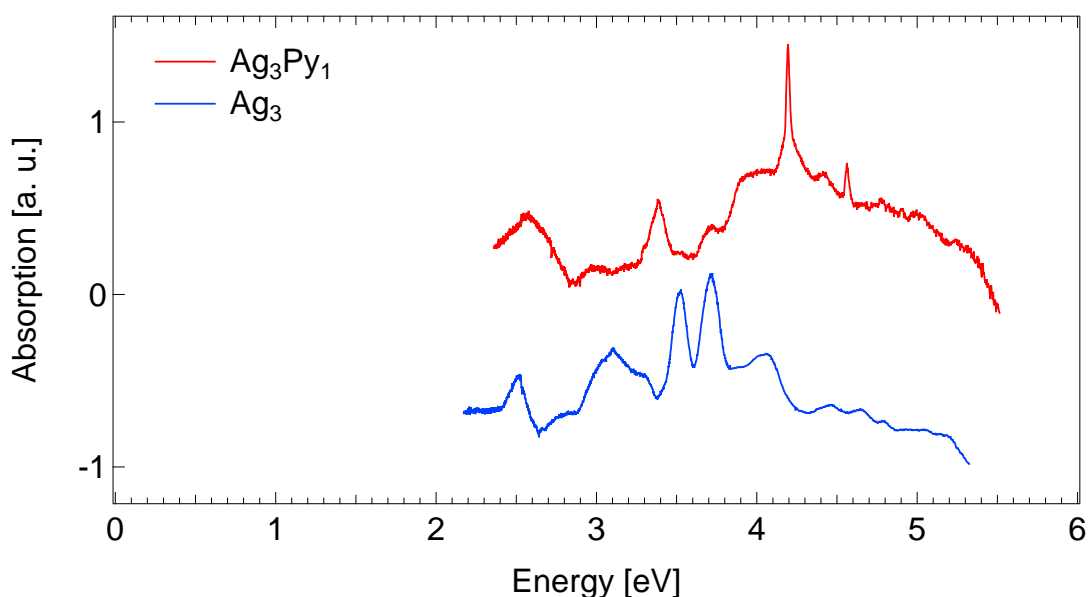


Figure 6.6 – Comparison of optical absorption spectrum of Ag_3Py_1 to that of Ag_3 .

6.3 Optical response of Ag_3Py_1

6.3.1 Absorption of Ag_3Py_1

Figure 6.6 (red curve) shows the experimental result of absorption spectrum on size-selected Ag_3Py_1 clusters embedded in solid neon. Three main peaks at 3.38, 4.20 and 4.56 eV and five small peaks at 2.58, 3.02, 3.73, 4.43 and 4.78 eV are found. Compared the absorption spectrum of Ag_3Py_1 to that of Ag_1Py_1 , we can clearly find that the four absorption peaks of Ag_3Py_1 at 2.58, 3.38, 4.20 and 4.56 eV are consistent to the corresponding values of 2.55, 3.40, 4.20 and 4.56 eV in the spectrum of Ag_1Py_1 . This manifests that these four peaks can serve as fingerprints for compounds of silver clusters attached to a pyridine molecule. Moreover, compared the absorption spectrum of Ag_3Py_1 to that of Ag_3Py_0 (see the blue curve in figure 6.6), we can see that two peaks of Ag_3Py_1 at 3.73 and 4.43 eV are in good agreement with the corresponding values of 3.71 and 4.47 eV in the spectrum of Ag_3Py_0 . This means these two peaks are the fingerprints for Ag_3Py_b compounds.

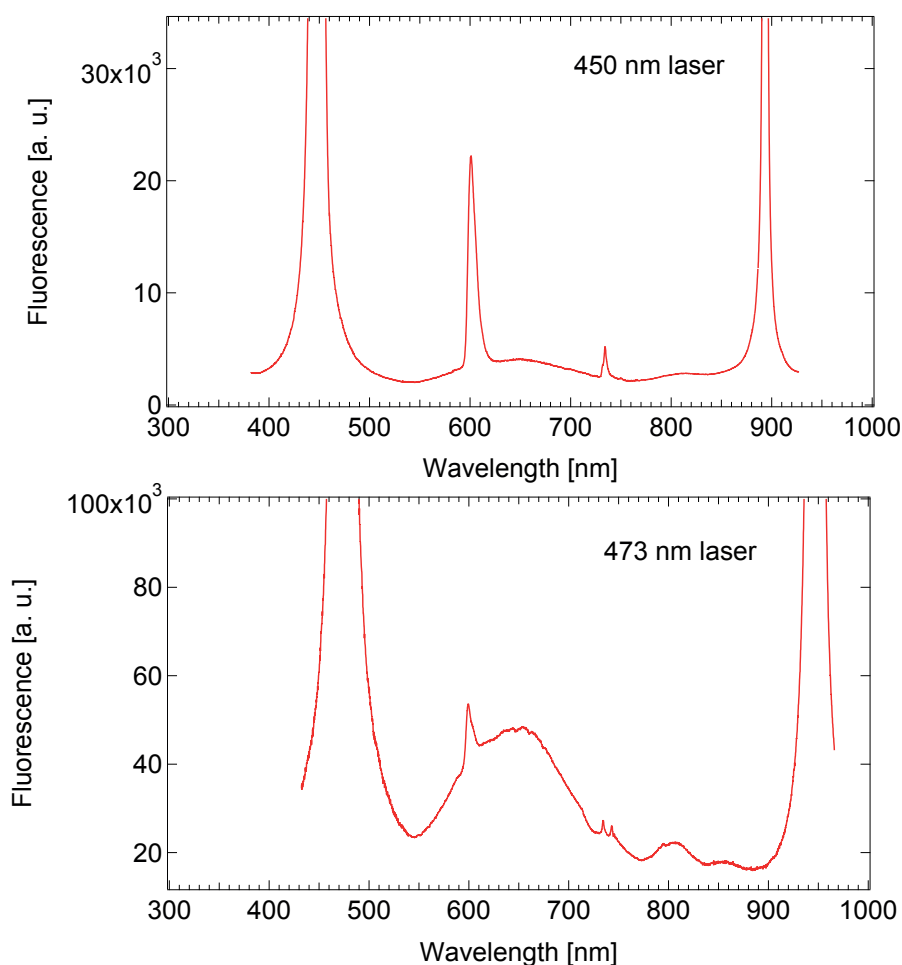


Figure 6.7 – Fluorescence spectrum of size-selected Ag_3Py_1 clusters embedded in solid neon matrix.

6.3.2 Fluorescence of Ag_3Py_1

Figure 6.7 shows the experimental result of fluorescence spectrum on Ag_3Py_1 excited by a 450 nm laser and a 473 nm laser respectively. A large fluorescent peak at 601 nm with FWHM of 7.0 nm is found for both excitations, which corresponds to the energy of 2.23 eV with FWHM of 0.024 eV in vacuum. This is interestingly the same as that of Ag_3Py_0 as shown in figure 3.25. In addition, a small peak at 734 nm with FWHM of 4.0 nm (corresponding to 1.86 eV with FWHM of 0.010 eV) presents for both excitations at 450 and 473 nm. Similarly to Ag_1Py_2 , for the excitation at 473 nm, Ag_3Py_1 shows a very wide peak at about 650 nm with FWHM of 130 nm (corresponding to 2.08 eV with FWHM of 0.17 eV), while no such wide peak is shown for the excitation at 450 nm.

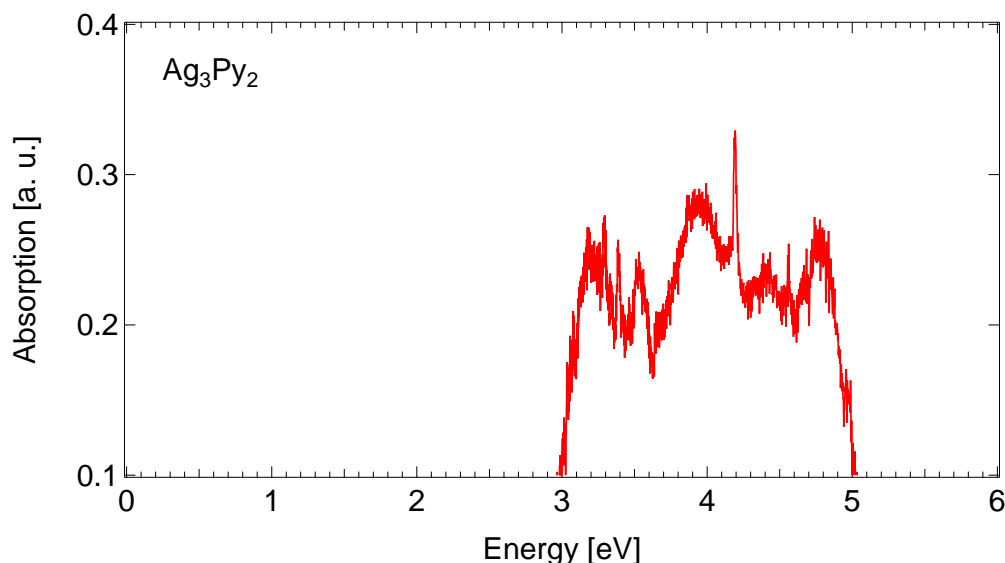


Figure 6.8 – Optical absorption spectrum of size-selected Ag_3Py_2 clusters embedded in solid neon matrix.

6.4 Optical response of Ag_3Py_2

6.4.1 Absorption of Ag_3Py_2

Figure 6.8 shows the experimental result of absorption spectrum on size-selected Ag_3Py_2 clusters embedded in solid neon. Two main peaks at 4.20 and 4.56 eV and five small peaks at 3.30, 3.39, 3.54, 3.94 and 4.40 eV are found. Compared the absorption spectrum of Ag_3Py_2 to that of Ag_3Py_1 , we can find two identical peaks at 4.20 and 4.56 eV. These two peaks also exist in Ag_1Py_2 and Ag_1Py_1 clusters. Besides, compared the absorption spectrum of Ag_3Py_2 to that of Ag_1Py_2 , we can see that the four absorption peaks of Ag_3Py_2 at 3.39, 3.54, 4.20 and 4.56 eV are consistent to the corresponding values of 3.39, 3.52, 4.20 and 4.56 eV in the spectrum of Ag_1Py_2 . This manifests that these four peaks can serve as fingerprints for compounds of silver clusters attached to two pyridine molecules.

6.4.2 Fluorescence of Ag_3Py_2

Figure 6.9 shows the experimental result of fluorescence spectrum on Ag_3Py_2 excited by a 450 nm laser and a 473 nm laser respectively. A large fluorescence peak at 735 nm with FWHM of 2.5 nm is found for both excitations, which corresponds to the energy of 1.86 eV with FWHM of 0.006 eV in vacuum. In addition, a small peak at 795 nm with FWHM of 2.0 nm (corresponding to 1.73 eV with FWHM of 0.004 eV) is presented for both excitations at 450 and 473 nm. Interestingly, this is exactly the same as that of Ag_1Py_2 . Different from Ag_3Py_1 and Ag_1Py_2 , Ag_3Py_2 does not show a wide fluorescence peak at 650 nm (corresponding to 2.08 eV).

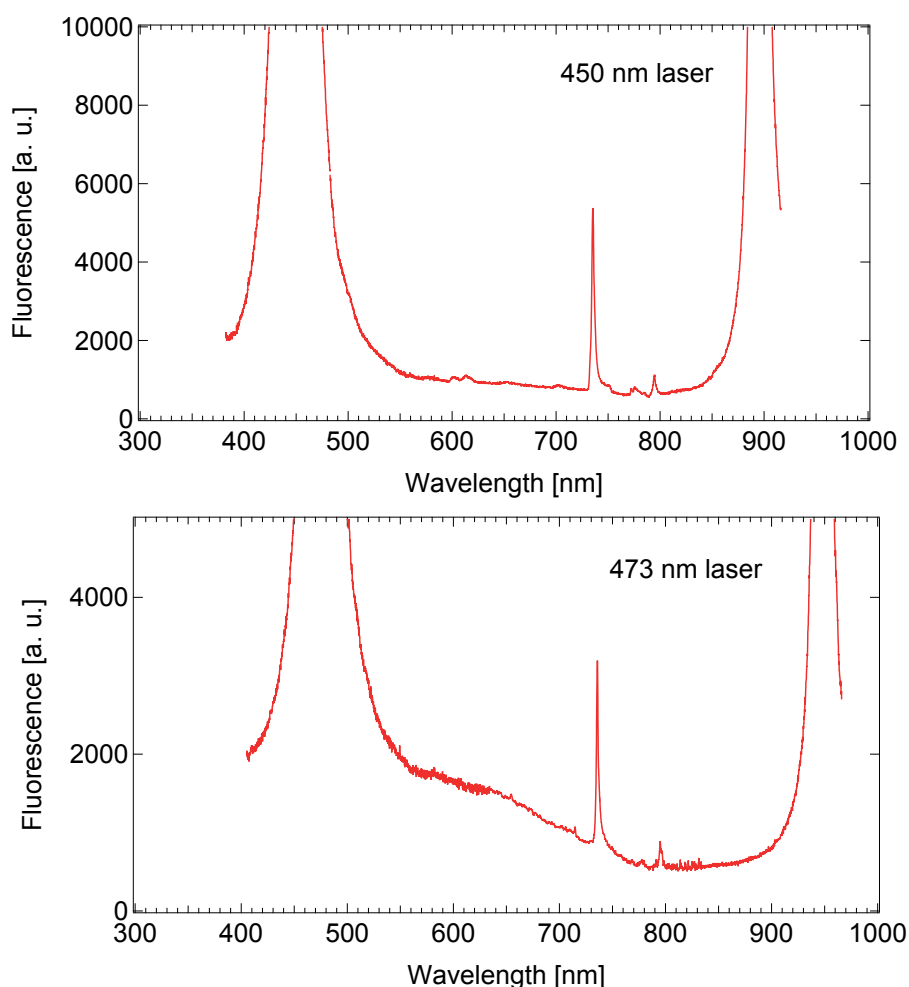


Figure 6.9 – Fluorescence spectrum of size-selected Ag_3Py_2 clusters embedded in solid neon matrix.

6.4.3 SERS of Ag_3Py_2

Figure 6.10 shows the Raman scattering measurements on size-selected Ag_3Py_2 clusters. Two Stokes shifted Raman peaks are found at 1032 and 1090 cm^{-1} (corresponding to 0.1272 and 0.1353 eV in energy) excited by a 375 nm laser. As discussed in Section 6.2.3, these two peaks are also the typical Raman peaks of silver-pyridine compounds, which are slightly shifted from that of Ag_1Py_2 and pure pyridine because of the different compositions. According to equation 6.2, $\beta(1032) = 1.2 \times 10^{-6}$ and $\beta(1090) = 5.8 \times 10^{-6}$. The total number of Ag_1Py_2 clusters is about 6.75×10^{12} . Therefore, the Raman cross sections of Ag_3Py_2 are $500 \times 10^{-30}\text{ cm}^2$ for the peak of 1032 cm^{-1} and $1500 \times 10^{-30}\text{ cm}^2$ for the one of 1090 cm^{-1} , which have also an estimated enhancement factor of about 10^3 compared with the normal Raman cross section of $1 \times 10^{-30}\text{ cm}^2$ [60].

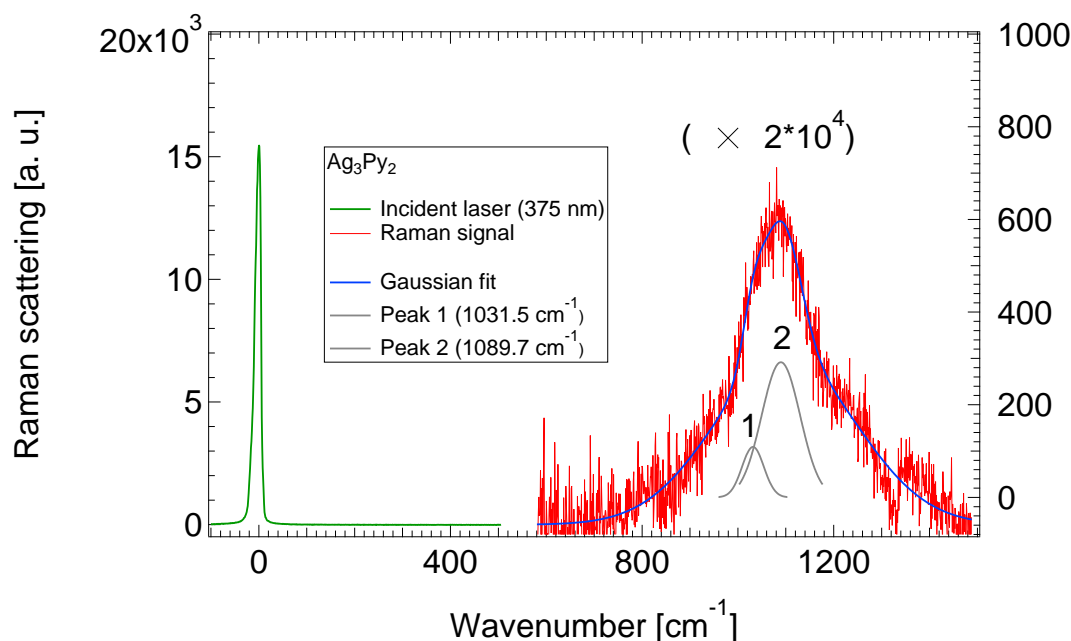


Figure 6.10 – Raman scattering spectrum of size-selected Ag_3Py_2 clusters embedded in solid neon matrix.

6.5 Conclusion of optical response of Ag_aPy_b ($a = 1, 3; b = 0, 1, 2$)

The comparison of optical absorption spectra of Ag_aPy_b ($a = 1, 3; b = 0, 1, 2$) clusters is presented in figure 6.11. The spectra are grouped on the left hand side according to the number of Ag atoms and on the right according to the number of pyridine molecules. As clearly seen, Ag_aPy_b clusters with the same number of pyridine molecules present more similar spectra than those with the same number of silver atoms. It is evident that the number of pyridine molecules strongly changes the spectra, while the number of Ag atoms has less influence on the absorption features. The same trend also holds for the fluorescence spectra, namely, the number of Ag atoms is less influential than the one of pyridine molecules.

Table 6.1 and figure 6.12 list the peaks energies in absorption, fluorescence and SERS spectra for Ag_aPy_b ($a = 1, 3; b = 0, 1, 2$) compounds. One sees from table 6.1 that 4.20 and 4.56 eV are the fingerprints for absorption spectra, and 1.73 and 1.86 eV are the fingerprints for fluorescence spectra.

This is the very first time that the SERS on size-selected Ag_aPy_b clusters has been observed. An enhancement factor of 10^3 is shown for both Ag_1Py_2 and Ag_3Py_2 . An interesting effect is that the SERS in our experiment only exists in Ag_aPy_2 compounds but not in Ag_aPy_1 compounds, which needs to be further studied. We suggest that our experimental results of the SERS in well defined systems can be compared to further theories under certain assumptions of the mechanism for the enhancement thus possibly revealing the mechanism.

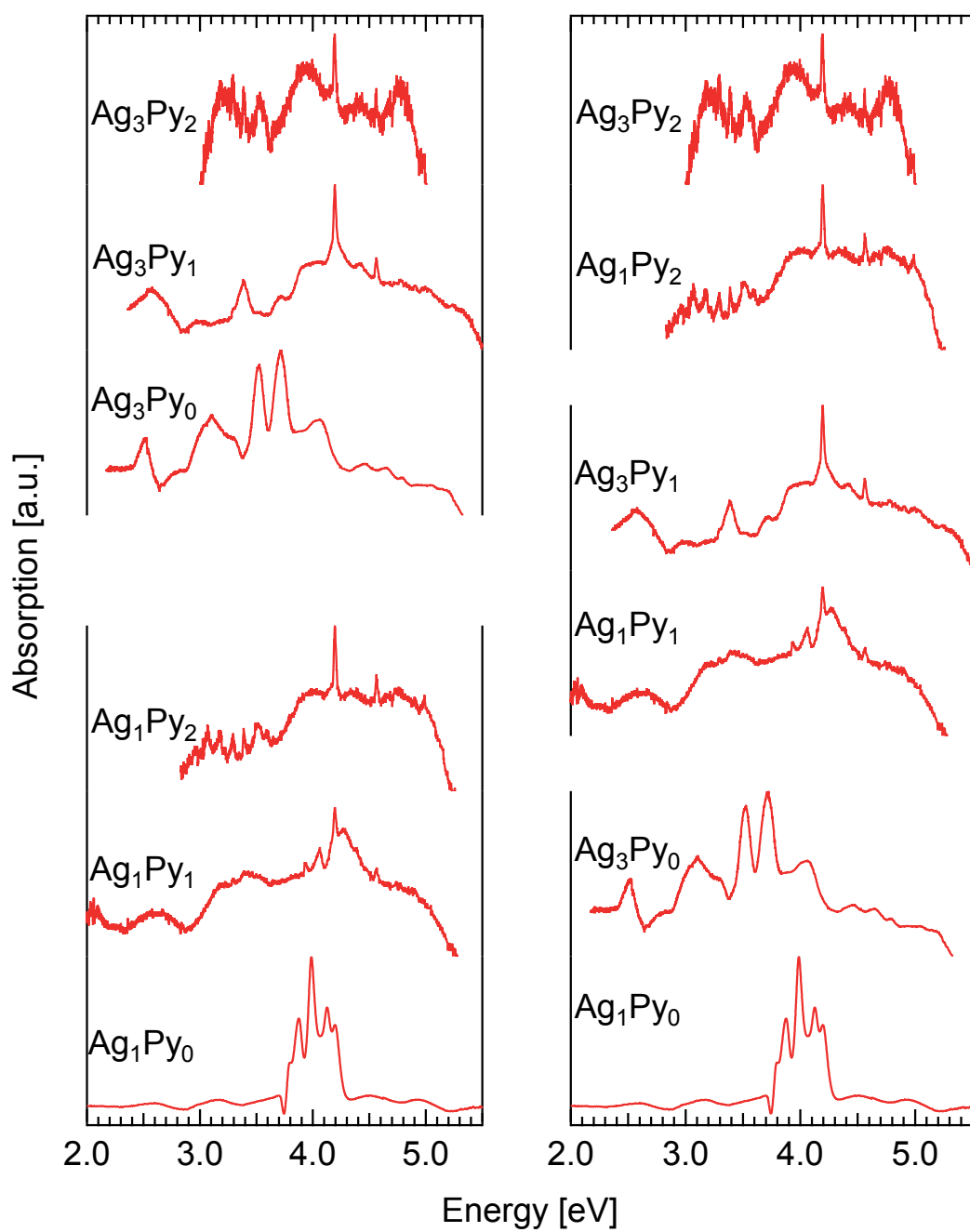


Figure 6.11 – Comparison of optical absorption spectra of Ag_aPy_b ($a = 1, 3; b = 0, 1, 2$) clusters.

Ag_aPy_b	Absorption (eV)			Fluorescence (eV)						SERS (eV)	
				450 nm laser			473 nm laser				
Ag_1Py_0	3.79	3.86	3.99								
	4.12	4.21									
Ag_1Py_1	2.55	3.19	3.40				1.86				
	3.93	4.06	4.20								
	4.27	4.39	4.56								
Ag_1Py_2	3.08	3.18	3.29	1.73	1.86	2.19	1.73	1.86	2.08	0.1316	0.1365
	3.39	3.52	3.60								
	4.20	4.56	4.75								
Ag_3Py_0	2.52	3.11	3.52	1.70	2.23		1.62	1.71	2.24		
	3.71	4.06	4.47								
	4.64										
Ag_3Py_1	2.58	3.02	3.38	1.86	2.23		1.86	2.23			
	3.73	4.20	4.43								
	4.56	4.78									
Ag_3Py_2	3.30	3.39	3.54	1.73	1.86		1.73	1.85		0.1272	0.1353
	3.94	4.20	4.40								
	4.56										

Table 6.1 – Energies of peaks in absorption, fluorescence and SERS spectra in Ag_aPy_b ($a = 1, 3$; $b = 0, 1, 2$) clusters.

6.5. Conclusion of optical response of Ag_aPy_b ($a = 1, 3; b = 0, 1, 2$)

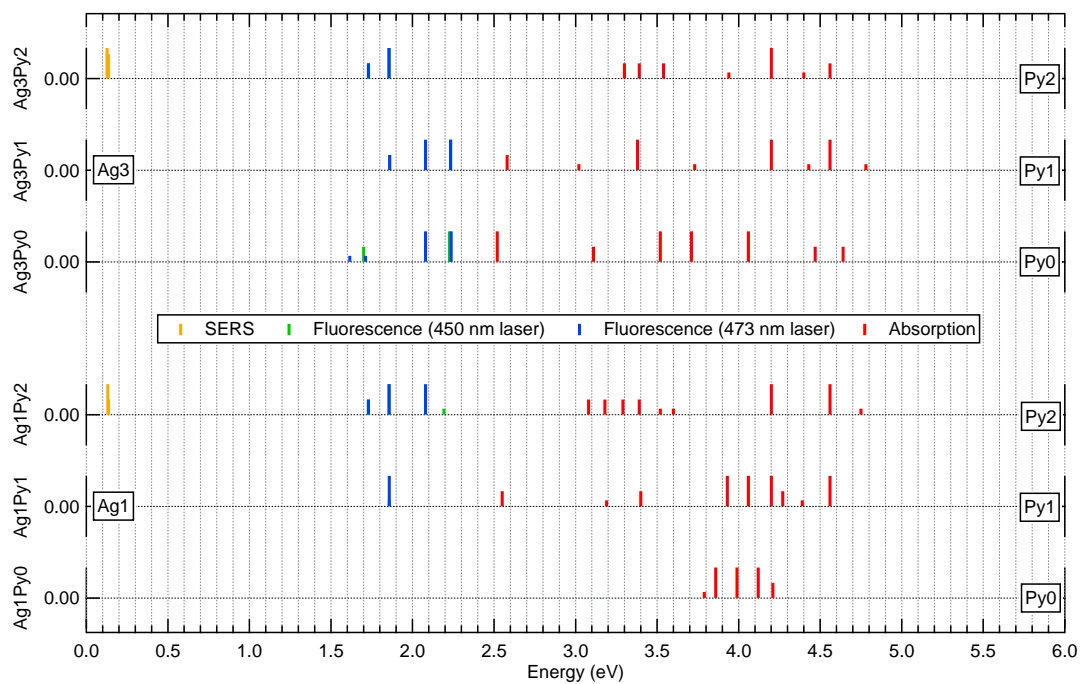


Figure 6.12 – Peaks of optical absorption, fluorescence and Raman scattering in Ag_aPy_b ($a = 1, 3; b = 0, 1, 2$) clusters.

7 Conclusions

The optical properties of small size-selected neutral metal clusters have been studied in order to explore the electronic and geometric structures of small metal clusters. Cationic metal cluster-organic compounds have been produced in different stoichiometries, mass selected and isolated as neutrals in a rare gas solid. To achieve these objectives a UHV compatible apparatus, allowing for the fabrication, size-selection and deposition of small metal clusters and metal-organic compounds in a solid rare-gas matrix under cryogenic conditions has been developed. Cluster cations are formed in a combined sputtering gas aggregation source commonly named the Haberland-Issendorf source. The combination of an AC or DC magnetron sputtering source, which allows to create atomic vapor of basically any element together with rare gas condensation makes this source very polyvalent. A novel custom-made radio frequency driven conical octupole serves to efficiently collect charged clusters and inject them into an electrostatic and radio frequency beam line which allows for mass selection and particle transport up to the deposition region where they are co-deposited together with excess rare gas (forming the matrix) and electrons for neutralization. Mass selection is performed by either one of two quadrupoles operating at low frequency which covers the mass range from 1 to 16,000 amu. The new source will be able to produce clusters of basically any element and forming a beam of mono dispersed clusters in the mentioned size range. This source has proven its performance in producing clusters of Ag and Au in large quantities. Cluster currents are sufficiently strong to allow for an accumulation of neutral clusters in an inert medium with sufficient densities. Clusters can be analyzed by absorption, fluorescence, excitation spectroscopy and Raman scattering in the UV-visible energy range.

The optical absorption on size-selected small silver clusters of Ag_n ($n = 20, 35, 55, 58, 84, 92, 120$) embedded in neon solid matrix has been investigated. These measurements extend previous studies to a larger size range closing the gap between molecular like absorption profiles on one side and plasmonic excitations on the other side obtained by electron energy loss spectroscopy on single particles using aberration corrected electron microscopes. A surface plasmon like absorption profile around 4.0 eV was found for the clusters in this size range. This energy is close to the molecular like absorptions of the smallest clusters but sensitively larger than

would be expected from the dielectric function of bulk silver. Among these clusters, Ag₅₈ shows the highest plasmon energy of 4.10 eV and Ag₁₂₀ shows the lowest plasmon energy of 3.90 eV. Besides, Ag₂₀, Ag₅₅, Ag₉₂ present respectively narrow absorption widths (< 0.32 eV of FWHM), while Ag₃₅, Ag₅₈, Ag₈₄, Ag₁₂₀ present respectively wide absorption widths (> 0.42 eV of FWHM). The spectra of Ag₂₀, Ag₃₅, Ag₈₄, Ag₁₂₀ were compared to the TDDFT calculations of clusters with highly symmetric tetrahedral structures, and the comparison results show that these selected clusters possess ground states with non-tetrahedral structures. Clusters with atom number of 8, 18, 34, 58, 92 show a localized maximum value of plasmon energy. These numbers correspond to the fully filled states of 1p, 1d, 1f, 1g and 1h according to the electronic shell model, manifesting a sub-shell effect.

The optical spectra of Au clusters which are ligand stabilized have been obtained in recent years. One of the key questions is whether the optical properties, absorption as well as fluorescence are properties of the Au clusters themselves or ligand mediated. We were successful to measure optical absorption, fluorescence and excitation on size-selected small gold clusters of Au_m (m= 19, 20, 21) embedded in neon solid matrix. This environment is inert up to very high excitation energies and the optical spectrum of the pure Au cluster is measured. These are the first optical data on ligand free neutral atomically precise Au clusters. All three clusters show continuous absorption spectra monotonically increasing from 2.0 to 5.5 eV. In addition, superposed to the monotonous increase, Au₂₀ presents a rich-structured absorption spectrum while Au₁₉ and Au₂₁ present poor-structured spectra. While the absorption background is reflected in ligand stabilized clusters, this is not the case for the rich fine structure. TDDFT calculations, which are in fairly good agreement show also these rich structures. Most important, all three Au clusters show strong fluorescence centered at around 1.85 eV, thus clearly proving that the fluorescence comes from the Au cluster itself and is only weakly influenced by the ligands.

Finally, optical absorption, fluorescence and Raman scattering on size-selected small silver-pyridine compounds of Ag_aPy_b (a=1,3; b=1,2) embedded in neon solid matrix were performed. For the first time these prototype metal-organic clusters could be isolated and measured. Absorption peaks between 2.5 and 4.8 eV as well as fluorescence peaks between 1.6 and 2.3 eV are shown in these compounds. Interestingly, the number of pyridine molecules strongly changes the spectra, while the number of Ag atoms has less influence on the absorption and fluorescence features. Most important, the SERS with an enhancement factor of 10³ on size-selected Ag₁Py₂ and Ag₃Py₂ clusters have been observed. We suggest that our experimental results of the SERS in well defined systems can be taken as a benchmark for further theories thus possibly revealing the mechanism of the SERS.

A Supporting information to devices

Section 3.4.1 has shown the custom-made conical octupole which was designed to focus the cluster ions. As discussed, the eight conical rods of the octupole are separated into two groups in order to avoid short-circuit of the electrodes. Actually, this is already an improved version of the octupole. Figure A.1 shows the original version of the octupole. Compared with the improved version shown in figure 3.4, all the eight rods of the original octupole are fixed together on a ceramic plate. After using it for a month, we have found that a short-circuit of the electrodes has occurred caused by the metallization of the ceramic due to the metal vapor transported by the rare gas. Therefore, a frequently periodic cleaning of the octupole is inevitable for the maintain of the original version of the octupole. By contrast, the improved version of the octupole has been used for two years and no short-circuit has been found. This manifests that the improved one is very practical and reliable.



Figure A.1 – Photos and model of the original version of home-made conical octupole.

B Supporting information to simulations

Section 3.8 has discussed the SIMION simulations of cluster ions passing through the ion guide device. Here we will supplement some additional simulation results of cluster ions passing through the conical octupole (see Section 3.4.1) and the lens (see Section 3.4.3).

Figure B.1 shows the simulations of ion particles passing through a conical octupole toward the quadrupole, where the blue curves represent the trajectory of ions. As discussed in Section 3.4.1, the octupole serves to focus the cluster ions from cluster source into the quadrupole. An important key to judge the ability of the octupole is the transmission of ions passing through it. The transmission can be affected both by the initial conditions of ion particles and by the parameters of octupole. Figure B.2 shows the simulation results of transmission of ion particles passing through the octupole as a function of different parameters. We can see from figure B.2(a) that the transmission decreases slowly when the initial kinetic energy of ions increases. A smaller initial diameter of ions distribution or a smaller initial angle of ion speed direction results in a higher transmission, as seen from figure B.2(b)-(c). Besides, the transmission does not change with the change of DC voltage of the octupole as shown in figure B.2(d). But there exist an optimal AC voltage and an optimal radio frequency for the highest transmission, as shown in figure B.2(e)-(f).

Figure B.3 shows the simulations of ion particles passing through an electrostatic lens toward the deposition head. As discussed in Sections 3.4.3 and 3.6.1, the lens before the sample holder serves to focus the cluster ions thus having a high deposition rate. An important key to judge the ability of the lens is the transmission of ions passing through the sample holder, that is the deposition rate. The transmission can be affected by the focus of the ions that is strongly dominated by the parameter of the voltage V_B of the center piece of the lens. We can clearly see from figure B.3 that the focus of ions is very sensitive to V_B , and the optimal value of $V_B = -20$ V for the best focus can also result in the highest transmission of the ions, as shown in figure B.4.

Appendix B. Supporting information to simulations

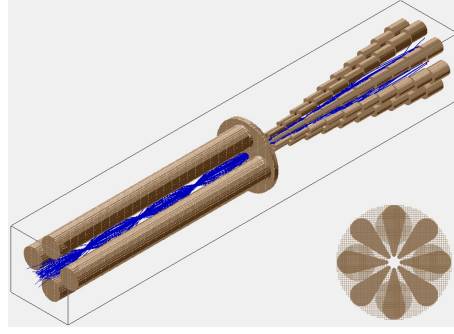


Figure B.1 – Simion simulations of ion particles passing through a conical octupole toward the quadrupole. Here the blue curves represent the trajectory of ions.

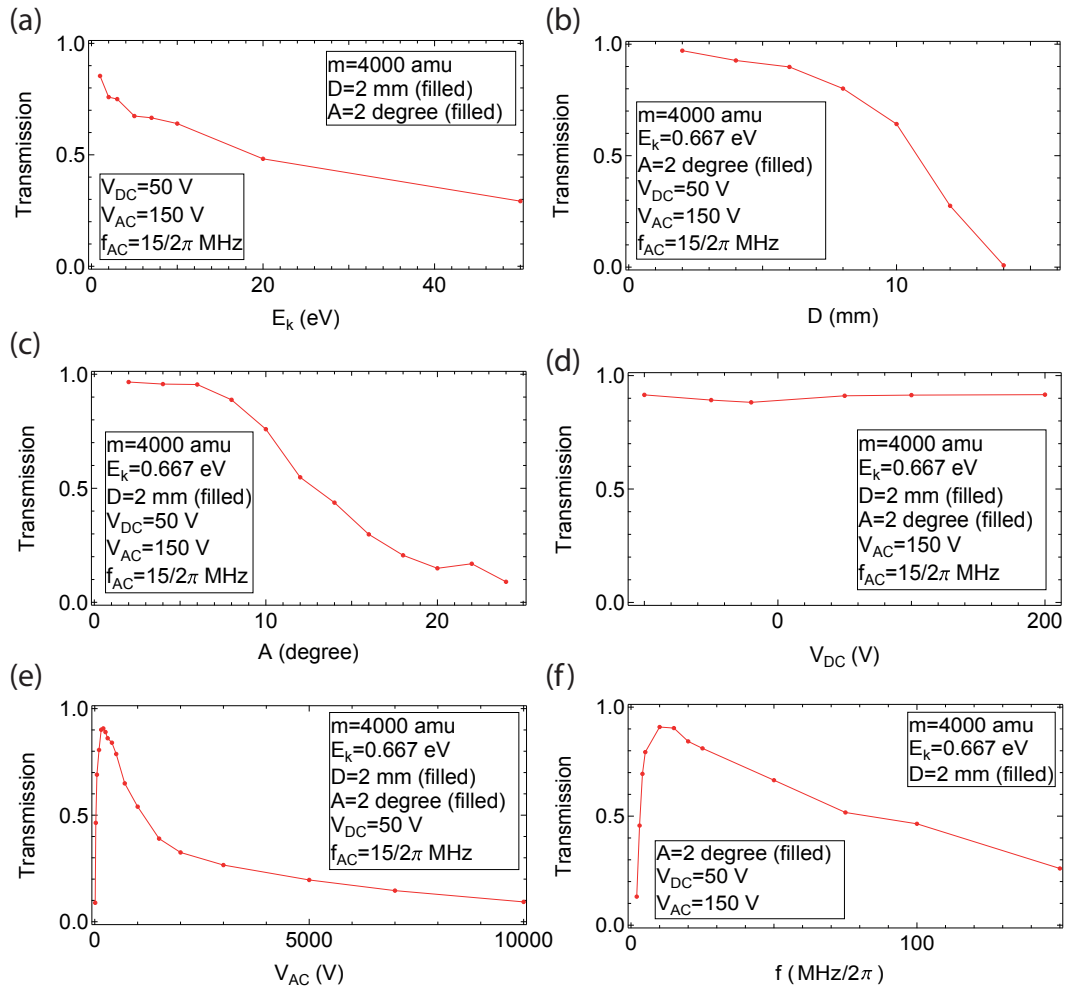


Figure B.2 – Simulation results of transmission of ion particles passing through a conical octupole as a function of (a) initial kinetic energy of ions, (b) initial diameter of ions distribution, (c) initial angle of ion speed direction, (d) DC voltage of octupole, (e) AC voltage of octupole, and (f) radio frequency of octupole.

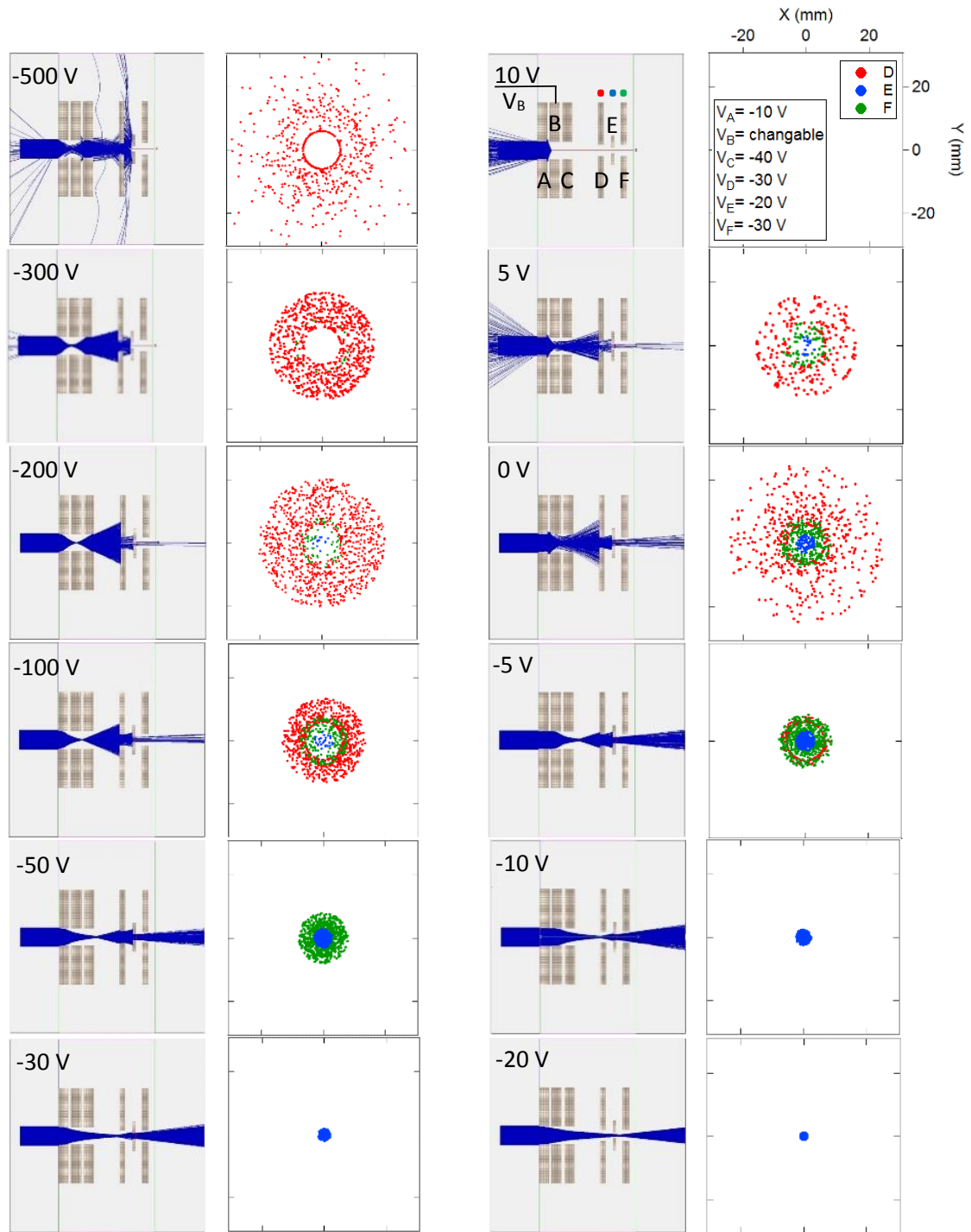


Figure B.3 – Left: Simulations of ion particles passing through an electrostatic lens (consisting of pieces *A*, *B* and *C*) toward the sample holder (consisting of pieces *D*, *E* and *F*) as a function of the voltage V_B of the center piece *B* of the lens. Here the blue curves represent the trajectory of the ions. Right: Simulation results of ions cross section distributions on the pieces of the sample holder, where the red dots represent the distributions of ion particles on the surface of piece *D*, and the blue (or green) dots represent those of piece *E* (or *F*).

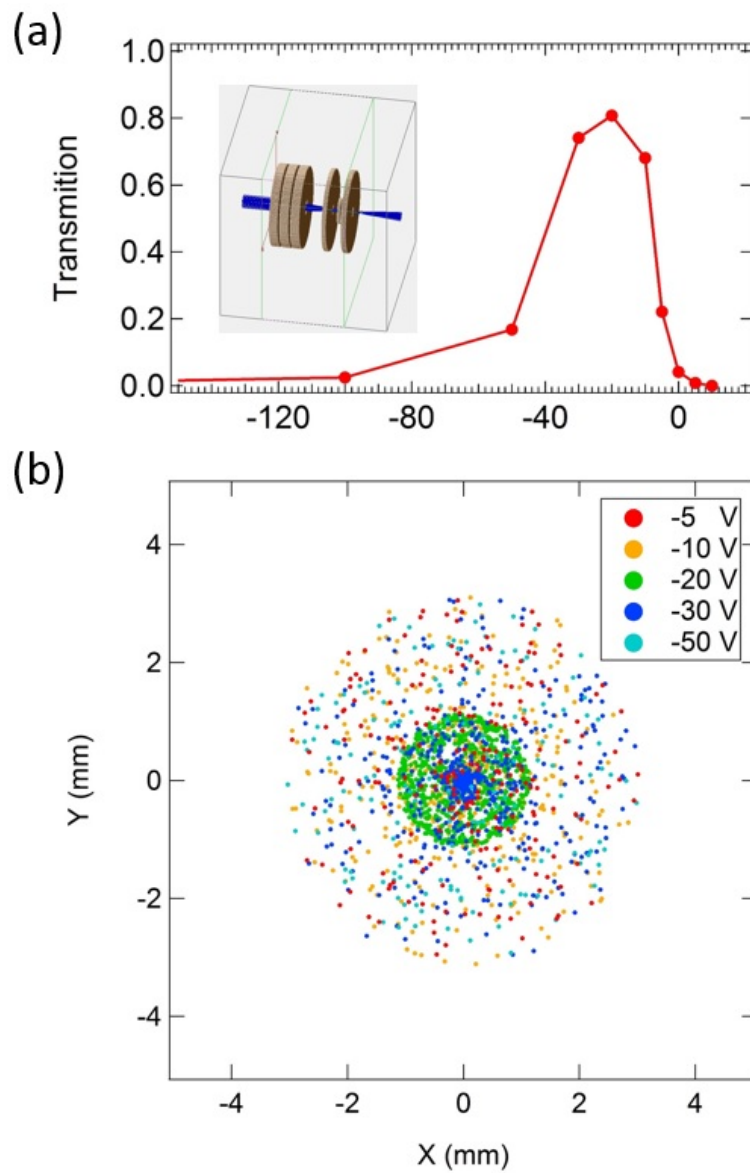


Figure B.4 – (a) Simulation results of transmission of ion particles passing through an electrostatic lens and the sample holder as a function of V_B . (b) Simulation results of cross section distributions of ion particles on the surface of piece E with different V_B .

Bibliography

- [1] I. Newton. Letter to Robert Hooke. 1676.
- [2] S. Hawking. Galileo and the birth of modern science. *American Heritage's Invention & Technology*, 24(1):36, 2009.
- [3] I. Newton. Principia, axioms or laws of motion. 1:19, 1729.
- [4] I. Newton. Principia, Book 3, General Scholium. 2:392, 1729.
- [5] A. Einstein. Zur elektrodynamik bewegter korper. *Annalen der Physik*, 17:891, 1905.
- [6] M. Planck. On the law of distribution of energy in the normal spectrum. *Annalen der Physik*, 4(3):553, 1901.
- [7] J. Strutt. On the scattering of light by small particles. *Philosophical Magazine*, 41(4):447–454, 1871.
- [8] G. Mie. *Ann. Phys. (Leipzig)*, 25(377), 1908.
- [9] U. Kreibig. *Z. Phys.*, 234(307), 1970.
- [10] W. D. Knight, K. Clemenger, W. A. de Heer, W. A. Saunders, M. Y. Chou, and M. L. Cohen. *Phys. Rev. Lett.*, 52(2141), 1984.
- [11] W. Ekardt. *Phys. Rev. Lett.*, 52(1925), 1984.
- [12] J. L. Persson, R. L. Whetten, H.-P. Cheng, and R. S. Berry. *Chem. Phys. Lett.*, 186(215), 1991.
- [13] H. Jahn and E. Teller. Stability of polyatomic molecules in degenerate electronic states. i. orbital degeneracy. *Proceedings of the Royal Society A*, 161(905):220–235, 1937.
- [14] K. Clemenger. *Phys. Rev. B*, 32(1359), 1985.
- [15] S. G. Nilsson. *K. Dan. Vidensk. Selsk. Mat. Fys. Medd.*, 29(16), 1955.
- [16] J. Li, X. Li, H. J. Zhai, and L. S. Wang. Au-20: A tetrahedral cluster. *Science*, 299(5608):864–867, February 2003.

- [17] H. Haberland. Looking from both sides. *Nature*, 494(7435):E1–2, February 2013.
- [18] C. M. Aikens, S. Li, and G. C. Schatz. From discrete electronic states to plasmons: TDDFT optical absorption properties of Ag(*n*) (*n* = 10, 20, 35, 56, 84, 120) tetrahedral clusters. *Journal of Physical Chemistry C*, 112(30):11272–11279, July 2008.
- [19] M. Chen, Jason E. Dyer, K. Li, and David A. Dixon. Prediction of structures and atomization energies of small silver clusters, (Ag)(*n*), *n* < 100. *Journal of Physical Chemistry A*, 117(34):8298–8313, August 2013.
- [20] B. Anak, M. Bencharif, and F. Rabilloud. Time-dependent density functional study of UV-visible absorption spectra of small noble metal clusters (Cu-*n*, Ag-*n*, Au-*n*, *n*=2-9, 20). *Rsc Advances*, 4(25):13001–13011, 2014.
- [21] F. Furche, R. Ahlrichs, P. Weis, C. Jacob, S. Gilb, T. Bierweiler, and M. M. Kappes. The structures of small gold cluster anions as determined by a combination of ion mobility measurements and density functional calculations. *Journal of Chemical Physics*, 117(15):6982–6990, October 2002.
- [22] S. Gilb, P. Weis, F. Furche, R. Ahlrichs, and M. M. Kappes. Structures of small gold cluster cations (Au-*n*(+), *n* < 14): Ion mobility measurements versus density functional calculations. *Journal of Chemical Physics*, 116(10):4094–4101, March 2002.
- [23] R. R. Hudgins, M. Imai, M. F. Jarrold, and P. Dugourd. High-resolution ion mobility measurements for silicon cluster anions and cations. *Journal of Chemical Physics*, 111(17):7865–7870, November 1999.
- [24] A. A. Shvartsburg, B. Liu, Z. Y. Lu, C. Z. Wang, M. F. Jarrold, and K. M. Ho. Structures of germanium clusters: Where the growth patterns of silicon and germanium clusters diverge. *Physical Review Letters*, 83(11):2167–2170, September 1999.
- [25] M. N. Blom, D. Schooss, J. Stairs, and M. M. Kappes. Experimental structure determination of silver cluster ions (Ag-*n*(+), 19 < *n* < 79). *Journal of Chemical Physics*, 124(24):244308, June 2006.
- [26] D. Schooss, M. N. Blom, J. H. Parks, B. von Issendorff, H. Haberland, and M. M. Kappes. The structures of Ag-55(+) and Ag-55(-): Trapped ion electron diffraction and density functional theory. *Nano Letters*, 5(10):1972–1977, October 2005.
- [27] M. D. Morse. Clusters of transition-metal atoms. *Chemical Reviews*, 86(6):1049–1109, December 1986.
- [28] H. G. Kramer, V. Beutel, K. Weyers, and W. Demtroder. Sub-doppler laser spectroscopy of silver dimers Ag-2 in a supersonic beam. *Chemical Physics Letters*, 193(5):331–334, June 1992.

- [29] B. A. Collings, K. Athanassenas, D. M. Rayner, and P. A. Hackett. Optical spectroscopy of Ag₇, Ag-9+, and Ag₉ - A test of the photodepletion method. *Chemical Physics Letters*, 227(4-5):490–495, September 1994.
- [30] J. Tiggesbaumker, L. Koller, H. O. Lutz, and K. H. Meiwesbroer. Giant-resonances in silver-cluster photofragmentation. *Chemical Physics Letters*, 190(1-2):42–47, February 1992.
- [31] A. Terasaki, T. Majima, and T. Kondow. Photon-trap spectroscopy of mass-selected ions in an ion trap: Optical absorption and magneto-optical effects. *Journal of Chemical Physics*, 127(23):231101, December 2007.
- [32] M. Moskovits and G. A. Ozin. Thermodynamic considerations regarding matrix stability of Mln complexes (where L=co or N₂). *Journal of Molecular Structure*, 32(1):71–78, 1976.
- [33] W. Harbich, S. Fedrigo, F. Meyer, D. M. Lindsay, J. Lignieres, J. C. Rivoal, and D. Kreisle. Deposition of mass selected silver clusters in rare-gas matrices. *Journal of Chemical Physics*, 93(12):8535–8543, December 1990.
- [34] E. C. Honea, A. Ogura, C. A. Murray, K. Raghavachari, W. O. Sprenger, M. F. Jarrold, and W. L. Brown. Raman-spectra of size-selected silicon clusters and comparison with calculated structures. *Nature*, 366(6450):42–44, November 1993.
- [35] T. L. Haslett, K. A. Bosnick, and M. Moskovits. Ag-5 is a planar trapezoidal molecule. *Journal of Chemical Physics*, 108(9):3453–3457, March 1998.
- [36] K. A. Bosnick, T. L. Haslett, S. Fedrigo, M. Moskovits, W. T. Chan, and R. Fournier. Tri-capped tetrahedral Ag-7: A structural determination by resonance Raman spectroscopy and density functional theory. *Journal of Chemical Physics*, 111(19):8867–8870, November 1999.
- [37] B. Zhao, H. Y. Lu, J. Jules, and J. R. Lombardi. Absorption and Raman spectroscopy of mass-selected scandium tetramers in argon matrices. *Chemical Physics Letters*, 362(1-2):PII S0009–2614(02)01039–4, August 2002.
- [38] A. Biesso, W. Qian, and Mostafa A. El-Sayed. Gold nanoparticle plasmonic field effect on the primary step of the other photosynthetic system in nature, bacteriorhodopsin. *Journal of the American Chemical Society*, 130(11):3258–+, March 2008.
- [39] A. Biesso, W. Qian, X. Huang, and Mostafa A. El-Sayed. Gold nanoparticles surface plasmon field effects on the proton pump process of the bacteriorhodopsin photosynthesis. *Journal of the American Chemical Society*, 131(7):2442–+, February 2009.
- [40] S. Neretina, W. Qian, Erik C. Dreaden, Mostafa A. El-Sayed, Robert A. Hughes, John S. Preston, and P. Mascher. Exciton lifetime tuning by changing the plasmon field orientation with respect to the exciton transition moment direction: CdTe-Au core-shell nanorods. *Nano Letters*, 9(3):1242–1248, March 2009.

Bibliography

- [41] S. Neretina, Erik C. Dreaden, W. Qian, Mostafa A. El-Sayed, Robert A. Hughes, John S. Preston, and P. Mascher. The dependence of the plasmon field induced nonradiative electronic relaxation mechanisms on the gold shell thickness in vertically aligned CdTe-Au core-shell nanorods. *Nano Letters*, 9(11):3772–3779, November 2009.
- [42] T. W. Odom and G. C. Schatz. Introduction to plasmonics. *Chemical Reviews*, 111(6):3667–3668, June 2011.
- [43] J. E. Millstone, S. J. Hurst, G. S. Metraux, J. I. Cutler, and C. A. Mirkin. Colloidal gold and silver triangular nanoprisms. *Small*, 5(6):646–664, March 2009.
- [44] E. B. Dickerson, E. C. Dreaden, X. Huang, I. H. El-Sayed, H. Chu, S. Pushpanketh, J. F. McDonald, and M. A. El-Sayed. Gold nanorod assisted near-infrared plasmonic photothermal therapy (PPTT) of squamous cell carcinoma in mice. *Cancer Letters*, 269(1):57–66, September 2008.
- [45] M. Haruta. Size- and support-dependency in the catalysis of gold. *Catalysis Today*, 36(1):153–166, April 1997.
- [46] M. Haruta. Catalysis - gold rush. *Nature*, 437(7062):1098–1099, October 2005.
- [47] U. Kreibig and M. Vollmer. Optical properties of metal clusters. *Springer series in materials*, 25, 1676.
- [48] C. F. Bohren and D. R. Huffman. Absorption and scattering of light by small particles. *Wiley, New-York*, 1983.
- [49] M. Moseler, H. Hakkinen, and U. Landman. Photoabsorption spectra of Na-n(+) clusters: Thermal line-broadening mechanisms. *Physical Review Letters*, 87(5):053401, July 2001.
- [50] U. Landman. Materials by numbers: Computations as tools of discovery. *Proceedings of the National Academy of Sciences of the United States of America*, 102(19):6671–6678, May 2005.
- [51] S. Lecoultre, A. Rydlo, J. Buttet, C. Felix, S. Gilb, and W. Harbich. Ultraviolet-visible absorption of small silver clusters in neon: Ag-n (n=1-9). *Journal of Chemical Physics*, 134(18):184504, May 2011.
- [52] S. Fedrigo, W. Harbich, J. Belyaev, and J. Buttet. Evidence for electronic shell structure of small silver clusters in the optical-absorption spectra. *Chemical Physics Letters*, 211(2-3):166–170, August 1993.
- [53] S. Lecoultre, A. Rydlo, C. Felix, J. Buttet, S. Gilb, and W. Harbich. UV-visible absorption of small gold clusters in neon: Au-n (n=1-5 and 7-9). *Journal of Chemical Physics*, 134(7):074302, February 2011.

-
- [54] S. Lecoultre, A. Rydlo, C. Felix, J. Buttet, S. Gilb, and W. Harbich. Optical absorption of small copper clusters in neon: Cu- n , ($n=1-9$). *Journal of Chemical Physics*, 134(7):074303, February 2011.
- [55] M. Moskovits. Surface-enhanced spectroscopy. *Reviews of Modern Physics*, 57(3):783–826, 1985.
- [56] M. Fleischmann, P. J. Hendra, and McQuilla. AJ. Raman-spectra of pyridine adsorbed at a silver electrode. *Chemical Physics Letters*, 26(2):163–166, 1974.
- [57] M. G. Albrecht and J. A. Creighton. Anomalously intense Raman-spectra of pyridine at a silver electrode. *Journal of the American Chemical Society*, 99(15):5215–5217, 1977.
- [58] J. A. Dieringer, II Lettan, R. B., K. A. Scheidt, and R. P. Van Duyne. A frequency domain existence proof of single-molecule surface-enhanced Raman spectroscopy. *Journal of the American Chemical Society*, 129(51):16249–16256, December 2007.
- [59] L. L. Zhao, L. Jensen, and G. C. Schatz. Pyridine-Ag-20 cluster: A model system for studying surface-enhanced Raman scattering. *Journal of the American Chemical Society*, 128(9):2911–2919, March 2006.
- [60] L. Jensen, L. Zhao, and George C. Schatz. Size-dependence of the enhanced raman scattering of pyridine adsorbed on Ag- n ($n=2-8, 20$) clusters. *Journal of Physical Chemistry C*, 111(12):4756–4764, March 2007.
- [61] J. Gaff and S. Franzen. Resonance Raman enhancement of pyridine on Ag clusters. *Chemical Physics*, 397:34–41, March 2012.
- [62] J. A. Scholl, A. Koh, and J. A. Dionne. Quantum plasmon resonances of individual metallic nanoparticles. *Nature*, 483(7390):421–U68, March 2012.
- [63] W. A. DeHeer. The physics of simple metal-clusters - experimental aspects and simple-models. *Reviews of Modern Physics*, 65(3):611–676, July 1993.
- [64] M. Brack. The physics of simple metal-clusters - Self-consistent Jellium model and semiclassical approaches. *Reviews of Modern Physics*, 65(3):677–732, July 1993.
- [65] G. V. Hartland. Optical studies of dynamics in noble metal nanostructures. *Chemical Reviews*, 111(6):3858–3887, June 2011.
- [66] S. Lecoultre. Propriétés optiques de petits agrégats de métaux nobles en matrice de neon. *EPFL These*, 4361, 2009.
- [67] S. M. Morton, D. W. Silverstein, and L. Jensen. Theoretical studies of plasmonics using electronic structure methods. *Chemical Reviews*, 111(6):3962–3994, June 2011.
- [68] R. Ruppin and H. Yatom. Size and shape effects on broadening of plasma resonance-absorption in metals. *Physica Status Solidi B-basic Research*, 74(2):647–654, 1976.

Bibliography

- [69] A. Lushnikov and A. J. Simonov. Surface plasmons in small metal particles. *Zeitschrift Fur Physik*, 270(1):17–24, 1974.
- [70] W. Ekardt. Size-dependent photoabsorption and photoemission of small metal particles. *Physical Review B*, 31(10):6360–6370, 1985.
- [71] A. Sihvola. Dielectric polarization and particle shape effects. *Journal of Nanomaterials*, page 45090, 2007.
- [72] S. Raza, N. Stenger, S. Kadkhodazadeh, S. V. Fischer, N. Kotesha, A. Jauho, A. Burrows, M. Wubs, and N. A. Mortensen. Blueshift of the surface plasmon resonance in silver nanoparticles studied with EELS. *Nanophotonics*, 2(2):131–138, 2013.
- [73] G. Bae and Christine M. Aikens. Time-dependent density functional theory studies of optical properties of Ag nanoparticles: octahedra, truncated octahedra, and icosahedra. *Journal of Physical Chemistry C*, 116(40):21646–21646, October 2012.
- [74] M. A. L. Marques and E. K. U. Gross. Time-dependent density functional theory. *Annual Review of Physical Chemistry*, 55:427–455, 2004.
- [75] P. Hohenberg and W. Kohn. Inhomogeneous electron gas. *Physical Review B*, 136(3B):B864–+, 1964.
- [76] L. H. Thomas. The calculation of atomic fields. *Proceedings of the Cambridge Philosophical Society*, 23:542–548, July 1927.
- [77] E. Fermi. A statistical method for determining some properties of the atoms and its application to the theory of the periodic table of elements. *Zeitschrift Fur Physik*, 48(1-2):73–79, January 1928.
- [78] W. Kohn and L. J. Sham. Self-consistent equations including exchange and correlation effects. *Physical Review*, 140(4A):1133–&, 1965.
- [79] D. M. Ceperley and B. J. Alder. Ground-state of the electron-gas by a stochastic method. *Physical Review Letters*, 45(7):566–569, 1980.
- [80] M. A. L. Marques and E. K. U. Gross. Time-dependent density functional theory. *Primer In Density Functional Theory*, 620:Univ Coimbra, Ctr Computat Phys, 2003.
- [81] E. Runge and E. K. U. Gross. Density-functional theory for time-dependent systems. *Physical Review Letters*, 52(12):997–1000, 1984.
- [82] A. Zangwill and P. Soven. Density-functional approach to local-field effects in finite systems - photoabsorption in the rare-gases. *Physical Review A*, 21(5):1561–1572, 1980.
- [83] F. W. King, R. P. Vanduyne, and G. C. Schatz. Theory of raman-scattering by molecules adsorbed on electrode surfaces. *Journal of Chemical Physics*, 69(10):4472–4481, 1978.

-
- [84] J. R. Lombardi and R. L. Birke. Time-dependent picture of the charge-transfer contributions to surface enhanced Raman spectroscopy. *Journal of Chemical Physics*, 126(24):244709, June 2007.
- [85] J. R. Lombardi and R. L. Birke. A unified view of surface-enhanced Raman scattering. *Accounts of Chemical Research*, 42(6):734–742, June 2009.
- [86] J. R. Lombardi and R. L. Birke. A unified approach to surface-enhanced Raman spectroscopy. *Journal of Physical Chemistry C*, 112(14):5605–5617, April 2008.
- [87] F. Conus, J. T. Lau, V. Rodrigues, and C. Felix. High sensitivity absorption measurement of small metal clusters embedded in an argon matrix. *Review of Scientific Instruments*, 77(11):113103, November 2006.
- [88] H. Haberland, M. Mall, M. Moseler, Y. Qiang, T. Reiners, and Y. Thurner. Filling of micron-sized contact holes with copper by energetic cluster-impact. *Journal of Vacuum Science & Technology A*, 12(5):2925–2930, September 1994.
- [89] I. M. Goldby, B. vonIssendorff, L. Kuipers, and R. E. Palmer. Gas condensation source for production and deposition of size-selected metal clusters. *Review of Scientific Instruments*, 68(9):3327–3334, September 1997.
- [90] M. A. Rottgen, K. Judai, J. M. Antonietti, U. Heiz, S. Rauschenbach, and K. Kern. Conical octopole ion guide: Design, focusing, and its application to the deposition of low energetic clusters. *Review of Scientific Instruments*, 77(1):013302, January 2006.
- [91] A. M. Dudarev, M. Marder, Q. Niu, N. J. Fisch, and M. G. Raizen. Statistical mechanics of an optical phase space compressor. *Europhysics Letters*, 70(6):761–767, June 2005.
- [92] P. H. Dawson. Experimental measurements of quadrupole mass analyzer performance and comparison with theoretical predictions. *International Journal of Mass Spectrometry and Ion Processes*, 21(3-4):317–332, 1976.
- [93] P. H. Dawson. Energetics of ions in quadrupole fields. *International Journal of Mass Spectrometry and Ion Processes*, 20(2-3):237–245, 1976.
- [94] R. Alayan, L. Arnaud, A. Bourgey, M. Broyer, E. Cottancin, J. R. Huntzinger, J. Lerme, J. L. Vialle, M. Pellarin, and G. Guiraud. Application of a static quadrupole deviator to the deposition of size-selected cluster ions from a laser vaporization source. *Review of Scientific Instruments*, 75(7):2461–2470, July 2004.
- [95] A. Rydlo. Study of the optical UV-visible electron induced luminescence of small size selected metal clusters in rare gas solids. *EPFL These*, 4734, 2010.
- [96] B. E. Wilcox, C. L. Hendrickson, and A. G. Marshall. Improved ion extraction from a linear octopole ion trap: SIMION analysis and experimental demonstration. *Journal of the American Society For Mass Spectrometry*, 13(11):PII 1044–0305(02)00622–0, November 2002.

Bibliography

- [97] W. Harbich. Collision of clusters with surfaces: Deposition, surface modification and scattering.
- [98] S. Fedrigo, W. Harbich, and J. Buttet. Media effects on the optical-absorption spectra of silver clusters embedded in rare-gas matrices. *International Journal of Modern Physics B*, 6(23-24):FDN IBM ITALIA; SISSA, December 1992.
- [99] S. Fedrigo, W. Harbich, and J. Buttet. Optical-response of Ag₂, Ag₃, Au₂, and Au₃ in argon matrices. *Journal of Chemical Physics*, 99(8):5712–5717, October 1993.
- [100] M. C. Daniel and D. Astruc. Gold nanoparticles: Assembly, supramolecular chemistry, quantum-size-related properties, and applications toward biology, catalysis, and nanotechnology. *Chemical Reviews*, 104(1):293–346, January 2004.
- [101] H. Chen, Martin G. Blaber, Stacey D. Standridge, Erica J. DeMarco, Joseph T. Hupp, Mark A. Ratner, and George C. Schatz. Computational modeling of plasmon-enhanced light absorption in a multicomponent dye sensitized solar cell. *Journal of Physical Chemistry C*, 116(18):10215–10221, May 2012.
- [102] V. Bonacic-Koutecky and Thorsten M. Bernhardt. Structure and reactivity of small particles: from clusters to aerosols. *Physical Chemistry Chemical Physics*, 14(26):9252–9254, 2012.
- [103] M. Harb, F. Rabilloud, D. Simon, A. Rydlo, S. Lecoultré, F. Conus, V. Rodrigues, and C. Felix. Optical absorption of small silver clusters: Ag(*n*), (*n*=4-22). *Journal of Chemical Physics*, 129(19):194108, November 2008.
- [104] S. Fedrigo. Spectroscopie optique de clusters de métaux nobles tries en mass et deposees dans une matrice de gaz rare. *EPFL These*, 1084, 1992.
- [105] P. B. Johnson and R. W. Christy. Optical constants of noble metals. *Physical Review B*, 6(12):4370–4379, 1972.
- [106] W. Harbich, S. Fedrigo, and J. Buttet. The optical-absorption spectra of small silver clusters (*n*=8-39) embedded in rare-gas matrices. *Zeitschrift Fur Physik D-atoms Molecules and Clusters*, 26(1-4):NATL SCI FDN; NATO; ARGONNE NATL LAB; UNIV CHICAGO, CHEM DEPT; DOW CORP;EOLEOLEXTREL; FORD MOTO; IBM; THREE M CO; AMOCO, May 1993.
- [107] H. Hovel, S. Fritz, A. Hilger, U. Kreibig, and M. Vollmer. Width of cluster plasmon resonances - bulk dielectric functions and chemical interface damping. *Physical Review B*, 48(24):18178–18188, December 1993.
- [108] K. P. Charle, L. König, S. Nepijko, I. Rabin, and W. Schulze. The surface plasmon resonance of free and embedded Ag-clusters in the size range 1,5 nm < *D* < 30 nm. *Crystal Research and Technology*, 33(7-8):1085–1096.

-
- [109] V. Kasperovich and V. V. Kresin. Ultraviolet photoabsorption spectra of silver and gold nanoclusters. *Philosophical Magazine B-physics of Condensed Matter Statistical Mechanics Electronic Optical and Magnetic Properties*, 78(4):385–396, October 1998.
- [110] S. M. Reimann and M. Brack. Shell structures and its semiclassical interpretation for spheroidally deformed sodium clusters. *Computational Materials Science*, 2(3-4):433–440, July 1994.
- [111] C. Zhang, Y. He, H. P. Cheng, Y. Q. Xue, M. A. Ratner, X. G. Zhang, and P. Krstic. Current-voltage characteristics through a single light-sensitive molecule. *Physical Review B*, 73(12):125445, March 2006.
- [112] T. G. Schaaff and R. L. Whetten. Giant gold-glutathione cluster compounds: Intense optical activity in metal-based transitions. *Journal of Physical Chemistry B*, 104(12):2630–2641, March 2000.
- [113] M. Haruta, N. Yamada, T. Kobayashi, and S. Iijima. Gold catalysts prepared by coprecipitation for low-temperature oxidation of hydrogen and of carbon-monoxide. *Journal of Catalysis*, 115(2):301–309, February 1989.
- [114] M. Valden, X. Lai, and D. W. Goodman. Onset of catalytic activity of gold clusters on titania with the appearance of nonmetallic properties. *Science*, 281(5383):1647–1650, September 1998.
- [115] G. A. Bishea and M. D. Morse. Spectroscopic studies of jet-cooled AgAu and Au₂. *Journal of Chemical Physics*, 95(8):5646–5659, October 1991.
- [116] W. Harbich, S. Fedrigo, and J. Buttet. The optical-absorption spectra of small silver clusters ($n = 5-11$) embedded in argon matrices. *Chemical Physics Letters*, 195(5-6):613–617, July 1992.
- [117] J. Zheng, C. W. Zhang, and R. M. Dickson. Highly fluorescent, water-soluble, size-tunable gold quantum dots. *Physical Review Letters*, 93(7):077402, August 2004.
- [118] A. Cecconello, C. Lu, J. Elbaz, and I. Willner. Au nanoparticle/DNA rotaxane hybrid nanostructures exhibiting switchable fluorescence properties. *Nano Letters*, 13(12):6275–6280, December 2013.
- [119] J. H. Guo, L. Z. Liu, X. B. Zhu, X. L. Wu, and Paul K. Chu. Enhanced fluorescence from dye molecules by Au nanoparticles on asymmetric double-stranded DNA and mechanism. *Applied Physics Letters*, 104(14):141910, April 2014.
- [120] H. He, C. Xie, and J. Ren. Nonbleaching fluorescence of gold nanoparticles and its applications in cancer cell imaging. *Analytical Chemistry*, 80(15):5951–5957, August 2008.

Bibliography

- [121] C. Liu, T. Liu, T. Hsieh, H. Liu, Y. Chen, C. Tsai, H. Chen, J. Lin, R. Hsu, T. Wang, C. Chen, C. Sun, and P. Chou. In vivo metabolic imaging of insulin with multiphoton fluorescence of human insulin-Au nanodots. *Small*, 9(12):2103–2110, June 2013.
- [122] P. Reineck, D. Gomez, S. Ng, M. Karg, T. Bell, P. Mulvaney, and U. Bach. Distance and wavelength dependent quenching of molecular fluorescence by Au@SiO₂ core-shell nanoparticles. *Acs Nano*, 7(8):6636–6648, August 2013.
- [123] Y. Wang, Y. Wang, F. Zhou, P. Kim, and Y. Xia. Protein-protected Au clusters as a new class of nanoscale biosensor for label-free fluorescence detection of proteases. *Small*, 8(24):3769–3773, December 2012.
- [124] X. Wen, P. Yu, Y. Toh, X. Ma, S. Huang, and J. Tang. Fluorescence origin and spectral broadening mechanism in atomically precise Au-8 nanoclusters. *Nanoscale*, 5(21):10251–10257, 2013.
- [125] C. M. Aikens. Effects of core distances, solvent, ligand, and level of theory on the TDDFT optical absorption spectrum of the thiolate-protected Au-25 nanoparticle. *Journal of Physical Chemistry A*, 113(40):10811–10817, October 2009.
- [126] R. W. Burgess and V. J. Keast. TDDFT study of the optical absorption spectra of bare and coated Au-55 and Au-69 clusters. *Journal of Physical Chemistry C*, 115(43):21016–21021, November 2011.
- [127] J. C. Idrobo, W. Walkosz, S. Yip, S. Oeguet, J. Wang, and J. Jellinek. Static polarizabilities and optical absorption spectra of gold clusters (Au- n , $n=2-14$ and 20) from first principles. *Physical Review B*, 76(20):205422, November 2007.
- [128] J. V. Koppen, M. Hapka, M. M. Szczesniak, and G. Chalasinski. Optical absorption spectra of gold clusters Au- n ($n=4, 6, 8, 12, 20$) from long-range corrected functionals with optimal tuning. *Journal of Chemical Physics*, 137(11):114302, September 2012.
- [129] M. Kuehn and F. Weigend. Implementation of two-component time-dependent density functional theory in turbomole. *Journal of Chemical Theory and Computation*, 9(12):5341–5348, December 2013.
- [130] Y. Xu, J. Sherwood, Y. Qin, D. Crowley, M. Bonizzoni, and Y. Bao. The role of protein characteristics in the formation and fluorescence of Au nanoclusters. *Nanoscale*, 6(3):1515–1524, 2014.
- [131] Z. Wu and R. Jin. On the ligand’s role in the fluorescence of gold nanoclusters. *Nano Letters*, 10(7):2568–2573, July 2010.
- [132] X. Wen, P. Yu, Y. Toh, A. Hsu, Y. Lee, and J. Tang. Fluorescence dynamics in BSA-protected Au-25 nanoclusters. *Journal of Physical Chemistry C*, 116(35):19032–19038, September 2012.

-
- [133] S. Lecoultre, A. Rydlo, C. Felix, and W. Harbich. Gold dimer in neon: an absorption and fluorescence study. *European Physical Journal D*, 52(1-3):187–190, April 2009.
- [134] E. M. Fernandez, J. M. Soler, and L. C. Balbas. Planar and cagelike structures of gold clusters: Density-functional pseudopotential calculations. *Physical Review B*, 73(23):235433, June 2006.
- [135] X. Li, H. Wang, X. Yang, Z. Zhu, and Y. Tang. Size dependence of the structures and energetic and electronic properties of gold clusters. *Journal of Chemical Physics*, 126(8):084505, February 2007.
- [136] T. Saue and H. J. A. Jensen. Linear response at the 4-component relativistic level: Application to the frequency-dependent dipole polarizabilities of the coinage metal dimers. *Journal of Chemical Physics*, 118(2):522–536, January 2003.
- [137] R. Guo, K. Balasubramanian, X. F. Wang, and L. Andrews. Infrared vibronic absorption spectrum and spin-orbit calculations of the upper spin-orbit component of the Au-3 ground state. *Journal of Chemical Physics*, 117(4):1614–1620, July 2002.
- [138] C. M. Aikens and G. C. Schatz. TDDFT studies of absorption and SERS spectra of pyridine interacting with Au₂₀. *Journal of Physical Chemistry A*, 110(49):13317–13324, December 2006.
- [139] X. J. Wang, X. H. Wan, H. Zhou, S. Takami, M. Kubo, and A. Miyamoto. Electronic structures and spectroscopic properties of dimers Cu-2, Ag-2, and Au-2 calculated by density functional theory. *Journal of Molecular Structure-theochem*, 579:PII S0166–1280(01)00729–1, March 2002.
- [140] I. Itkin and A. Zaitsevskii. Quasirelativistic multipartitioning perturbation theory calculations on electronic transitions in Au-2. *Chemical Physics Letters*, 374(1-2):143–150, June 2003.
- [141] F. Wang, T. Ziegler, E. van Lenthe, S. van Gisbergen, and E. J. Baerends. The calculation of excitation energies based on the relativistic two-component zeroth-order regular approximation and time-dependent density-functional with full use of symmetry. *Journal of Chemical Physics*, 122(20):204103, May 2005.
- [142] M. A. Omary, M. A. Rawashdeh-Omary, C. C. Chusuei, J. P. Fackler, and P. S. Bagus. Electronic structure studies of six-atom gold clusters. *Journal of Chemical Physics*, 114(24):10695–10701, June 2001.
- [143] J. Laxmikanth Rao, G. Krishna Chaitanya, S. Basavaraja, K. Bhanuprakash, and A. Venkataramana. Density-functional study of Au-Cu binary clusters of small size (n=6): Effect of structure on electronic properties. *Journal of Molecular Structure-theochem*, 803(1-3):89–93, February 2007.

Bibliography

- [144] K. H. Wu, J. Li, and C. S. Lin. Remarkable second-order optical nonlinearity of nano-sized Au(20) cluster: a TDDFT study. *Chemical Physics Letters*, 388(4-6):353–357, April 2004.
- [145] R. H. Xie, G. W. Bryant, J. J. Zhao, T. Kar, and V. H. Smith. Tunable optical properties of icosahedral, dodecahedral, and tetrahedral clusters. *Physical Review B*, 71(12):125422, March 2005.
- [146] K. Kneipp, Y. Wang, H. Kneipp, L. T. Perelman, I. Itzkan, R. Dasari, and M. S. Feld. Single molecule detection using surface-enhanced Raman scattering (SERS). *Physical Review Letters*, 78(9):1667–1670, March 1997.
- [147] H. X. Xu, E. J. Bjerneld, M. Kall, and L. Borjesson. Spectroscopy of single hemoglobin molecules by surface enhanced raman scattering. *Physical Review Letters*, 83(21):4357–4360, November 1999.
- [148] K. Kneipp, Y. Wang, H. Kneipp, I. Itzkan, R. R. Dasari, and M. S. Feld. Population pumping of excited vibrational states by spontaneous surface-enhanced Raman scattering. *Physical Review Letters*, 76(14):2444–2447, April 1996.
- [149] L. Peyser-Capadona, J. Zheng, J. I. Gonzalez, T. H. Lee, S. A. Patel, and R. M. Dickson. Nanoparticle-free single molecule anti-stokes Raman spectroscopy. *Physical Review Letters*, 94(5):058301, February 2005.
- [150] I. Yamazaki and H. Baba. Observation of fluorescence of pyridine in vapor-phase. *Journal of Chemical Physics*, 66(12):5826–5827, 1977.
- [151] E. B. Hughes, H. H. G. Jellinek, and B. A. Ambrose. Pyridine - ultraviolet absorption spectrum and dissociation constant. *Journal of Physical and Colloid Chemistry*, 53(3):410–414, 1949.
- [152] P. Person, J. W. Lash, and A. Fine. On the presence of myoglobin and cytochrome oxidase in the cartilaginous odontophore of the marine snail, *busycon*. *Biological Bulletin*, 117(3):504–510, 1959.
- [153] D. M. Kolb and D. Leutloff. Fluorescence-spectra of matrix-isolated silver atoms. *Chemical Physics Letters*, 55(2):264–266, 1978.
- [154] H. Sponer. The near ultraviolet absorption of pyridine vapor. *Reviews of Modern Physics*, 16(3/4):0224–0225, July 1944.
- [155] S. Venkateswaran. On the raman effect in liquid pyridine. *Journal of Physical Chemistry*, 34(1):145–152, January 1930.
- [156] J. T. Golab, J. R. Sprague, K. T. Carron, G. C. Schatz, and R. P. Vanduyne. A surface enhanced hyper-raman scattering study of pyridine adsorbed onto silver - experiment and theory. *Journal of Chemical Physics*, 88(12):7942–7951, June 1988.

Acknowledgements

Now it's the time to thank all those people who have guided, helped and accompanied me during my four years of doctoral life.

First, I would like to thank my thesis director, Dr. Wolfgang Harbich, for offering me the possibility to carry out such an exciting thesis project and explore such an interesting physics world. I really appreciate for his wide and wise guidance throughout the project. He is always nice to me and willing to discuss with me. He taught me the way to be an experimental physicist, encouraging me during my work in the laboratory. He is not only a thesis director but also a friend and a mentor, sharing his experience with me and introducing the Swiss way of life to me.

I want to thank also Prof. Harald Brune for co-directing my thesis project. He has always provided me a lot of useful suggestions in my research, which widens my eyes and broaden my knowledge.

I thank Prof. Vitaly Kresin, Dr. Matthias Hillenkamp and Prof. Olivier Martin for doing me the honor of being my thesis juries, and Prof. Romuald Houdré being the president.

Thanks to Chantal Roulin, Florence Grandjean, Nadja Favre and Anh Eymann for their kind and warm help in all the administrative tasks.

Thanks to Claude Amendola, Gilles Grandjean and all the other technical staff from mechanical and electrical workshops for their remarkable technical help and support. I've really learned a lot of technical skills from them. Thanks also to Martial Doy, Primo Locatelli and Claire-Lise Bandelier for the IT support.

A special thanks to all my lovely colleagues in the group of Laboratory of Nanostructures at Surfaces. I have really enjoyed the group activities and had a happy time with them.

Last but not least, I want to particularly thank my family, relatives and friends for their endless support in my life. I love all of you!

Curriculum vitae

Chongqi Yu

Date of birth: 27 May 1986
Place of birth: Shanghai, China
Nationality: Chinese

2011-2015 Ph.D. candidate, Institute of Condensed Matter Physics (ICMP),
Department of Physics, Swiss Federal Institute of Technology
(EPFL), Lausanne, Switzerland

2008-2011 Master degree, Institute of Optical Science and Engineering
Research Center (OSERC), Department of Physics, Shanghai
Jiao Tong University, Shanghai, China

Master Thesis: Novel photoelectric effect in MOS structures

2004-2008 Bachelor degree, Institute of Applied Physics, Department of
Physics, Shanghai Jiao Tong University, Shanghai, China

Bachelor Thesis: New theory about lateral photovoltaic effect
in multilayer structure with external field

